COMPUTATIONAL CHARACTERIZATION OF DIFFUSIVE MASS TRANSFER IN POROUS SOLID OXIDE FUEL CELL COMPONENTS

A Dissertation
Presented to
The Academic Faculty

By

George J. Nelson

In Partial Fulfillment
Of the Requirements for the Degree
Doctor of Philosophy in Mechanical Engineering

Georgia Institute of Technology

December, 2009

COMPUTATIONAL CHARACTERIZATION OF DIFFUSIVE MASS TRANSFER IN POROUS SOLID OXIDE FUEL CELL COMPONENTS

Approved by:

Dr. William Wepfer, Co-Advisor
School of Mechanical Engineering
Georgia Institute of Technology

Dr. Comas Haynes, Co-Advisor
Georgia Tech Research Institute
Georgia Institute of Technology

Dr. Andrei Fedorov
School of Mechanical Engineering
Georgia Institute of Technology

Dr. Christiaan Paredis
School of Mechanical Engineering
Georgia Institute of Technology

Dr. Meilin Liu
School of Materials Science and Engineering
Georgia Institute of Technology

Dr. Amyn Teja
School of Chemical and Biomolecular Engineering
Georgia Institute of Technology

Date Approved: October 20, 2009

ACKNOWLEDGEMENTS

The present work was completed with the assistance of many people. I would first like to thank my co-advisors Dr. William Wepfer and Dr. Comas Haynes for their guidance and support during this project. Their complementary perspectives have strengthened this work, provided valuable insights on my research, and fortified the confidence I hold in my abilities. I would also like to thank Drs. Andrei Fedorov, Christiaan Paredis, Meilin Liu, and Amyn Teja who, as members of my reading committee, have helped shape this work and enabled its further refinement.

I would like to thank my parents, Robert and Carol Nelson for the support and encouragement they have provided to me throughout my life. I also thank my "extra parents," Robert and Christine Indech, for supplementing this support and encouragement.

Finally, and most of all, I would like to thank my phenomenal wife Jennifer Indech Nelson. Her analytical talents have been instrumental in the polishing of this work. Her advice and support have helped me navigate in all aspects of life. Her love and encouragement have bolstered my strength and mitigated my weakness. More than any other person, she enables the full realization of my potential.

TABLE OF CONTENTS

LIST OF TABLES

LIST OF FIGURES

NOMENCLATURE

a	Unit Cell Half Width, m
b	Fuel Stream Half Width, m
C_i	Reactant Concentration, mol/m^3
D_f	Fractal Dimension
D_{ij}	Binary Diffusion Coefficient, m^2/s
D_{ik}	Knudsen Diffusion Coefficient, m^2/s
d_p	Dominant Pore Size, m
F	Faraday Constant, C/mol
i''	Local Current Density, A/m^2 or A/cm^2
K_s	Surface Reaction Rate Coefficient, m/s
l	Length of Smallest Fractal Branch, m
L_{act}	Electrode Active Length, m
LF	Length Fraction
L_{GS}	Gas Stream Contact Width, m
L_p	Perimeter of Rough Interface, m
L_{Total}	Unit Cell Total Width, m
M_i	Molar Mass, kg/kmol
N_i	Molar Flux, mol/m^2-s
p_i	Partial Pressure, kPa
R_u	Universal Gas Constant, kJ/mol-K
T	Temperature, K

t	Thickness, m
t^*	Dimensionless Electrode Thickness
y_i	Mole Fraction
z	Electrons Participating in Reaction

Greek Symbols

ε	Porosity
Λ	Diffusion-Reaction Length Scale, m
τ	Tortuosity

Selected Superscripts

eff	Effective Diffusion Coefficient
n	Branch Number in Fractal Structure
ref	Reference Value
0	Gas Stream Value

Selected Subscripts

Ar	Argon
an	Bulk Anode Parameter
BC	Value Based on Button-Cell Approximation
ca	Bulk Cathode Parameter
dep	Value at Reactant Depletion
elec	General Electrode Parameter
H_2	Hydrogen
H_2O	Steam
O_2	Oxygen

N_2	Nitrogen
tot	Total

Selected Acronyms

CFD	Computational Fluid Dynamics
FEA	Finite Element Analysis
DGM	Dusty-Gas Model
LSA	Land Surveyor Approximation
MIEC	Mixed Ionic-Electronic Conductor
SOFC	Solid Oxide Fuel Cell
TPB	Triple-Phase Boundary
YSZ	Yttria-Stabilized Zirconia

SUMMARY

Diffusive mass transport within porous SOFC components is explored using two modeling approaches that can better inform the SOFC electrode design process. These approaches include performance metrics for electrode cross-sectional design and a fractal approach for modeling mass transport within the pore structure of the electrode reaction zone. The performance metrics presented are based on existing analytical models for transport within SOFC electrodes. These metrics include a correction factor for button-cell partial pressure predictions and two forms of dimensionless reactant depletion current density. The performance impacts of multi-dimensional transport phenomena are addressed through the development of design maps that capture the trade-offs inherent in the reduction of mass transport losses within SOFC electrode cross-sections. As a complement to these bulk electrode models, a fractal model is presented for modeling diffusion within the electrochemically active region of an SOFC electrode. The porous electrode is separated into bulk and reaction zone regions, with the bulk electrode modeled in one-dimension based on the dusty-gas formalism. The reaction zone is modeled in detail with a two-dimensional finite element model using a regular Koch pore cross-section as a fractal template for the pore structure. Drawing on concepts from the analysis of porous catalysts, this model leads to a straightforward means of assessing the performance impacts of reaction zone microstructure. Together, the modeling approaches presented provide key insights into the impacts of bulk and microstructural geometry on the performance of porous SOFC components.

CHAPTER 1

INTRODUCTION

1.1 Motivation and Overview

The implementation of a robust and sustainable energy infrastructure will require the development and application of myriad technologies. Among these technologies, solid oxide electrochemical cells present several advantages as energy conversion devices and could therefore play a key role in the realization of a robust, sustainable energy infrastructure. In solid oxide fuel cell (SOFC) applications, solid oxide cells directly convert chemical energy to electrical energy, alleviating many of the losses associated with thermal and mechanical energy conversion devices. This direct energy conversion also results in less problematic emissions streams with fewer components and reduced levels of criteria pollutants when compared to combustion based technologies [1]. In addition to their power production capabilities, solid oxide electrochemical cells offer the potential to act as hydrogen production devices under an applied electrical current [2, 3]. These solid oxide electrolysis cells (SOECs) offer the opportunity for hydrogen production at higher operating temperatures, which result in enhanced reaction kinetics and lower operating voltages. Furthermore, higher temperature operation results in a reduced Nernst potential, meaning a lower thermodynamic minimum voltage is required for SOEC operation when compared to lower temperature electrolysis methods. Finally, these power and hydrogen production capabilities can be paired for solid oxide regenerative fuel cell (SORFC) applications, which are receiving increased attention as energy storage devices in renewable power systems. Acting as SOFCs, these

regenerative fuel cells produce electrical power to meet load requirements. Depending on the specific application, this load may be a fixed system base load or a dynamic peaking load. While under an applied electrical load SORFCs serve as electrolysis cells producing hydrogen for future fuel needs [4, 5].

The modeling methods that inform the design of solid oxide cells span many levels of detail and must balance complexity and computational cost. These levels of detail are often distinguished based on scale as illustrated in Figure 1.1. To obtain macro-scale insights efficiently, simplified models often sacrifice key details like the influence of cell geometry or the role of electrode microstructure on mass transport performance. Conversely, detailed microstructural models may draw heavily upon computing resources to ascertain highly localized insights into physical phenomena within a given cell. While such examples lie at the extremes of the complexity/computational cost spectrum, imbalance between these two aspects is often the case. Solid oxide cell design and system optimization efforts would be aided by the continued development of cell, stack, and system level models that run with reduced computational burden while retaining key design information from high fidelity component models. However, achieving this goal requires development of component level models that can translate solution fidelity to higher level models.

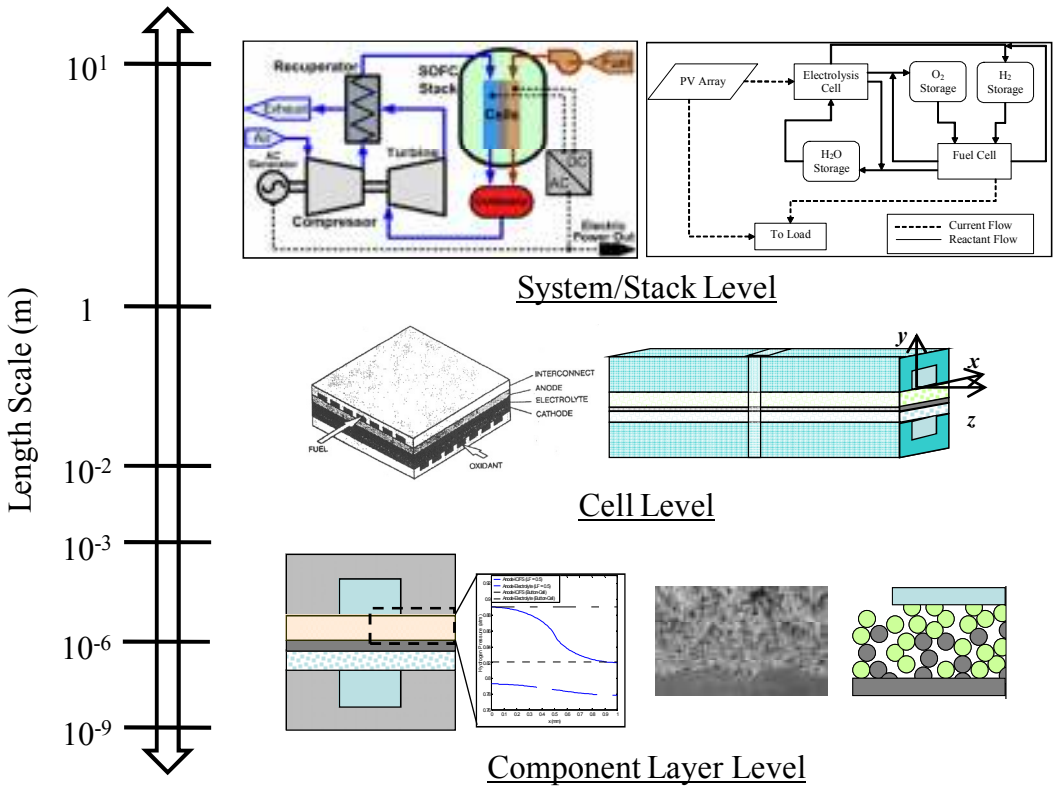

Figure 1.1 Common levels of modeling detail applied in SOFC research

The present work demonstrates two component-level SOFC modeling approaches capable of translating solution fidelity to higher level models. An emphasis is placed on the more common SOFC application of solid oxide cells. However, similar modeling approaches may be useful in the analysis of SOEC and SORFC systems. The modeling approaches presented focus on the development of reduced order models of SOFC gas transport within the porous electrodes. The first approach applies simplified Fickian models of mass diffusion within the electrodes toward the development of performance metrics for the design of SOFC electrode cross-sectional geometry. These performance metrics elucidate the trade-offs inherent in the reduction of losses associated with mass transport. The second approach applies fractal templates to modeling diffusion within the porous electrode microstructure with a focus on capturing the impact of microstructural

details within electrochemically active regions of the electrodes. In addition to providing an accessible means of modeling microstructural detail, this fractal approach draws a connection to an approximation for porous catalyst performance prediction that provides a reduced order approach for describing the impacts of reaction zone microstructure.

Analytical solutions of the two-dimensional Laplace equation have been developed to describe partial pressure distributions of reactants within solid oxide fuel cell (SOFC) electrodes. These analytical models capture the performance impacts of interconnect and gas channel contact area sizing. Specifically, the effects of cross-sectional area changes caused by distinct gas channel (mass transport) and interconnect (electronic transport) contact regions within the SOFC are described. In addition to demonstrating the effects of interconnect geometry on electrode performance these analytical models introduce the concept of a reactant depletion current density, which in many cases is distinct from the traditionally defined limiting current density [6]. This depletion current density describes the onset of reactant depletion at the electrode-electrolyte interface, which is assumed to initiate at the interconnect rib midpoint, as shown in Figure 1.2.

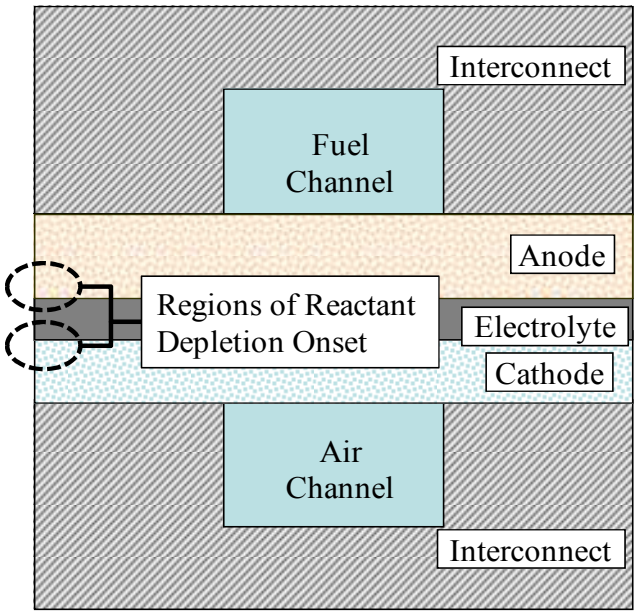

Figure 1.2 SOFC unit cell cross-section geometry with regions susceptible to reactant depletion highlighted

In the present work existing analytical expressions for two-dimensional reactant partial pressure distributions and reactant depletion current densities are further developed into dimensionless performance metrics for SOFC electrodes. These metrics include a correction factor that can be applied to button-cell predictions of pressure distribution and two forms of dimensionless reactant depletion current density.

Performance predictions based on the dimensionless performance metrics for electrode mass transport are compared to numerical predictions of partial pressure and depletion current density based on a finite element solution of the dusty-gas model (DGM) within SOFC electrodes. It is shown that the pressure correction factor developed provides a reasonable prediction of interconnect geometry effects without incurring an excessive computational burden. Thus, it is presented as a modeling tool that can be applied to translate component level fidelity to cell and stack level models. The depletion current density metrics developed are used to present basic design maps for

SOFC unit cell cross-sections. The first dimensionless form of the depletion current density presented can be used to judge the influence of sheet resistance effects on reactant depletion and to determine when reducing electrode thickness will no longer benefit mass transfer performance for a given unit cell cross-section geometry. The second dimensionless form of the depletion current density provides a gauge of deviation from the limiting current behavior predicted using a button-cell model. Thus it can be used as a design tool that is compatible with established button-cell approaches that are used in the experimental characterization of SOFC performance. Together these two current density metrics demonstrate that balancing contact lengths and the primary characteristic dimensions in the design of SOFC electrode cross-section geometry is generally desirable for mass transport performance.

The analytical solutions and associated dimensionless performance metrics presented in this work are developed from electrode models that rely on average microstructural parameters to modify diffusion coefficients and assume that electrochemically active regions near the electrode-electrolyte interface are planar. While useful design insights can be extracted from these models, the non-uniform nature of electrode microstructure and its effect on electrode performance cannot be fully captured by bulk parameters. Additionally, microstructural details such as heightened active lengths and the extension of reaction zone beyond electrode-electrolyte "bulk" interface may impact performance. For greater design insights consideration must be given to the microstructural details of the electrodes, particularly within the electrochemically active regions. To this end, a detailed electrode model is developed using a macro/micro finite element approach to solve key transport equations within SOFC electrodes. The porous electrode is separated

into supporting and electrochemically active regions. At the continuum component level this model focuses on the supporting SOFC electrode region with neutral species transport modeled using the dusty-gas formalism assuming average microstructural parameters. Near the electrochemically active electrode-electrolyte interface a micro-scale model is developed to describe gaseous diffusion within the electrode pores. The morphology of the pore surfaces is given consideration using fractal geometry models in an effort to capture the effects of pore surface irregularity on transport performance. Fractal structures common in the study of porous media can serve as templates for electrode pore structure and allow for the more detailed examination of diffusion phenomena. In the present work, the electrochemically active region is modeled in detail using a regular Koch pore cross-section as a fractal template. The fractal structure allows for the constraint of microstructural parameters, such as porosity, and enables the targeted specification of pore sizes and active boundaries. This capability results from the scaling relation that exists between the parts of the fractal.

The fractal model developed is corroborated through comparison to published experimental results for electrode and cell polarization behavior. Additionally, modeling results are compared to one-dimensional transport models applying the common assumption of a planar reaction zone, and performance variations in microstructure that may exist for electrodes with the same average bulk properties are investigated. The initial results presented suggest that more accurately accounting for microstructural details within the reaction zone impacts performance predictions, but such details cannot be considered the sole factor of influence. Increasing active length within the reaction zone results in reduced predictions of cell performance with respect to mass transport as

indicated by predictions of mass transport, polarization, and limiting current behavior. Modeling results suggest that scaling between the apparent and actual active areas may play a dominant role in the mass transport performance of SOFC electrodes. Additional exploration of mass transport dependence on characteristics of the fractal template applied for the reaction zone allows for discerning between the impacts of geometric scaling effects and other factors, such as active site accessibility.

The studies of the detailed electrode model also provide the groundwork for investigating a simplified approach to modeling SOFC neutral species transport based on an existing approximation for porous catalyst performance. This approach, referred to as the Land Surveyor Approximation (LSA), suggests that the microstructure impacts electrode performance through scaling and accessibility effects. The former relates to the increase in active length that results from an irregular active surface and accounts for scaling between the apparent and actual active length for an electrode. The latter relates to the influence that microstructural features, within the electrode, exert over reactant transport to active sites. Analysis of the transport problem in light of the LSA approach provides a justification for the dominance of scaling effects seen in the fractal modeling studies. Furthermore, the LSA may provide an accessible means for the future exploration of microstructural influence on SOFC performance inclusive of detailed reaction kinetics and percolation phenomena.

1.2 Significance and Contribution

The work presented offers an enhanced understanding of the mass transport mechanisms within SOFC porous components and extends the knowledge base of

transport phenomena that affect cell performance by outlining two modeling approaches that can better inform the SOFC electrode design process. These two approaches include expressions for dimensionless performance metrics for electrode cross-sectional design and a fractal approach for modeling mass transport within the electrode pore structure. The first of these approaches describes the performance impacts of multi-dimensional mass transport and allows for the development of design maps for electrode cross-section geometry. The second approach provides an accessible numerical approach to modeling transport within the electrode microstructure and uncovers a reduced order approach that can account for electrode microstructural details.

Analytical models have been developed to describe diffusive mass transfer in SOFC electrode cross-sections. These models offer key design insights on gas channel sizing trade-offs and multi-dimensional reactant depletion phenomena while offering a significantly reduced computational burden compared to numerical approaches. Development and exploration of these models and the associated design maps provide several key contributions. First, the neglect of mass transfer limitations arising from cathode geometry, based on presumed one-dimensional transport, is shown to be a tenuous assumption. The counterintuitive insight that thinner electrodes are not necessarily better for mass transport results from this realization. Additionally, a basic partial pressure correction factor is developed for translating component level information about mass transport to higher level SOFC models, and it is shown that with proper definition of diffusion coefficients this correction factor may provide sufficient accuracy compared to more detailed numerical approaches. Third, through a normalized form of the depletion current density a means is presented for determining the reactant

depletion performance for an electrode as compared to the standard experimental button-cell measurement. As with the pressure correction factor, this form of the depletion current density captures the same behavior predicted with numerical models. Finally, the design maps based on the two forms of dimensionless depletion current density provide straightforward means of assessing the trade-offs inherent in reducing mass transport losses within the electrode.

A fractal approach to modeling SOFC electrode mass transport is also presented in order to address microstructural details that are not captured by the analytical models described above. This modeling approach provides a basis for exploring the merits of applying fractal concepts toward modeling SOFC electrode microstructural performance and establishes the groundwork for a reduced order modeling approach to neutral species transport that is more sensitive to electrode microstructural characteristics than average porosity and tortuosity values. An accessible macro/micro modeling approach that couples a one-dimensional solution approach to finite element analysis is outlined and shown to provide insight into the impacts of microstructural detail within electrochemically active regions. The contribution of reaction zone microstructure to electrode mass transport performance is investigated, and a reduced order approach is presented as a means of capturing microstructural detail and incorporating it into continuum level electrode models.

The performance metrics and fractal modeling approach presented provide an accessible set of SOFC electrode design tools that are sensitive to interconnect geometry effects and microstructural characteristics. Compared to more common SOFC modeling approaches these approaches capture component level details and bridge levels of

modeling detail with reduced computational costs, as shown in Figure 1.3. The simplified nature and reduced computational cost of these approaches could allow for easier integration into higher level SOFC system models. Through this integration, the challenge of connecting the varying levels of detail applied in current SOFC modeling efforts can be addressed more effectively.

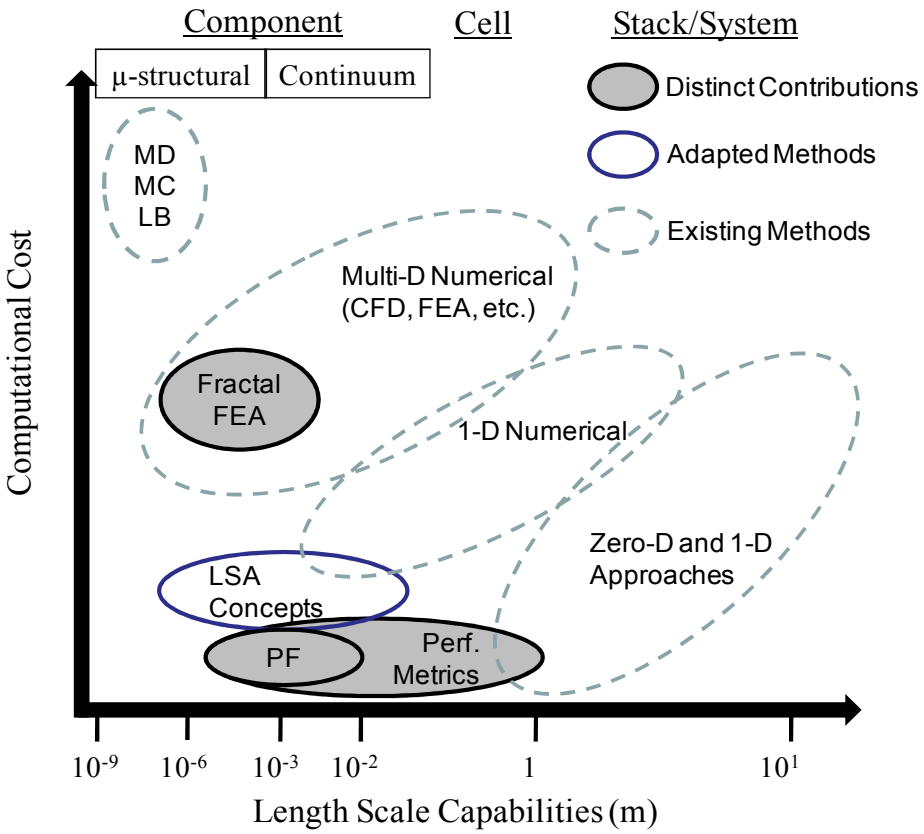

Figure 1.3 Levels of modeling detail covered by the models in the present work

CHAPTER 2

LITERATURE REVIEW

2.1 SOFC Background

Solid oxide fuel cells allow for the direct conversion on chemical energy to electrical energy through the electrochemical oxidation of hydrogen and reduction of oxygen. This process, shown in Figure 2.1, produces an electrical current that can be supplied to an external load. In general, SOFCs are composed of dual-purpose electrodes which allow mass and electronic transport separated by an electrolyte which allows for ionic transport, and their geometry can be described through four critical component layers: the anode (or fuel electrode), the cathode (or air electrode), the electrolyte, and the interconnect. Among SOFCs these layers are arranged in two prevalent cell geometries: planar (or flat plate) and tubular, as shown in Figure 2.2. Planar SOFCs, of particular interest in the present work, are typically classified by the component layer that provides structural support. These classifications are referred to as either electrolyte- or electrode- (i.e., anode- or cathode-) supported. Additionally, three manifolding arrangements are common among planar SOFC. These arrangements are based upon the arrangement of fuel and oxidant flow within the cell. Cell arrangements incorporating perpendicular fuel and oxidant flows are referred to as cross-flow. Arrangements incorporating parallel flows of fuel and oxidant moving in opposite directions are referred to as counter-flow. If fuel and oxidant flows are parallel and the in same direction the cell flow arrangement is referred to as co-flow. This latter manifolding arrangement is the more commonly studied SOFC geometry [7]. Similar distinctions can be made between the flow

arrangements of tubular SOFCs. For planar SOFCs parallel gas channel configurations (co-flow and counter-flow) are generally considered desirable from a performance standpoint as they result in higher electrical efficiencies and more symmetric temperature distributions within the cell than cross-flow designs [8-14]. Additionally, co-flow designs are expected to operate with lower mechanical stresses than counter-flow arrangements and would therefore be most desirable [12].

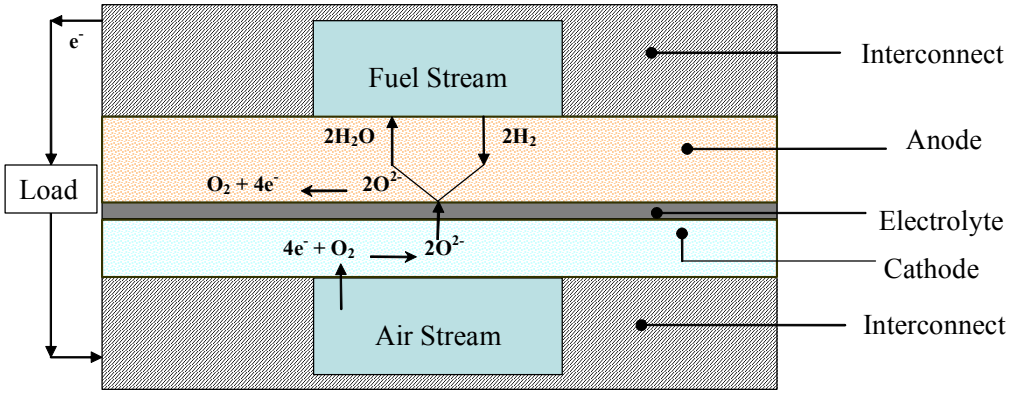

Figure 2.1 Basic planar SOFC cross-section and operation

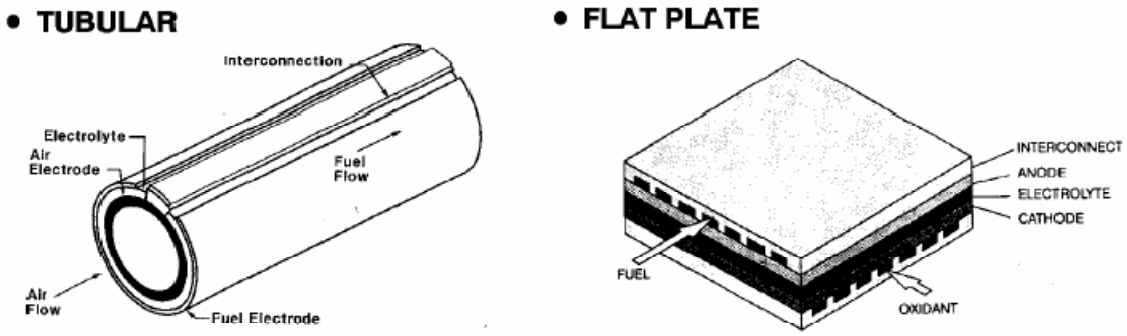

Figure 2.2 Tubular and flat plate SOFC geometries from [15], planar SOFC shown for a cross-flow arrangement

The limiting factors of SOFC performance are most commonly broken down into three categories of losses: activation, ohmic, and concentration. Activation losses are associated with the initiation of current generation from the cell electrochemical reactions that exist in a dynamic equilibrium at the open cell voltage (i.e. zero net current production). Ohmic losses in SOFCs are associated with the resistance to electronic conduction within the electrodes and interconnects and the resistance to ionic conduction in the electrolyte. Concentration losses refer to the decrease in performance caused by limitations on mass transfer from the reactant streams to the reaction sites at the electrode-electrolyte interfaces. Minimization of any of these above losses can result in enhanced SOFC performance. However, within operational cell geometries a balance between losses may be required. For example, optimized anode and interconnect geometry may be required to balance concentration and ohmic losses [16]. Operational parameters such as pressure, fuel concentration, and oxidant concentration can also be optimized to increase SOFC performance.

The minimization of losses within SOFCs can be achieved through several means. Activation losses can be decreased by increasing cell temperature to create more active chemical kinetics. Increased temperature also increases the ionic conductivity of SOFC electrolytes and thus reduces ohmic losses. However, the trend in SOFC technological development has shifted toward lower temperature operation as such operation offers the option of using less expensive and/or more reliable materials in stack design. Activation losses can also be reduced through the use of more active catalyst materials, such as platinum or palladium, or through increases in electrode surface area, which serves to increase the number of reaction sites, or triple-phase boundaries (TPBs), at and near the

bulk electrode-electrolyte interfaces. Ohmic losses can be reduced through the creation of thinner electrolytes or electrodes and interconnects with higher electronic conductivity. Concentration losses are typically reduced through operational parameters and proper control of electrode porosity [17].

2.2 Porous Electrode Composition and Microstructure

Solid oxide cells are composed of porous hydrogen and oxygen electrodes separated by a dense ceramic electrolyte that is typically composed of yttria-stabilized zirconia (YSZ). SOFC anode materials must meet three general criteria. Most important among these criteria is that the anode materials perform well in the reducing environments encountered during operation. Additionally, the anode must resist reaction with sulfur, which is common in potential fuels like natural gas, and demonstrate a good thermal expansion match with other SOFC component layers [18, 19]. Nickel is the most common catalyst used in SOFC anodes, being combined with YSZ to form the porous anode structure. SOFC cathode materials must generally exhibit high electronic conductivity, good ionic conductivity, and be non-reactive with the electrolyte and interconnect. Furthermore, the materials used in the cathode must act as an oxygen electro-reduction catalyst. Cathode materials are typically semi-conducting oxides, with lanthanum deficient strontium doped manganite (LSM) being the most common. A layer with a balanced proportion of LSM and YSZ (in the range of 50:50) may also be used at the cathode-electrolyte interface to create an interfacial material that is an effective mixed ionic-electronic conductor (MIEC) [18, 19]. This MIEC region allows for ionic conduction further into the cathode and extends the reaction zone where oxygen is

reduced. In addition to LSM many p-type conducting perovskites capable of mixed ionic-electronic conduction can be used as cathode materials. Such materials that are strong MIECs could prove critical to the achievement of lower temperature SOFC operation. Finally, several n-type semi-conductors, such as lanthanum strontium ferrite and lanthanum strontium cobaltite, may allow production of cathodes with enhanced electrocatalytic properties [17].

SOFC anodes may be produced in button-cell form by die-pressing a mixture of NiO powder, YSZ powder, and an organic pore former [20-22]. Larger anodes can be produced by tape casting layers from slurries of NiO, YSZ, and pore former, which are laminated together to form a "green" anode of desired thickness. These anodes can be screen-printed with a thin YSZ film to form the electrolyte layer, and the resulting structure is then sintered at high temperature, a process which removes the pore former and produces an anode-electrolyte assembly with porous NiO-YSZ structure. The NiO within the anode-electrolyte assembly is subsequently reduced at high temperature to produce the desired porous Ni-YSZ anode structure [18, 20-22]. SOFC cathode layers are often applied to this anode-electrolyte structure in a two step process. First, a 50/50 LSM and YSZ layer is applied to the anode-electrolyte assembly. This assembly is then sintered to form the previously mentioned MIEC interfacial layer. A second layer of LSM is then applied and sintered to form the remainder of the cathode [18, 19].

It is commonly assumed that porous SOFC electrodes resulting from the general processing steps above have relatively consistent microstructural characteristics, such as porosity and tortuosity. However, these structures are inherently random and subject to variations in microstructure. Furthermore, electrodes with tailored microstructure may

allow for enhanced mass transfer performance. These tailored, or functionally graded, microstructures include electrodes designed with discrete layers produced using common approaches and electrodes produced using processes that create continuously varying microstructures, including chemical vapor deposition and plasma spraying techniques [23-25]. Recently, freeze-tape casting has been investigated for the production of dendritic pure YSZ structures, impregnated with Ni catalyst particles, that can be employed as electrodes [26]. These functionally graded designs may allow for production of electrodes that are electrochemically active throughout the entire thickness. This possibility of volumetric activity stands in contrast to common, relatively uniform, electrodes which typically have electrochemically active regions only near the bulk electrode-electrolyte interface [21].

2.3 Common SOFC Modeling Approaches

As noted in the previous chapter, the modeling of SOFCs spans many levels of detail and requires a trade-off between computational cost and fidelity of results. Translating the fidelity of numerical component level models to a cell or stack level is often a difficult task. At the cell level, it is common for models to treat the distribution of temperature and reactant species as uniform across the thickness of the electrode structure. Modeling efforts that have attempted to include greater detail on transport phenomena within the electrode have involved general expressions for cell concentration and ohmic polarization and have often relied upon a one-dimensional characterization of mass transport phenomena across the electrodes [10, 27-29]. Cell level analyses seeking a more detailed description of transport phenomena at the continuum electrode level

typically employ FEA and CFD to ascertain the multidimensional characteristics of SOFC transport phenomena [2, 8, 9, 11, 30-34]. For example, Khaleel et al. [11] developed a routine for interfacing an electrochemical model with an FEA model that is capable of accounting for spatial variation of temperatures within the cell. However, this work does not focus on variations through the electrode thickness. Ferguson et al. [9] apply CFD techniques toward modeling thermal, mass, and electronic transport within solid oxide fuel cells and demonstrate the effects of interconnect rib size on hydrogen and voltage distributions within the electrode. Ohmic losses are shown to be reduced by broader interconnect ribs. However, the interconnect is shown to reduce hydrogen concentration in regions not directly beneath the anode-fuel stream interface. Ji et al. demonstrated similar effects on cathode mass transport [33].

SOFC models that focus on the continuum transport of electronically neutral species (i.e. gaseous reactant species that are not charged such as H_2, O_2, and H_2O) within the electrode include application of one of three common models: Fick's model, the Stefan-Maxwell model, and the dusty-gas model (DGM) [32, 35-38]. The first and last of these approaches are of particular interest in the present work. Fick's model typically assumes binary diffusion and accounts for the effects of the porous medium by the use of an effective diffusion coefficient. For SOFC electrodes with small enough pores, this effective diffusion coefficient can be further modified to account for Knudsen diffusion. In the present work Fick's model is also referred to as the potential flow model, since under proper conditions the distribution of gaseous species in an SOFC electrode can be described using the Laplace equation [39]. The dusty-gas model is a special extension of the Stefan-Maxwell model that accounts for the gas-solid interaction by abstracting the

solid matrix as a large, immobile species or "dust" [40, 41]. The DGM has been successfully implemented for modeling SOFC electrode performance in many instances and has demonstrated enhanced modeling capabilities when compared to Fick's model [36-38]. The dusty-gas approach is considered as a state-of-the-art benchmark for the other models explored in the present work.

Microstructural-level models can be employed for more detailed modeling of transport phenomena within the electrodes. The concept of extended surfaces has been used to model ionic transport phenomena at the microstructural level. Liu used an extended surface visualization to develop an equivalent circuit model of the performance of porous MIEC cathodes [42]. Around the same time Tanner, et al. abstracted the anode-electrolyte interface as a region of YSZ corrugations wrapped by a nickel catalyst [43]. This model was applied to examining the potential distributions within the YSZ structures.

Packed sphere models of SOFC electrodes have gained more significant attention compared to these extended surface models [44-50]. In these models the dispersion of catalyst and YSZ particles within the composite electrode is modeled discretely, accounting for individual particle resistances. Focusing primarily on electrode property predictions, such models can address the performance effects of detailed microstructural parameters including particle size, electrode composition and porosity. Additionally, the effects of processing can be considered. For example, Schneider et al. applied the discrete element method to generate packings of monosized particles which are numerically sintered to simulate an electrode microstructure and an associated network of resistances [46, 48]. Like detailed models at the continuum electrode level a high

computational cost is associated with these packed sphere approaches. Furthermore, with the exception of recent work by Cannarozzo et al. and Zhu and Kee, these packed sphere models do not tend to consider the transport of neutral species.

Recently, efforts have been made at more detailed microstructural visualization and reconstruction that go beyond the more basic packed sphere approaches [51-53]. Wilson et al. reconstructed the pore, nickel, and YSZ phases of an SOFC anode based on focused ion beam-scanning electron microscopy scans and measured the triple phase boundary length and tortuosity within a segment of the anode [53]. Greater consideration has been given to neutral species transport in more detailed microstructural geometry by Izzo et al. [51, 52]. Mercury intrusion porosimetry and X-ray computed tomography were used to characterize pore size distribution. Mass transport is modeled using the DGM, with diffusion coefficients calculated based on the pore size distribution, and using the Lattice Boltzmann method. These works demonstrate variations within pore structure in SOFC anodes and expand upon the work of Joshi et al. that explored two-dimensional transport of neutral species within SOFC electrodes, emphasizing electrode geometry on the microstructural level SOFC mass transport [54, 55]. The DGM is applied toward modeling one-dimensional transport within the anode of a tubular SOFC. The more detailed Lattice Boltzmann method focuses on the microstructural level and entails a heavy computational cost, requiring the application of multiple parallel processors over extended periods of time.

In addition to the challenge of maintaining multi-scale model fidelity there are several assumptions employed in the modeling of SOFCs that require further consideration. The assumption of one-dimensional transport within the electrodes, noted above, has been

reviewed using analytical and numerical techniques. Continuum level transport phenomena in SOFC electrodes have been addressed by the author using analytical models of electrode behavior that focus on a unit cell cross-section [6, 39, 56]. These models use a potential flow description of mass and electronic transport within the electrodes and are capable of discerning some key insights involving trade-offs between ohmic and concentration losses as well as cell operation near limiting current densities. However these modeling attempts rely on the neglect of pressure gradients, the assumption of planar reaction zones, and the application of effective (i.e. tuned or fitted) microstructural parameters.

Neglecting pressure gradients has received attention lately as a potential source of error in SOFC models. Most notably Ni et al. compared models of SOFC electrode mass transport to demonstrate the importance of pressure gradients on reactant concentration distributions within SOFC anodes and cathodes [57]. Pressure gradients were calculated from a method developed by Zhu and Kee [49]. For the anode side methane reformate was examined, and it was determined that pressure gradients be considered in models of SOFCs operating on hydrocarbon fuels. For a binary fuel mixture of hydrogen and steam Washak et al. compared the extended Fick's model, which includes a pressure gradient term, and the dusty-gas model for gas transport in an SOFC with an interdigitated flow field design [37]. This flow field arrangement results in convective and diffusive mass transport effects within the anode. However, results of eight modeling scenarios showed significant difference between the models only when hydrogen concentration is low, concentration polarization is high, and pore sizes in the anode are small.

Estimations of reaction zone size on the order of 10 μm are often used to justify treating reactive regions within the electrode as planar [21]. The extension of active regions away from the electrode-electrolyte interface has been addressed through application of the packed sphere models and the use of discrete reaction zone domains in continuum level models. Packed sphere models of SOFC anodes that do not consider the impact of reactant gas transport estimate reaction zones that extend 100-150 μm from the electrode-electrolyte interface. Considering the effects of gas transport within such models can result in reaction zone sizes ranging from 10-50 μm [44-46, 49]. Through application of the Stefan-Maxwell approach Hussain et al. explored a multi-component mass transfer model within the SOFC anode inclusive of a discrete reaction volume near the anode-electrolyte interface. This discrete reaction zone was proposed to have a smoothing effect on the concentration profile by reducing concentration gradients at the anode-electrolyte interface when compared to the common constant flux boundary condition set when assuming a planar reaction zone [35].

The neglect of pressure gradients and the assumption of planar reaction zones have received less attention than the use of effective tortuosity values, which are commonly applied in SOFC models to accurately predict performance in diffusion limited scenarios. These effective tortuosity values are often significantly larger than experimentally demonstrated tortuosities for SOFC electrodes [21]. It has been suggested that this inaccuracy in diffusion limited scenarios may result from surface phenomena near the electrode-electrolyte interface. However, studies demonstrating such effects have relied on experiments using pattern electrodes that cannot account for diffusion within the pores of the electrodes [58, 59]. Shi et al. incorporated these surface diffusion and competitive

adsorption effects into a two-dimensional model of an SOFC button-cell, with dusty-gas model (DGM) used to model gas transport within the porous electrodes. Although a thorough multi-physics modeling approach was applied, the tuning of parameters to a base case model is still required for results to agree with experimental polarization behavior. Furthermore, even with tuned parameters some cases require adjustment of the tortuosity to artificially high levels [60]. As an alternative, Lee et al. proposed a means of predicting SOFC performance, including concentration polarization and limiting current, based on switching the reaction mechanism that limits transport between hydroxyl ion oxidation and hydrogen adsorption. The former mechanism was shown to match experimental predictions in most ranges of SOFC operation but accuracy decreased in limiting current situations. Instead, hydrogen adsorption was suggested as a limiting factor that causes an increase in activation polarization near limiting currents. The role of surface diffusion proposed by Williford et al. and Shi et al. was suggested to overestimate diffusion resistance by applying surface diffusion coefficients over the whole electrode and not just near the active surface or TPB [61].

2.4 Fractal Approaches for Gas Transport Modeling

While the DGM is considered to be the state-of-the-art approach for modeling gas transport in porous media and is widely used in SOFC modeling, it should be noted that there is some debate on its appropriateness for modeling transport in porous media [62-64]. Of particular note, the cylindrical pore interpolation model (CPIM) developed by Young and Todd essentially interpolates between the gas flow in the continuum and Knudsen regimes in a manner similar to the DGM. This approach is intended for

application as an alternative means of modeling SOFC gas transport. While claiming a more straightforward description of multi-component flow, the resulting model still relies on application of an empirical tortuosity factor [63, 64].

The challenge presented to SOFC modeling by the application of effective parameters, tortuosity in particular, is indicative of a broader issue in modeling gas transport porous media. The physical pore structure is generally abstracted away by most models, as noted before in the explanation of the dusty-gas approach. The tortuosity is then applied as a fitting parameter to account for the pore structure. However, this fitting approach may result in the tortuosity enshrouding key physical phenomena within a parameter describing pore structure. Specifically, it has been noted that the tortuosity of porous catalysts has demonstrated dependence on physical factors including temperature, pressure, and Thiele modulus [65].

To better discern the role of the physical pore structure, transport network models may be applied to simulate the connection between individual pores. However, such approaches often rely upon treating pores as simplified cylindrical capillaries [65, 66]. Fractal approaches for describing porous media may also be applied and can allow for simulation of more complex pore geometry with respect to pore surface and network properties.

In the mathematical sense, a fractal is a countable system that possesses the same general geometry regardless of scale. This characteristic is also referred to as self-similarity or scale symmetry [65, 67, 68]. The scaling relation between each part of the system is described through the fractal dimension, a quantity that is limited by the Euclidean dimension of the space occupied by the fractal (i.e., a two-dimensional fractal

requires a fractal dimension between one and two). Systems that can be described using fractal geometry include natural coastlines, turbulent flows, and porous media [65, 67, 68]. For these finite systems, fractal geometric descriptions may be applied if the system can be considered statistically self-similar or is treated as prefractal. The former description applies to geometries that are fractal in an average sense, with a sufficiently broad range of feature sizes present within the system [65, 69]. The latter description applies to a finite size system in which feature size obeys a scaling relation similar to a mathematically fractal system [70].

Fractal approaches for describing gas transport in porous media can be generally classified as focusing on medium morphology and pore network topology. Such works often focus on transport within porous catalysts. Through application of a morphological approach fractal structures can serve as templates for a catalyst's pore structure and allow for the more detailed examination of diffusion phenomena within pores and particle interaction with the catalyst surface [70-79]. In contrast, topological approaches seek to describe particle trajectories as fractal curves with path lengths greater than apparent transport path lengths [80, 81]. The first of these approaches is of particular interest in the present work.

Methods of accounting for the effect of irregular surface geometry on catalyst activity have been developed by Coppens and colleagues for systems operating in the Knudsen diffusion regime [71-74]. In these works, the structure of a porous catalyst is treated as a "fjord tree" similar to a natural coastline, where smaller pores branch off from a larger main pore. A distribution of accessibility for reacting molecules is proposed to result from this branched structure, and a means of modifying the Knudsen diffusion coefficient

is suggested based on the size of the smallest accessible fjord within the tree. In later works self-diffusion and transport diffusion were compared, and it was proposed that self-diffusion is primarily affected by the surface irregularity of the pore [73]. However, depending on the relation between pore length and feature size transport diffusivity may be impacted by surface irregularity [74].

Using simulations of ballistic particle trajectories in prefractal pores Santra and Sapoval demonstrated that pore surface irregularity can impact catalytic efficiency by increasing the active surface area and the specific yield of a catalyst through increased collision frequency [70]. The first of these effects can be considered as a direct scaling effect that the rough surface has on the reaction rate while the second relates to the accessibility of the fractal surface as influenced by its microstructural characteristics. The influence of scaling and accessibility effects is described by Sapoval and colleagues through a concept known as the Land Surveyor Approximation [76, 78, 79, 82]. This approach allows for the description of these surface roughness effects based on the relation between diffusive transport and surface reaction rates. When the rate of reactant consumption at the surface is sufficiently lower than the rate of diffusion in the catalyst the reaction rates near the catalyst surface, and the corresponding catalytic efficiency, scale based on the ratio of the actual surface length (or area) and the apparent surface length (or area). In diffusion limited scenarios this scaling relation is dependent on the microstructural characteristics of the rough surface [78, 79]. A variety of numerical approaches are applied in analyzing the effects. For example, Sapoval et al. explore these phenomena for rough surfaces simulated using a basic deterministic fractal geometry using finite element analysis within the irregular fractal pores [78], and Andrade et al.

apply a nonequilibrium molecular dynamics approach to modeling transition and Knudsen diffusion scenarios [75]. While the majority of the work on the Land Surveyor Approximation treats fully activated surfaces with simplified geometric characteristics, extension to modeling catalytic surfaces with inactive regions has been broached [82]. Additionally, it is noted that application of the LSA to more complex structures can be made based on the general concept of a scaling relation between apparent and actual surface characteristics [78].

Fractal topology models of porous media are often applied toward the development of a refined definition of tortuosity [80, 81]. Zhang and Liu developed a fractal expression for the tortuosity of a porous catalyst pellet. In this case, the fractal dimension of the average particle trajectory is the only tuned parameter of the model [81]. The argument can be made that such an approach merely introduces a new fitting in lieu of the tortuosity. However, the requirements of fractal geometry in this description place strict limits on the range of values that such a fractal dimension can take [67, 68]. Thus, the convolution of geometry with other physical parameters may be alleviated through fractal definitions of the tortuosity.

For flows in porous media that are influenced by pressure gradients a fractal permeability may be defined assuming the pore size distribution covers an acceptable range. Yu and Liu define fractal permeabilities for single and two-phase fluid flow in a porous medium with a ratio of maximum to minimum pore size of at least 10^{-2}. This approach states fluid flow rates according to the Hagen-Poiseuille Law. The permeability is estimated by first integrating individual capillary flow rates over the range of pore sizes to find the total flow rate for the medium and then substituting this total flow rate into

Darcy's Law [69]. Shi et al. have adapted this approach for gas transport in the gas diffusion layers of polymer electrolyte membrane (PEM) fuel cells by defining flow rates based on the Adzumi equation, which essentially superposes Poiseuille and Knudsen flows [83].

In addition to their development of a fractal expression of permeability for PEMFC gas diffusion layers Shi et al. have also applied a fractal approach for describing the thermal conductivity of PEMFC gas diffusion layers. These two works serve as the most direct application of fractal geometry concepts to transport phenomena in fuel cells [83, 84]. However, fractal approaches have also been applied in the characterization of carbon materials used in PEMFC electrocatalyst supports [85], and Park et al. have proposed the application of fractal concepts within the general area of electrochemical systems, particularly with respect to electrode structures. In such application fractal structures are considered to provide a means of spreading reaction sites throughout a given volume and reducing limitations associated with mass transfer [86]. These nascent applications of fractal concepts to electrochemical systems and the established application of these concepts to the study of similar porous catalyst structures provide motivation for the extension of fractal approaches to SOFC modeling.

CHAPTER 3

CONTINUUM COMPONENT LEVEL MODELS: THEORY

Numerical SOFC models are powerful design tools when focusing on a specific level of detail. Focusing on variations in temperature and pressure within an electrode can be done numerically in a straightforward manner, especially with the advent of user friendly multi-physics software packages. However, detail is difficult to preserve when translating numerical component level models to a cell or stack level. Detailed cell-level CFD models can require almost 500,000 computational cells to accurately capture multi-dimensional variations throughout the SOFC component layers [32]. Finite element models present similar challenges when attempting to retain proper element aspect ratios in meshes that span multiple length scales within the component layers.

The advantage of developing and applying simplified analytical component models, as will be demonstrated, lies in their ability to retain detail and integrate into higher level models without exacting significant computational cost. Furthermore, if direct integration of analytical component models into higher level models is not desired, the expressions developed for the analytical model can be directly manipulated to produce dimensionless correction factors and performance metrics that could not be as easily produced from running "numerical experiments." Thus, analytical models can provide straightforward insights that are more readily available than insights from numerical models. In the present chapter performance metrics for SOFC cross-sectional design are developed based on existing potential flow models. Numerical models based on the dusty-gas approach are also presented for comparison to these analytical models.

3.1 Mass Transport Models

Two common approaches applied toward modeling neutral species transport in SOFC electrodes are Fickian models (also referred to as potential flow models) and the dusty-gas model for transport in porous media. The first of these approaches allows for analytical solution, while the second, implemented numerically, provides a more detailed treatment of the gas-solid interaction. The distinction between these models lies in the definition of molar flux within the porous medium, as shown for a binary mixture in Equations 3-1 and 3-2. Terms accounting for the influence of pressure gradients within the electrodes are neglected for simplified comparison. The binary diffusion coefficient for the binary gas mixture, D_{ij}, is defined using the Chapman-Enskogg model as outlined by Reid et al. [87]. The variables ε and τ are the anode porosity and tortuosity, respectively. Their ratio is the anodic permissivity, which is incorporated to create an effective binary diffusion coefficient as defined in [21]. This effective diffusion coefficient approach is also applied to the Knudsen diffusion coefficient in the dusty-gas model.

$$N_i = -D_{ij}^{eff} \nabla C_i \tag{3-1}$$

$$N_i = -\left[\frac{1 - \alpha y_i}{D_{ij}^{eff}} + \frac{1}{D_{ik}^{eff}} \right]^{-1} \nabla C_i \tag{3-2}$$

$$\alpha = 1 - \sqrt{M_i / M_j}$$

For SOFC electrode models these flux definitions are applied in the equation for conservation of species with advection in the porous electrode neglected, Equation 3-3. When subject to the assumptions of steady-state behavior and no internal chemical reactions this equation is simplified to Equation 3-4.

$$\varepsilon \frac{\partial C_i}{\partial t} = -\nabla \cdot N_i + r_i \tag{3-3}$$

$$\nabla \cdot N_i = 0 \tag{3-4}$$

3.1.1 Fickian Potential Flow Models

A unit cell for an SOFC is herein defined as a single pair of co-flow reactant channels which encompass the corresponding *positive electrode/electrolyte/negative electrode* (P-E-N) tri-layer, as shown in Figure 3.1. The present work focuses on a cross-sectional region of the electrode components of this fundamental element of a full co-flow cell arrangement. For the models developed, the lengths *a* and *b* are defined as half the total unit cell width and half the fuel stream width, respectively. A symmetry boundary condition is applied about the centerline of the reactants channels to further simplify the problem geometry. Finally, a dimensionless length fraction (*LF*) is defined to compare the gas stream contact length to the total unit cell length. This dimensionless term can also be thought of as the ratio of gas contact length (source) to electroactive contact length (sink), which for continuum component level models is an apparent contact length corresponding to the unit cell width.

$$a = \frac{L_{Total}}{2}; \quad b = \frac{L_{GS}}{2}; \quad LF = \frac{b}{a} = \frac{L_{GS}}{L_{Total}} \tag{3-5}$$

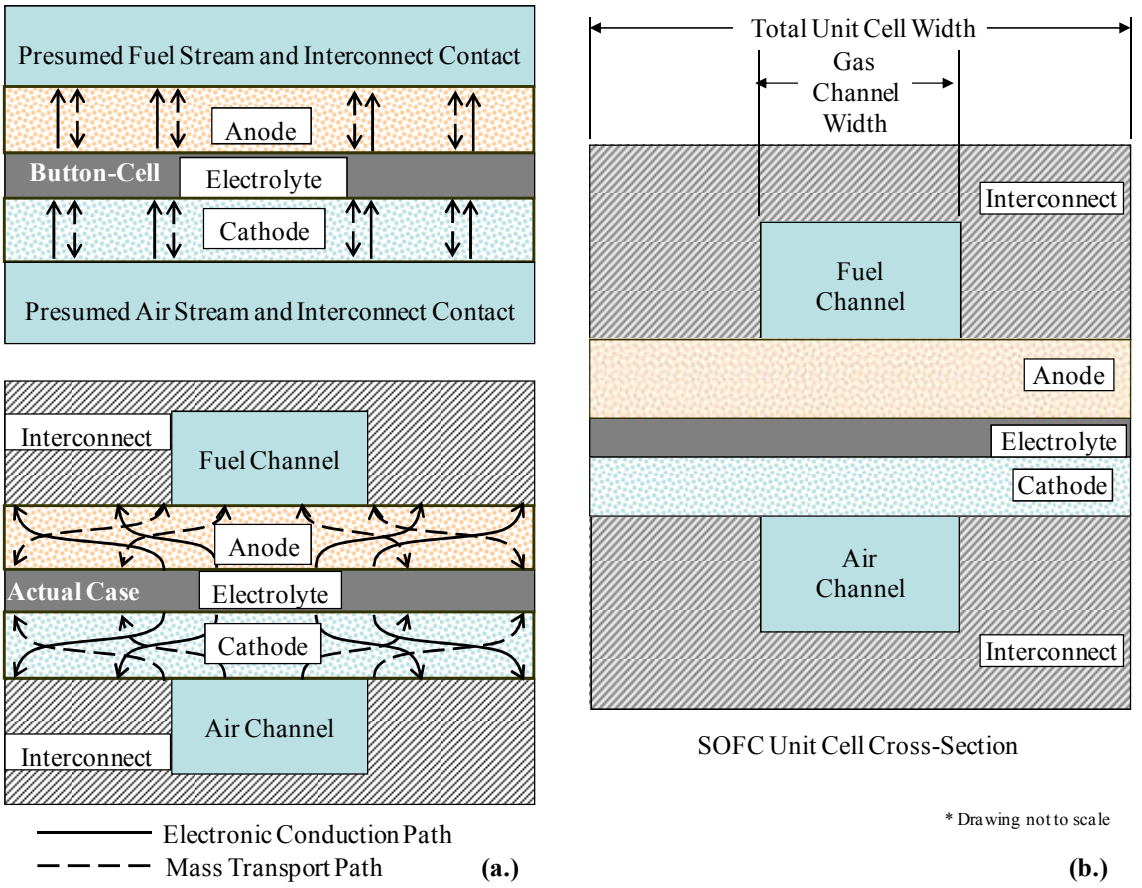

Figure 3.1 Comparison of the one-dimensional button-cell approximation and actual two-dimensional transport for component layer mass and electronic transport (a.) for a common SOFC unit cell cross-sectional geometry (b.)

When applying the Fickian approach two-dimensional diffusive mass transport within SOFC electrodes can be described in a simplified form using analytic solutions to the Laplace equation. These solutions have been developed from boundary value problems describing the anode and cathode partial pressure distributions within a rectangular domain defined by a unit cell cross-section, as shown in Figure 3.2. This general domain is also explored for the dusty-gas models discussed later.

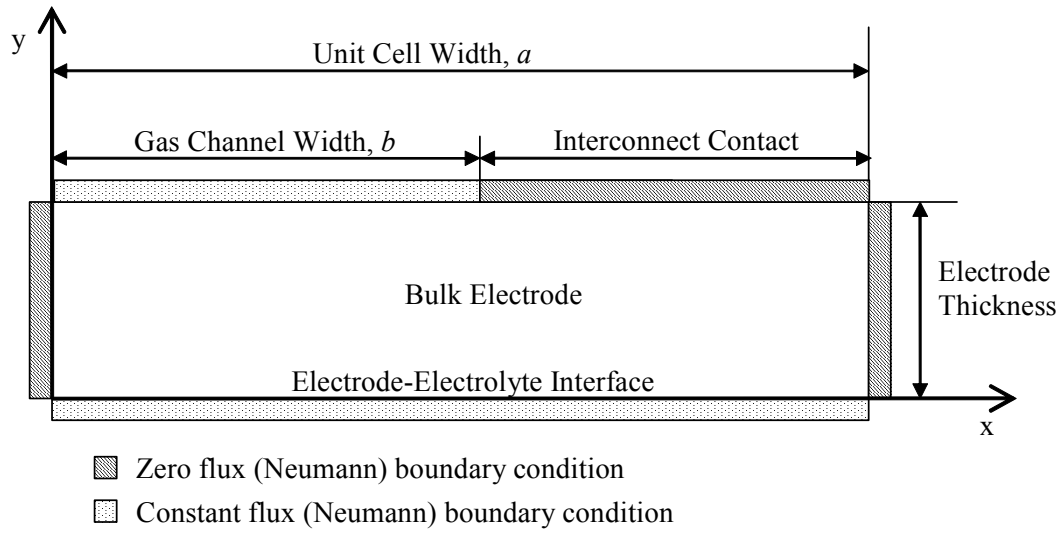

Figure 3.2 General domain studied for neutral species mass transport model development, the bulk electrode may be the cathode or anode in contact with oxidant or fuel channels, respectively

3.1.1.1 Anode Mass Transport Model

The application of a simplified potential flow (Fickian) approach to the partial pressure problems is made possible primarily through the basic assumptions of equimolar counterdiffusion of hydrogen and steam within the anode, a stationary medium within the cathode, and relatively thin reaction zones (~10 μm) at the electrode-electrolyte interfaces [21]. These assumptions are stronger for thicker electrode geometries, such as the anode of the more common anode-supported SOFC arrangement. For thinner electrodes the effects of distributed reactions within the porous medium may warrant further consideration. In the present chapter however, this requirement is relaxed to allow for a general investigation of electrode transport performance.

A uniform partial pressure across the gas channel cross-section is also assumed for the reactant gas species, due to anticipated low resistance to convective mass transport within

the gas channel when compared to resistance to diffusion within the electrode. This assumption is corroborated through a brief comparison of the diffusive and convective mass transfer resistances, as defined in Equations 3-6 and 3-7.

$$R_{Diff} = \frac{t_{an}}{D_{H_2-H_2O} A_s} \frac{\tau_{an}}{\varepsilon_{an}} \tag{3-6}$$

$$R_{conv} = \frac{d_h}{D_{H_2-H_2O} \cdot Sh \cdot A_s} \tag{3-7}$$

Here, A_s is the surface area of the anode in contact with the fuel channel, and d_h is the hydraulic diameter. It should be noted that the binary diffusion coefficient for the hydrogen-steam mixture is used in Equation 3-7 because the convective mass transfer resistance relates to diffusion within the fuel stream, which would have a permissivity of 1.0.

For a standard flow channel width on the order of 1 mm and a nominal height of 1 mm, the ratio of convective resistance within the flow channel to conductive resistance within the electrode can be found using published Sherwood number values [88]. The convective mass transfer resistance within the fuel channel is 2-3% of the diffusive mass transfer resistance. Thus for the present model, the diffusive resistance is considered to be the dominant mass transfer resistance, and the reactant partial pressure at the channel centerline (x = 0, $y = t_{elec}$ in Figure 3.2) is treated as equal to the gas stream partial pressure.

The boundary value problem for the hydrogen partial pressure consists of the Laplace equation with constant species flux boundary conditions specified at the anode-electrolyte

and anode-fuel stream interfaces. These boundary conditions, shown in Equation 3-9 and 3-10, are based upon an *a priori* assumption of uniform flux at the anode-electrolyte and anode-fuel stream interfaces of a localized cross-sectional region of the unit cell. The scaling factor, *a/b*, in Equation 3-10 is the result of species conservation and the reduction in area between the respective interfaces. A zero species flux boundary condition is specified at the anode-interconnect interface. A corresponding problem can be defined for the steam partial pressure by reversing the sign of the boundary conditions given in Equation 3-9 and 3-10. The general domain studied in the development of the anode partial pressure model is shown in Figure 3.2. A similar domain is used in the development of the cathode oxygen transport models.

$$\frac{\partial^2 p_{H_2}}{\partial x^2} + \frac{\partial^2 p_{H_2}}{\partial y^2} = 0 \tag{3-8}$$

$$\frac{\partial p_{H_2}}{\partial y}(x,0) = \frac{R_u T}{2FD_{H_2-H_2O}} \frac{\tau_{an}}{\varepsilon_{an}} i'' = B_{0,an} \tag{3-9}$$

$$\frac{\partial p_{H_2}}{\partial y}(x,t_{an}) = \begin{cases} \dfrac{R_u T}{2FD_{H_2-H_2O}} \dfrac{a}{b} \dfrac{\tau_{an}}{\varepsilon_{an}} i''; & 0 < x < b \\ 0, & b < x < a \end{cases} \tag{3-10}$$

$$\frac{\partial p_{H_2}}{\partial x}(0,y) = 0\,,\ \frac{\partial p_{H_2}}{\partial x}(a,y) = 0 \tag{3-11}$$

The solution to the hydrogen partial pressure problem is outlined in Equations 3-12 and 3-13. This solution is derived for a general SOFC electrode in Appendix A. A similar solution can be defined for the steam partial pressure distribution [6].

$$p_{H_2}(x,y) = p^0_{H_2} - B_{0,an}(t_{an} - y) - \sum_{n=1}^{\infty} A_{n,an}\left[\cosh(\lambda_n t_{an}) - \cosh(\lambda_n y)\cos(\lambda_n x)\right] \tag{3-12}$$

$$A_{n,an} = \frac{2B_{0,an}\sin(\lambda_n b)}{n\pi\lambda_n \sinh(\lambda_n t_{an})}\left(\frac{a}{b}\right); \quad \lambda_n = \frac{n\pi}{a} \tag{3-13}$$

For a button-cell case ($b = a$) the series term in this solution is eliminated, and the expression for the partial pressure of hydrogen takes on the standard one-dimensional form.

$$p_{H_2}(y) = p^0_{H_2} - \frac{i'' R_u T}{2FD_{H_2-H_2O}p}\frac{\tau_{an}}{\varepsilon_{an}}(t_{an} - y) \tag{3-14}$$

The solution for electrode reactant distributions outlined in Appendix A provides a straightforward means of assessing the role of interconnect geometry in SOFC electrode mass transport. However, calculations based on these electrode mass transport models will become less accurate as the electrode thickness is decreased. This reduced accuracy has two sources: the extension of the reaction zone away from the electrode-electrolyte interface and the variation of current along the electrode-electrolyte interface. The first of these sources was noted above. The second of these sources is linked to the influence of localized current variation along the electrode-interconnect interface.

For thin electrodes, the constant voltage along the electrode-interconnect interface will impact the validity of the constant molar flux boundary condition shown in Equation

3-9. At the transition point between the gas channel and interconnect contact the shift from an electronically insulated boundary with variable voltage (along the gas channel) to an electronically conducting boundary at constant voltage (along the interconnect) results in a singularity that will cause a localized increase in current density. As the electrode thickness is reduced this local increase in current density at the electrode-interconnect interface will begin to influence the current density at the electrode-electrolyte interface. In turn, the molar flux at the interface, which is proportional to the current density, will begin to vary. This variation in molar flux will become more pronounced as the electrode thickness is reduced.

For thin electrodes, the reduced accuracy of the planar reaction zone assumption, which is due to a greater percentage of the electrode being electrochemically active, and the potential for localized current density variation at the electrode-electrolyte interface suggest that insights gained should be treated as qualitative. In future work these findings may be compared to more detailed electrode models that couple mass and electronic transport to a greater degree. While the results and design insights for thin electrodes presented in later chapters are considered qualitative, the performance impacts of cross-sectional geometry for thin electrodes are still expected to be significant. Such impacts are indicated by the more detailed modeling results of Ji et al. [33].

3.1.1.2 Cathode Mass Transport Model

For the cathode, the stationary medium and thin reaction zone assumptions are applied. The only diffusing species in this case is oxygen. The nitrogen, present when air is used as the oxidant, is treated as stagnant. The stationary medium assumption, as

discussed below, produces a conservative, lower estimate of the oxygen partial pressure distribution within the cathode. This conservative estimate of oxygen partial pressure causes a computational "safety factor" to result when designing for reduced cathodic concentration polarization.

For the cathode, the stationary medium approximation can be supported by comparing the influence diffusive and convective mass transport, as described by the convection-diffusion equation**,** Equation 3-15. Convective mass transport is described by the molar average velocity, defined in Equation 3-16a. The magnitude of the molar average velocity can be estimated based on the molar flux of oxygen within the cathode (Equation 3-16b). The magnitude of this velocity can be used to calculate a mass diffusion Peclet number, which quantifies the influence of convective and diffusive mass transport in the cathode. The comparison of these convective and diffusive influences via the Peclet number suggests that diffusion dominates mass transport within the cathode. The negligible influence of the mass average velocity term justifies the stationary medium approximation.

$$\vec{J}_{O_2} = -D_{O_2-N_2}\frac{\varepsilon_{ca}}{\tau_{ca}}\nabla C_{O_2} + \frac{C_{O_2}}{C_{tot}}\vec{J}_{O_2} \tag{3-15}$$

$$\vec{v} = \frac{\vec{J}_{O_2}}{C_{tot}} \tag{3-16a}$$

$$|\vec{v}| = \frac{i''}{4FC_{tot}} \tag{3-16b}$$

$$Pe_m = \frac{L_c \cdot |\vec{v}|}{D_{O_2-N_2}} \tag{3-17}$$

The characteristic length, L_c, is defined as the ratio of cathode cross-sectional area to the perimeter of the cross-section, a comparison of diffusive and convective (molar average velocity) influences can be made. This characteristic length definition is chosen to avoid the requirement of an *a priori* designation of the cathode dimension that would influence mass transport the most. For thin cathodes this definition treats the unit cell width as the primary dimension in the characteristic length.

When the stationary medium assumption is not applied, the distribution of oxygen within the cathode is described by Equation 3-15. For the one-dimensional case solution of this convection-diffusion equation is straightforward, as demonstrated below. However, to observe multi-dimensional effects numerical solution is necessary.

The two-dimensional problem for cathode oxygen transport can be solved analytically if the stationary medium assumption is applied over the general domain shown in Figure 3.2. This problem is established in the same manner as the hydrogen and steam problems. However, the boundary conditions at the horizontal boundaries require modification to account for the differing stoichiometric coefficient of oxygen, as shown in Equations 3-18 and 3-19.

$$\frac{\partial p_{O_2}}{\partial y}(x,0) = \frac{R_u T}{4FD_{O_2-N_2}} \frac{\tau_{ca}}{\varepsilon_{ca}} i'' = B_{0,ca} \tag{3-18}$$

$$\frac{\partial p_{O_2}}{\partial y}(x,t_{ca}) = \begin{cases} \dfrac{R_u T}{4FD_{O_2-N_2}} \dfrac{a}{b} \dfrac{\tau_{ca}}{\varepsilon_{ca}} i''; & 0 < x < b \\ 0, & b < x < a \end{cases} \tag{3-19}$$

The resulting cathode oxygen pressure distribution is given in Equation 3-20 and 3-21. As for the hydrogen distribution, this solution follows the form of an electrode partial pressure distribution outlined in Appendix A.

$$p_{O_2}(x,y) = p^0_{O_2} - B_{0,ca}(t_{ca} - y) - \sum_{n=1}^{\infty} A_{n,ca}\left[\cosh(\lambda_n t_{ca}) - \cosh(\lambda_n y)\cos(\lambda_n x)\right] \tag{3-20}$$

$$A_{n,ca} = \frac{2B_{0,ca}\sin(\lambda_n b)}{n\pi\lambda_n \sinh(\lambda_n t_{ca})}\left(\frac{a}{b}\right); \quad \lambda_n = \frac{n\pi}{a} \tag{3-21}$$

In applying the stationary medium assumption, the molar average term is removed from Equation 3-15. The one-dimensional solution of this equation, with the stationary medium approximation applied, is shown in Equation 3-22. For comparison, the corresponding solution without the stationary medium approximation is shown in Equation 3-23. Additionally, for a thin cathode a sufficient approximation for the one-dimensional pressure distribution can be made using the first terms from the series expansion of the exponential in Equation 3-23, as shown in Equation 3-24 [21]. It should be noted that Equations 3-22 and 3-24 differ only by the bracketed term. Thus the stationary medium approximation will under-predict the oxygen partial pressure when compared to the full solution, and is therefore considered a conservative estimate.

$$p_{O_2}(y) = p^0_{O_2} - \frac{i'' R_u T}{4FD_{O_2-N_2} p}\frac{\tau_{ca}}{\varepsilon_{ca}} y \tag{3-22}$$

$$p_{O_2}(y) = p - \left(p - p_{O_2}^0\right)\exp\left[\frac{i'' R_u T}{4FD_{O_2-N_2} p}\frac{\tau_{ca}}{\varepsilon_{ca}} y\right] \tag{3-23}$$

$$p_{O_2}(y) \approx p_{O_2}^0 - \left[\frac{p - p_{O_2}^0}{p}\right]\frac{i'' R_u T}{4FD_{O_2-N_2} p}\frac{\tau_{ca}}{\varepsilon_{ca}} y \tag{3-24}$$

3.1.1.3 The Depletion Current Density

Under SOFC operation at high current densities the diffusion of reactants to electroactive sites near the electrode-electrolyte interfaces can limit cell performance. This diffusion limitation is typically described through the cell concentration polarization and limiting current density, the latter of these corresponding to the total depletion of consumed reactants at reaction sites near the electrode-electrolyte interfaces. However, under the common one-dimensional approach it is not considered that depletion of reactants can occur along discrete segments of the electrode-electrolyte interface while other segments of the interface remain active. Furthermore, in diffusion limited scenarios it is possible for the depletion of reactants to lead to the degradation and deactivation of cell components. For example, in fuel depleted anode regions a lack of hydrogen combined with the electro-oxidative generation of oxygen can promote transformation of the Ni phase back into NiO [10]. Such a redox scenario could have deleterious effects on SOFC performance and reliability, specifically with respect to changes in anodic microstructures compromising interfacial integrity [89].

The potential flow models presented above allow for the description of highly localized reactant depletion phenomena within the bulk electrode. Given a conventional interconnect design (see Figure 3.1), the onset of reactant depletion at the electrode-electrolyte interface is expected to occur at the interconnect rib midpoint, Figure 3.3. A

depletion current density for the consumed reactant, i''_{dep}, can be defined by solving the reactant partial pressure distribution at this location in the electrode under the condition of zero concentration (i.e., $p_i^0(a,0)=0$) for the corresponding current density, shown in Equation 3-25 [6, 56].

$$i''_{dep} = \frac{zFD_{ij}}{R_u T}\frac{\varepsilon}{\tau}\frac{p_i^0}{t_{elec} + \sum_{n=1}^{\infty} C_n\left[\cosh\left(\lambda_n t_{elec}\right) - \cos n\pi\right]} \tag{3-25}$$

$$C_n = \frac{A_{n,elec}}{B_{0,elec}} = \frac{2\sin\left(\lambda_n b\right)}{n\pi\lambda_n \sinh\left(\lambda_n t_{elec}\right)}\left(\frac{a}{b}\right) \tag{3-26}$$

If the button-cell approximation is applied the constant C_n defined in Equation 3-26 reduces to zero. In this case, the depletion current density for the given electrode approaches the more commonly defined limiting current density, Equation 3-27. However, in actual SOFC operation the reactant depletion current density will be less than the expected limiting current density. This distinction is significant, since depleted operation may occur at current densities considered safe using a button-cell approach.

$$i''_{dep} = i''_{lim} = \frac{zFD_{ij}}{R_u T}\frac{\varepsilon}{\tau}\frac{p_i^0}{t_{elec}} \tag{3-27}$$

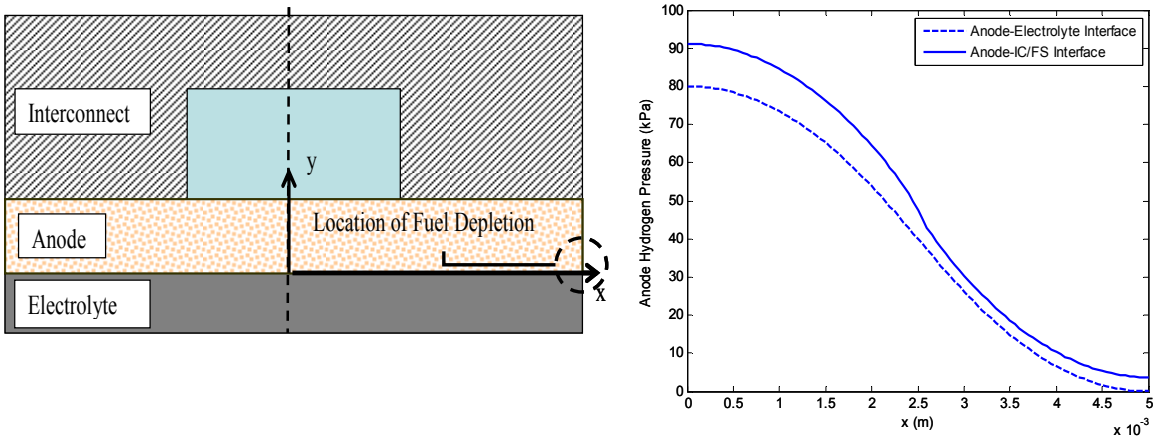

Figure 3.3 Multi-dimensional fuel depletion effects within the SOFC anode: similar oxygen depletion effects may be seen within the cathode as indicated above

3.1.1.4 Dimensionless Electrode Performance Metrics

Five basic dimensionless parameters can be used to analyze electrode performance. The first four are geometric parameters that are normalized by the unit cell half-width, a. This dimension is chosen as a characteristic dimension because discerning the impacts of the lateral electrode geometry is desired. These four parameters are the previously defined length fraction, the dimensionless coordinates (x^* and y^*), and the dimensionless thickness (t^*). Additionally, a dimensionless partial pressure is defined.

$$x^* = \frac{x}{a};\ y^* = \frac{y}{a};\ t^* = \frac{t_{elec}}{a};\ p_i^* = \frac{p_i}{p_i^0} \tag{3-28}$$

Based on the first four parameters the dimensionless partial pressure can be defined in a form comparable to the existing electrode partial pressure distributions. This expression is cast in the most general form with respect to the electrode type in Equation 3-29.

$$p_i^*\left(x^*, y^*\right) = 1 - \frac{a}{p_i^0} B_0\left(t^* - y^*\right) - 2\frac{a}{p_i^0} B_0 \sum_{n=1}^{\infty} \frac{\sin\left(n\pi LF\right)}{n^2\pi^2 \sinh\left(n\pi t^*\right)} \left(\frac{1}{LF}\right)\left[\cosh\left(n\pi t^*\right) - \cosh\left(n\pi y^*\right)\cos\left(n\pi x^*\right)\right] \tag{3-29}$$

$$B_0 = \frac{R_u T}{zFD_{ij}} \frac{\tau}{\varepsilon} i'' \tag{3-30}$$

This dimensionless pressure can be recast to find a correction factor for the pressure based on the button-cell approximation by multiplying Equation 3-29 by the gas stream partial pressure, p_i^0. Recognizing that the first two terms in Equation 3-31 compose the expression for the partial pressure based on the button-cell approximation the correction factor is easily recognized as the summation term on the right-hand side.

$$p_i\left(x^*, y^*\right) = p_i^0 - aB_0\left(t^* - y^*\right) - 2aB_0 \sum_{n=1}^{\infty} \frac{\sin\left(n\pi LF\right)}{n^2\pi^2 \sinh\left(n\pi t^*\right)} \left(\frac{1}{LF}\right)\left[\cosh\left(n\pi t^*\right) - \cosh\left(n\pi y^*\right)\cos\left(n\pi x^*\right)\right] \tag{3-31}$$

$$p_i\left(x^*, y^*\right) = p_{i,BC} - 2aB_0 \sum_{n=1}^{\infty} \frac{\sin\left(n\pi LF\right)}{n^2\pi^2 \sinh\left(n\pi t^*\right)} \left(\frac{1}{LF}\right)\left[\cosh\left(n\pi t^*\right) - \cosh\left(n\pi y^*\right)\cos\left(n\pi x^*\right)\right] \tag{3-32}$$

Based on the pressure in Equation 3-29 a dimensionless depletion current density can also be defined. A more detailed derivation is provided in Appendix B. This dimensionless form of the depletion current density compares the depletion current density to a limiting current density based on the unit cell half-width (see the denominator of the expression on the right-hand side in Equation 3-33a). Casting the

limiting current density in this form allows for representation of the upper limit of influence that the lateral electrode geometry exerts over reactant depletion. The dimensionless depletion current density defined in Equation 3-33 can be used to judge the influence of sheet resistance effects on reactant transport. These sheet resistance effects arise from increased transport path lengths associated with lateral diffusion across the unit cell cross-section. It is particularly important to note that this dimensionless current density is strictly a function of non-dimensional geometric factors, and thus serves as a general guide for continuum-level electrode design with respect to mass transfer, indicating in a general sense where reducing electrode thickness is no longer favorable for a given interconnect geometry.

$$i_{dep}^{*} = \frac{i_{dep}^{''}}{\frac{zFD_{ij}p_i^0}{R_u Ta}\frac{\varepsilon}{\tau}} \tag{3-33a}$$

$$i_{dep}^{*} = \frac{1}{t^{*} + \sum_{n=1}^{\infty} \frac{2\sin(n\pi LF)}{n^2\pi^2 \sinh(n\pi t^{*})}\left(\frac{1}{LF}\right)\left[\cosh(n\pi t^{*}) - \cos n\pi\right]} \tag{3-33b}$$

For the button-cell case, the dimensionless depletion current density reduces to a simple inverse dependence on t^{*}. Using basic relation i^{*}_{dep} can be normalized to gauge how much a particular electrode geometry will deviate from the depletion behavior predicted using a button-cell model.

$$i_{dep,BC}^{*} = \frac{1}{t^{*}} \tag{3-34}$$

$$\frac{i_{dep}^*}{i_{dep,BC}^*} = \frac{t^*}{t^* + \sum_{n=1}^{\infty} \frac{2\sin(n\pi LF)}{n^2\pi^2 \sinh(n\pi t^*)} \left(\frac{1}{LF}\right) \left[\cosh(n\pi t^*) - \cos n\pi\right]} \tag{3-35}$$

3.1.2 The Dusty-Gas Model

3.1.2.1 One-Dimensional Electrode Models

The potential flow models described above provide a simplified means of modeling diffusive phenomena within SOFC electrodes. However, these models only account for the interaction between the gases and the porous electrode through the use of an effective diffusion coefficient, i.e. the binary diffusion coefficient modified by the ratio of the electrode porosity and tortuosity. A means of further accounting for the gas-solid interaction within the porous electrode is through the use of the dusty-gas model, in which the solid matrix is abstracted as large immobile dust particles that impede the motion of the gas species [41].

The dusty-gas model is shown in its general form in Equation 3-36. Typically the final term on the right hand side is neglected in SOFC electrode models due to the assumption of negligible pressure gradients within the electrode. For the current work this assumption is retained. Neglecting pressure gradients has received attention lately as a potential source of error in SOFC models [57]. However, the influence of pressure gradients, particularly within the cross-sectional geometry shown in Figure 3.1, is not expected to be significant.

$$\frac{N_i}{D_{ik}^{eff}} + \sum_{j=1, j\neq i}^{n} \frac{y_j N_i - y_i N_j}{D_{ij}^{eff}} = -\frac{1}{RT}\left[p_{tot}\left(\vec{\nabla} \cdot y_i\right) + y_i \vec{\nabla} p_{tot}\left(1 + \frac{\kappa p_{tot}}{\mu D_{ik}^{eff}}\right)\right] \tag{3-36}$$

For the one-dimensional case, conservation of mass, inclusive of the dusty-gas flux model within the SOFC electrodes, reduces to a second order ordinary differential equation that can be subsequently reduced to a system of first order equations and solved numerically using a shooting method. Assuming a planar reaction zone, this approach relies on the application of a Faradaic molar flux boundary condition at the electrode-electrolyte interface to ensure that conservation of the reactant species is satisfied across the electrode. In later chapters this simplifying planar reaction zone assumption will be relaxed, and the impact of reaction zone microstructure will be addressed in greater detail. The second order ODEs for the anode and cathode are given in Equations 3-37 and 3-39, respectively.

$$\frac{d^2 y_1}{dx^2} + \frac{\alpha}{D_{12}^{eff}}\left[\frac{1-\alpha y_1}{D_{12}^{eff}} + \frac{1}{D_{1k}^{eff}}\right]^{-1}\left(\frac{dy_1}{dx}\right)^2 = 0 \tag{3-37}$$

$$\alpha = 1 - \sqrt{M_{H_2}/M_{H_2O}} \tag{3-38}$$

$$\frac{d^2 y_1}{dx^2} + \frac{1}{D_{12}^{eff}}\left[\frac{1-y_1}{D_{12}^{eff}} + \frac{1}{D_{1k}^{eff}}\right]^{-1}\left(\frac{dy_1}{dx}\right)^2 = 0 \tag{3-39}$$

The primary distinction between the anode and cathode side models is that the variable α will not be present in the cathode ODE, Equation 3-39. The absence of this value results from the fact that there is no molar flux of nitrogen within the cathode. Additionally, the binary system consists of oxygen and nitrogen, indicated by the subscripts 1 and 2, respectively.

The dusty-gas model equations were initially solved for a SOFC anode in a simplified one-dimensional sense following the work of Suwanwarangkul, et al. [36] in order to provide a benchmark for the potential flow models described above. The presently reported investigation utilized a Runge-Kutta method, implemented both directly and through the Matlab ode45 solver, to simulate and analyze binary (H_2-H_2O) and ternary (H_2-H_2O-Ar) mixtures. The latter of these mixtures allows for comparison of the one-dimensional DGM result to the modeling and experimental results presented in [36] and [90], respectively. For the ternary mixture, the ODE that is solved is shown in Equation 3-40. In all cases, separate scenarios of constant concentration (Dirichlet) and constant molar flux (Neumann) boundary conditions were applied at the electrode-gas stream interface. These molar flux boundary conditions are set based on the current density and Faraday's Law.

$$\frac{d^2 y_1}{dx^2} + \frac{\alpha}{D_{12}^{eff}}\left[\frac{1}{D_{1k}^{eff}} + \frac{1}{D_{1Ar}^{eff}} + \left(1 - y_{Ar}\right)\left(\frac{1}{D_{12}^{eff}} - \frac{1}{D_{1Ar}^{eff}}\right) - \frac{\alpha y_1}{D_{12}^{eff}}\right]^{-1}\left(\frac{dy_1}{dx}\right)^2 = 0 \quad (3\text{-}40)$$

3.1.2.2 Two-Dimensional Electrode Cross-Section Models

Two dimensional dusty-gas models were explored further for the binary mixture case within a finite element analysis (FEA) environment using COMSOL Multi-Physics. These DGM studies provide benchmark two-dimensional models for the anode and cathode potential flow models and their corresponding dimensionless parameters. This benchmarking process focuses on the comparison of predicted interfacial partial pressures, depletion current densities, and the corroboration of predictions from the

dimensionless parameters. Comparison of these models will be provided in the following chapter.

Due to increased interest in anode supported SOFC geometries the exploration of mass transport phenomena in SOFC electrodes often focuses on the study of anode transport phenomena [21, 36, 44, 54, 55]. Within the anode, the molar flux of hydrogen for a binary mixture, according to the dusty-gas model, is defined in Equation 3-41. A two dimensional finite element model for oxygen transport on the cathode side can also be produced based on the oxygen molar flux, Equation 3-42. As in the potential flow and one-dimensional DGM approaches, nitrogen is treated as a stagnant gas. Each of these flux expressions is applied as the operand in Equation (3-4), which is subsequently solved using the General PDE mode in COMSOL Multi-Physics.

$$N_{H_2} = -\frac{p}{R_u T}\left[\frac{1-\alpha y_{H_2}}{D^{eff}_{H_2-H_2O}} + \frac{1}{D^{eff}_{H_2k}}\right]^{-1} \vec{\nabla}\cdot y_{H_2} \tag{3-41}$$

$$N_{O_2} = -\frac{p}{R_u T}\left[\frac{1-y_{O_2}}{D^{eff}_{O_2-N_2}} + \frac{1}{D^{eff}_{O_2k}}\right]^{-1} \vec{\nabla}\cdot y_{O_2} \tag{3-42}$$

For the anode and cathode models two boundary condition cases are considered within the gas stream: Dirichlet (constant composition) and Neumann (constant molar flux). The first of these cases allows for additional comparison of the finite element models with the one-dimensional dusty-gas model solved using Runge-Kutta methods, which fix both composition and molar flux along the entire electrode-gas stream interface (effectively treating a boundary value problem with an initial value problem approach).

The latter case follows the potential flow models above, which use a Neumann boundary condition along the electrode-gas stream interface. Implementation of the DGM within the General PDE mode allows for the application of constraint equations on particular points. These constraint equations allow for setting the flux within the gas channel and constraining the composition at the channel centerline. A similar approach is taken in completing the solution of potential flow models, where the partial pressure was constrained to set a constant within the general solution.

Both boundary conditions were used to examine convergence behavior for meshes applied to the computational domain shown in Figure 3.2. For the anode models, a 36x36 grid was found to be sufficient for two geometry cases with thicknesses of 750 μm and 2000 μm. While the second of these geometries has a significantly larger thickness than its width, the elements in a square grid still maintain a reasonable aspect ratio of 4:1. In general the cathode models require a finer mesh than the anode models. Initial investigations focused on a cathode geometry of 50 μm. At around 50 element divisions along the cathode width convergence was achieved for this case. Two additional cathode thicknesses were examined: 100 μm and 250 μm. An element aspect ratio of 2.5:1 was maintained for the cathode models with 50 μm thickness. For the thicker cathode geometries meshes of 20x100 and 50x100 were used, each with a 1:1 aspect ratio for the elements.

In the next chapter performance predictions based on dimensionless performance metrics are compared to numerical predictions of partial pressure and depletion current density based on a finite element solution of the dusty-gas model within SOFC electrodes. It will be shown that the pressure correction factor developed provides a

reasonable prediction of interconnect geometry effects. Thus, it is presented as a modeling tool that can be applied to translate component level fidelity to cell and stack level models. The depletion current density metrics developed are used to present basic design maps for SOFC unit cell cross-sections. These dimensionless forms of the depletion current density quantify the influence of sheet resistance effects on reactant depletion and can predict the deviation from the limiting current behavior predicted using a button-cell model.

3.2 Summary

Performance metrics for the design of SOFC unit cell cross-section have been developed using existing potential flow models for SOFC mass transport. These metrics include a pressure correction factor that can be used to modify button-cell predictions and dimensionless forms of the reactant depletion current density. Numerical benchmark models for mass transport based on the dusty-gas formalism are also presented for one- and two-dimensional cases. In the following chapter, the analytical models and their associated performance metrics will be compared to these benchmark models, culminating in the presentation of design maps for SOFC cross-sectional geometry that are based on the dimensionless reactant depletion current density.

CHAPTER 4

CONTINUUM COMPONENT LEVEL MODELS: RESULTS AND ANALYSIS

The performance metrics developed in the previous chapter provide valuable tools for SOFC cross-sectional design. This point is demonstrated in the present chapter through the comparison of the analytical models to benchmark numerical models. The analytical performance metrics are shown to close the gap in performance predictions made by the potential flow models and the more rigorous dusty-gas model. Additionally, presented in the form of design maps these dimensionless metrics provide a concise means of predicting electrode performance for planar SOFCs.

4.1 Potential Flow Models: Initial Results

4.1.1 Mass Transport Models

The potential flow models for mass transport were initially examined for a binary hydrogen and steam mixture for a SOFC with unit cell width of 1.0 mm and an anode thickness of 750 μm. A current density of 1.0 A/cm^2 was applied at a cell temperature of 800 °C (1073 K). A mixture of 90% hydrogen and 10% steam at atmospheric pressure was used to model the fuel stream. An anodic porosity of 30% was assumed, and a tortuosity of 14.5 was set based on existing literature [21]. While this value is higher than geometric anode tortuosities measured experimentally (typically 2-10), it is estimated directly from experimental SOFC button-cell performance. It has been suggested that estimation of such heightened tortuosities may be mitigated by accounting

for separate diffusion resistances within the bulk anode and the chemically active regions near the anode-electrolyte interface [22], by factoring in Knudsen diffusion within the anode [21], or by considering surface diffusion effects at the anode-electrolyte interface [58]. These effects are not considered in the initial results presented based on the potential flow models. However, models used in later chapters attempt to incorporate some of these transport effects. In the initial results presented below the higher tortuosity value is employed as an effective tortuosity for SOFC operation unless otherwise noted.

The hydrogen and steam partial pressure distributions for the button-cell and actual interconnect geometry cases are compared in Figure 4.1 and 4.2. In these figures the solid and dashed lines indicate the pressure distribution along the electrode-interconnect/gas stream interface and the electrode-electrolyte interface, respectively. The influence of interconnect geometry is readily discernible. The hydrogen partial pressure at the anode-electrolyte interface is reduced when accounting for interconnect geometry. Correspondingly, the steam partial pressure at the anode-electrolyte interface shows a subsequent increase. Checks of the partial pressure distributions within the anode, as shown in Figures 4.1 and 4.2, reveal that the sum of the hydrogen and steam partial pressures throughout the anode adds to atmospheric (i.e., the total) pressure. This condition was also found to be true for the other geometries analyzed, as would be expected for the assumption of a negligible pressure gradient within the electrode. While the reactant partial pressure values are impacted by the interconnect geometry, the reactant distribution at the electrode-electrolyte interface remains relatively uniform. As will be discussed in later sections, this relative uniformity can be traced to the sizing of the electrode width and thickness for the geometry examined.

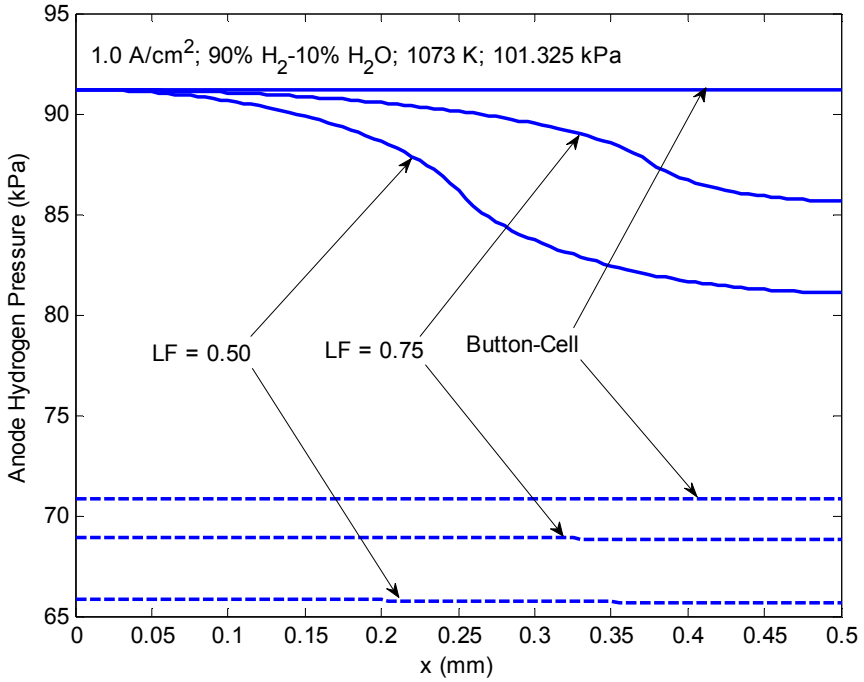

Figure 4.1 Anodic hydrogen partial pressures for button-cell and actual cell geometries at the fuel stream/interconnect (—) and electrolyte (- -) interfaces; shown for a unit cell cross-section similar to those shown in Figure 3.1

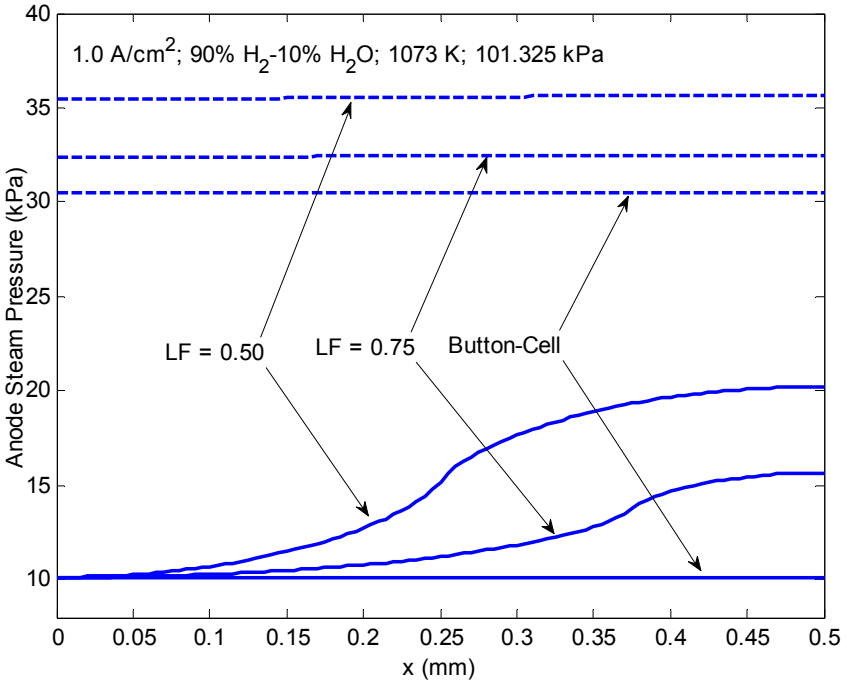

Figure 4.2 Anodic steam partial pressures for button-cell and actual cell geometries at the fuel stream/interconnect (—) and electrolyte (- -) interfaces; shown for a unit cell cross-section similar to those shown in Figure 3.1

Applying the model developed for the oxygen pressure distribution results in more drastic geometry effects, as shown in Figure 4.3. Again, the solid and dashed lines indicate the electrode-interconnect/gas stream interface and the electrode-electrolyte interface. As with the anode pressure distributions, a unit cell width of 1.0 mm and a current density of 1.0 A/cm^2 were used. A cathode thickness of 50 μm was used to reflect an anode-supported arrangement. Under the presumed one-dimensional transport of the button-cell case the pressure drop is relatively small compared to the anode, less than 1 kPa. However, a significant pressure drop along the width of the unit cell becomes evident when interconnect geometry is considered. Furthermore, at the edges farthest from the oxidant stream the cathode approaches oxygen depletion. In fact, for the cathode, results for $LF = 0.50$ are not shown since this geometry was found to experience depletion along a significant portion of the cathode-electrolyte interface. Under presumed 1-D transport an anode-supported cell can be considered to be chiefly limited by the anode geometry, but for actual anode-supported SOFCs with conventional interconnects, the thinner cathode could in fact limit performance. This is associated with the increased in-plane (or "sheet") resistance effects. Performance limiting effects arising from mass transfer within the cathode have been demonstrated in numerical models of electrolyte supported cells [33].

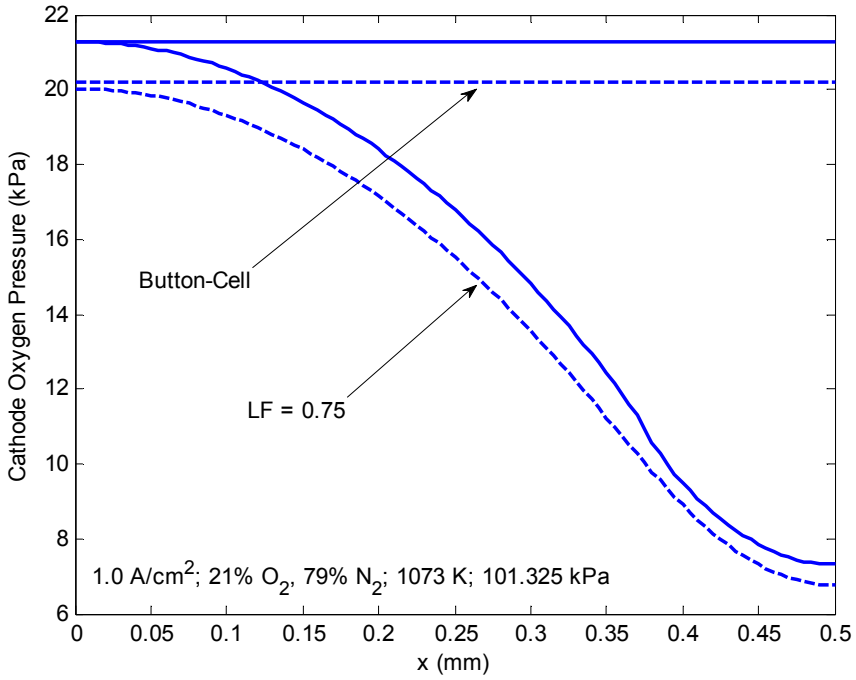

Figure 4.3 Oxygen partial pressures for button-cell and actual cell geometries at the air stream/interconnect (—) and electrolyte (- -) interfaces; shown for a unit cell cross-section similar to those shown in Figure 3.1

The significance of the geometry effects shown in Figures 4.1 through 4.3 demonstrate the need to account for interconnect geometry within SOFC models, particularly for thin electrodes. Details of these geometry effects have been addressed for specific electrode geometries in previous work [6, 39, 56]. Figures 4.1 through 4.3, however, also reveal some general behavior of porous SOFC electrodes at the continuum level. Overall, it can be seen that a decrease in length fraction results in an increase in mass transport resistance within an electrode of fixed thickness and width, as indicated by the decrease in interfacial pressures for the consumed reactants (Figures 4.1 and 4.3). Furthermore, a thin electrode can exacerbate lateral partial pressure variations. The increased sensitivity of thinner electrode can be attributed to the heightened impact of this in-plane, or "sheet," resistance despite the smaller transverse resistances of thin

electrodes. Finally, in previous work mass transport resistance and in-plane resistance effects were shown to be more pronounced for anodes with larger unit cell widths [6, 39, 56]. In later sections these general trends will be further quantified using the dimensionless groups developed in the previous chapter.

4.1.2 Depletion Current Density

As previously noted, depletion current density and its performance effects are commonly considered on the anode side for button-cell geometries and thus reduce to the limiting current density. To explore the effects of geometry on this critical parameter, initial studies of depletion phenomena focused on fuel depletion in the anode [6, 56]. Some key results of the studies are provided in Figure 4.4. The two cases shown are for a unit cell width of 1.0 mm, and both rely on a higher effective tortuosity value of 14.5 to produce estimates in the range of experimentally observed limiting currents [20, 21]. Under the button-cell approximation, the fuel depletion current density corresponds to the established definition of limiting current density, and is predicted to increase significantly as the anode becomes thinner. However, when interconnect geometry is accounted for (as shown for a length fraction of 0.50) the fuel depletion current density decreases after the thickness decreases below 500 μm for the case shown. The change in behavior of fuel depletion current density as a function of anode thickness (in the case with LF = 0.50) can be attributed to the dominance of sheet resistance effects within the total anodic resistance to mass transfer. This concept was demonstrated above for the cathode oxygen partial pressure investigation. For excessively thin electrodes, the predominance of sheet resistance effects hindering mass transfer can become a performance issue and leads to

significant variation from predictions based on button-cell models, as will be demonstrated.

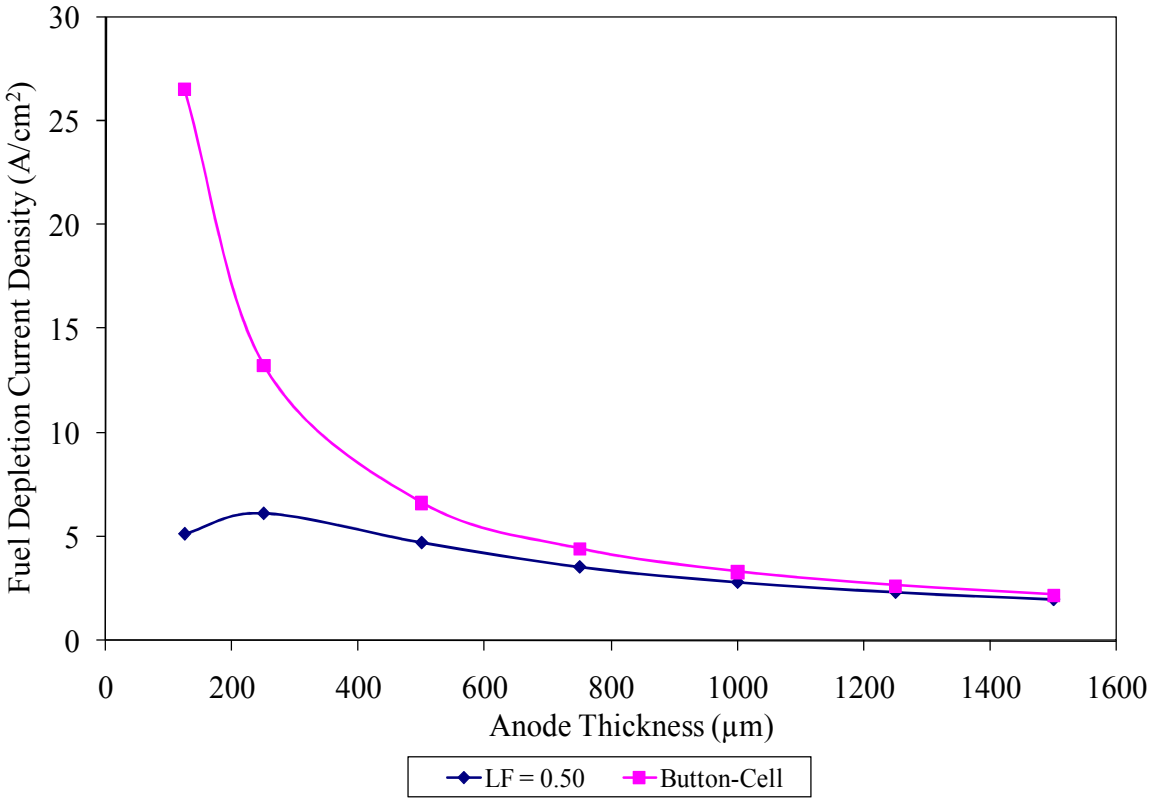

Figure 4.4 Effects of interconnect geometry on fuel depletion current density

The role of anode geometry in fuel depletion phenomena has been further investigated in parametric studies based on a central composite experimental design [6, 56]. Representative values of the fuel depletion current density computed for a range of fuel stream compositions are given in Table 4.1 for the unit cell geometries analyzed in these studies. All values shown are calculated for an anode thickness of 750 µm. The advantage of smaller unit cell geometries is apparent. For example, at all concentrations shown a SOFC with a unit cell width of 1.0 mm can achieve fuel depletion current

densities approximately three times greater than those achieved by a SOFC with a unit cell width of 5.0 mm. The same 1.0 mm unit cell SOFC can achieve fuel depletion current densities almost ten times greater than those achieved with a SOFC with a 10 mm unit cell. Furthermore, for the smallest geometry the onset of fuel depletion can occur at a current density near the traditionally defined limiting current density. As demonstrated in Figure 4.5a, the onset of fuel depletion in geometries with smaller unit cell widths corresponds to what is almost the complete absence of hydrogen at the anode-electrolyte interface. This scenario stands in sharp contrast to that of the larger 10 mm unit cell geometry shown in Figure 4.5b. In the latter case the unit cell width serves as the greatest distance for hydrogen diffusion and results in a significant pressure drop in the lateral direction and a relatively low pressure drop between points across the anode thickness. Thus, for a given fuel stream composition and current density demand, a larger unit cell may exhibit a lower average pressure drop between the fuel stream and anode-electrolyte interface. However, these larger geometries may be noticeably more susceptible to fuel depletion at the anode-electrolyte interface and may exhibit significant disagreement between the depletion current density and the limiting current density predicted from a button-cell approach.

Table 4.1 Fuel depletion current density over a range of fuel stream (FS) compositions

FS Hydrogen Composition	SOFC Fuel Depletion Current Density (A/cm^2)		
	1.0 mm	5.0 mm	10 mm
5%	0.20	0.06	0.02
10%	0.40	0.13	0.04
50%	1.98	0.63	0.20
90%	3.57	1.13	0.36
95%	3.77	1.20	0.38

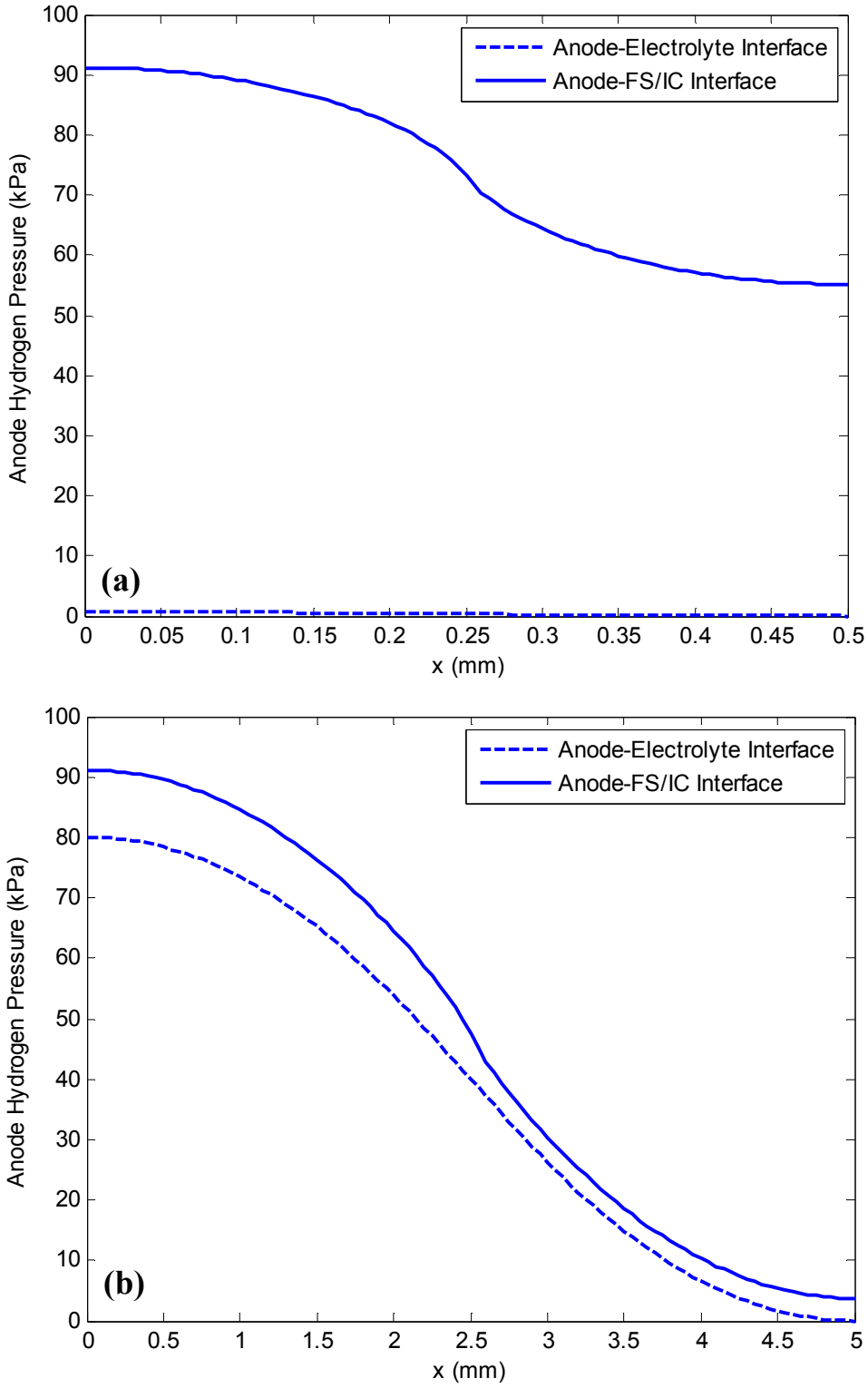

Figure 4.5 Hydrogen partial pressure distributions at the fuel depletion current density for unit cells of (a) 1.0 mm width and (b) 10 mm width (90% fuel stream hydrogen)

4.2 Dusty-Gas Model: Initial Results

4.2.1 One-Dimensional Anode Model

The application of the dusty-gas model was initially explored for the one-dimensional case on the anode side, since the anode is often the subject of continuum-level mass transport modeling within SOFCs [21, 36, 44, 54, 55]. In addition to serving as a baseline comparison to the two-dimensional problems outlined in the previous chapter and discussed below, the 1-D anode model allows for testing the strength of the proposed button-cell pressure correction factor. Two cases were examined for this model: a binary H_2-H_2O mixture and a ternary H_2-H_2O-Ar mixture. The application of a ternary mixture follows modeling and experimental results in the literature, with the ratio of H_2:H_2O constrained at 4:1 [36, 90]. Representative hydrogen partial pressure distributions through the anode thickness are shown in Figure 4.6 for a 50% H_2 mixture. This concentration is chosen to distinguish between the binary and ternary models. As expected, the addition of the argon diluent impedes diffusion of hydrogen and further lowers the interfacial partial pressure.

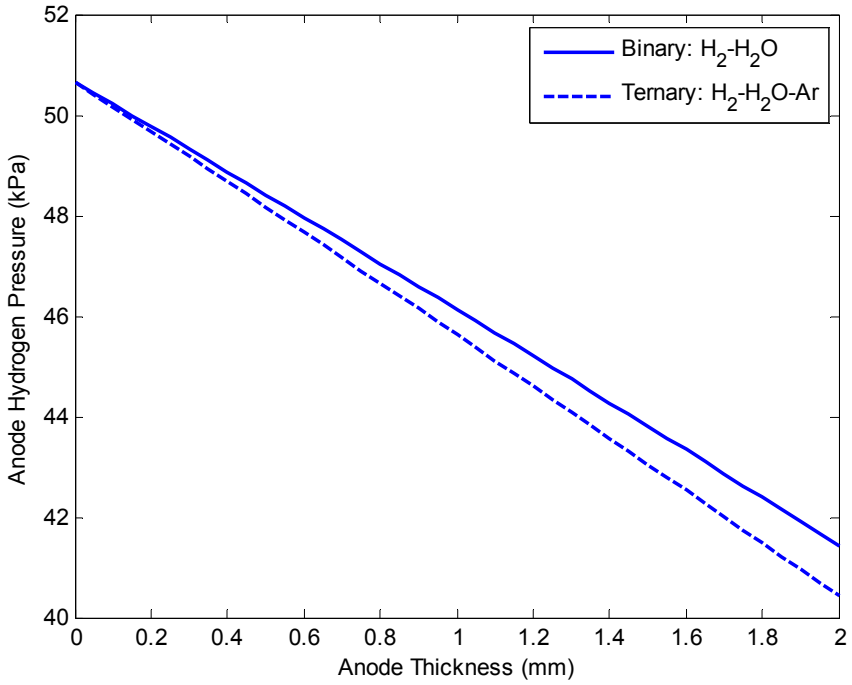

Figure 4.6 Anodic hydrogen partial pressures for 1-D dusty-gas model for a binary H_2-H_2O mixture (—) and a ternary H_2-H_2O-Ar mixture (- -) (50% H_2 and 12.5% H_2O at 1.0 A/cm^2)

To further corroborate the one-dimensional numerical solution approach, the results for the ternary dusty-gas model are compared with published modeling results [36] and experimental data [90] in Figure 4.7. For most operating scenarios the model results agree with the experimental data. However, as conditions that are more likely to result in fuel depletion phenomena are approached the model and experimental results increasingly diverge, as can be seen for the cases of a current density of 1.0 A/cm^2. Thus it is possible that for more accurate predictions of limiting and fuel depletion current densities the dusty-gas model will also require the use of an effective tortuosity. This point is further illustrated in later sections where limiting and fuel depletion current density predictions are compared for the potential flow and DGM models. Additionally, the one-dimensional DGM results shown in Figures 4.6 and 4.7 assume a planar reaction

zone subject to a uniform molar flux based on the current density demand. The need to apply an effective tortuosity to improve the accuracy of concentration polarization and depletion current density predictions using this simplified boundary condition could be reduced through a more detailed treatment on the reaction zone within the electrode. A means of incorporating reaction zone details will be addressed in later chapters.

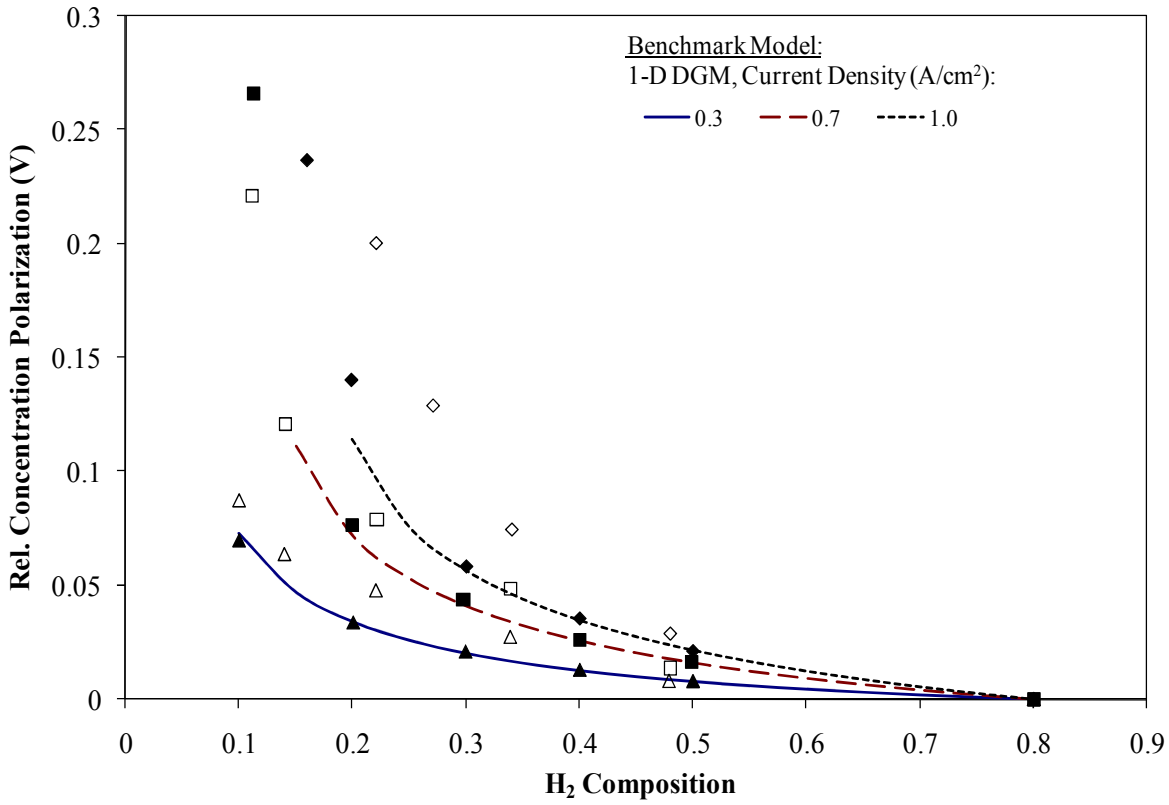

Figure 4.7 Dusty-gas model predictions of concentration polarization relative to 80% H_2 in fuel stream: model results from Suwanwarangkul et al. (♦ 1.0 A/cm^2, ■ 0.7 A/cm^2, ▲ 0.3 A/cm^2) [36] and experimental data from Yakabe et al. (◊ 1.0 A/cm^2, □ 0.7 A/cm^2, Δ 0.3 A/cm^2) [90]

4.2.2 Two-Dimensional Binary Models

Finite element solutions of the dusty-gas model have been explored for two anode geometries. The first geometry corresponds to the geometry studied using the potential

flow models. The second geometry corresponds to the anode geometry outlined in the one-dimensional DGM studies and was examined to provide a comparison to the modeling and experimental results shown above. Use of these two geometries will also provide for comparison to performance predictions made with the dimensionless metrics from the previous chapter. Representative results of these models are shown in Figures 4.8 and 4.9 for hydrogen fuel stream compositions of 90% and 80%, respectively. The 80% hydrogen composition applied in the case shown in Figure 4.9 corresponds to the base case applied in the published experimental and modeling work above. In both cases, the incorporation of geometry effects is evident and comparing the finite element results with the one-dimensional numerical predictions shows a lower interfacial hydrogen partial pressure for the two-dimensional case. For the results in Figure 4.8 this difference can be seen directly. For the results following the work of Suwanwarangkul et al. [36] and Yakabe et al. [90] the Runge-Kutta solution of the 1-D DGM predicts a minimum hydrogen partial pressure of ~74.1 kPa in the base case. As demonstrated in the potential flow results, geometry effects are evident when describing electrode mass transport using the more rigorous dusty-gas formalism as well. While at the concentrations and current densities shown the deviations between each approach are at most ~4% (for the 1-D DGM and potential flow cases in Figure 4.8), significant variation between model predictions can arise, particularly in diffusion limited scenarios. Developing a means of accounting for geometry effects and establishing when significant variations will occur is warranted and will be discussed in further detailed in later sections.

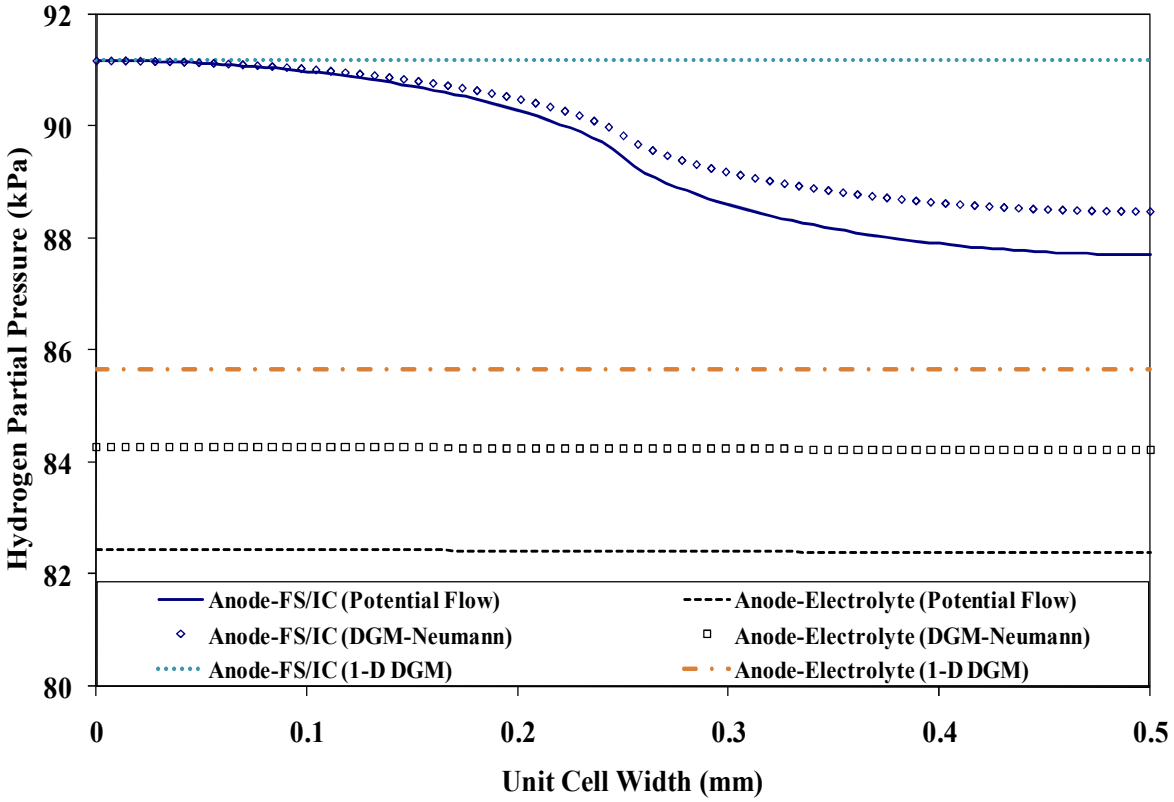

Figure 4.8 Dusty-gas model and potential flow hydrogen partial pressure distributions for an anode with thickness 750 μm and 1 mm unit cell width (1.0 A/cm^2, 90% H_2, $\varepsilon = 0.3$ and $\tau = 5$)

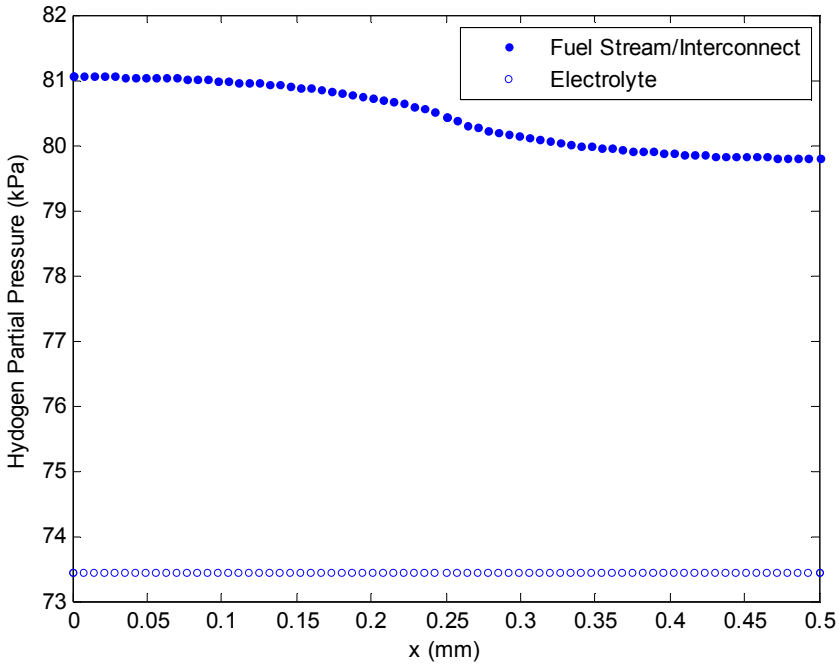

Figure 4.9 DGM prediction of the hydrogen partial pressure distribution for an anode with thickness 2 mm and 1 mm unit cell width (1.0 A/cm^2, 80% H_2, $\varepsilon = 0.46$ and $\tau = 4.5$)

In addition to the models of anodic mass transport, oxygen transport within the cathode has been characterized using a two-dimensional finite element solution of the dusty-gas model, with initial results displayed in Figure 4.10. As shown with the potential flow cathode model, a significant variation in oxygen partial pressure is seen across the cathode in the lateral direction. In fact, for a low current density of 0.5 A/cm^2 the geometry analyzed approaches oxygen depleted operation. This finding underscores the issue that for actual anode-supported SOFCs with conventional interconnects the thinner cathode could in fact limit performance. Furthermore, it can be shown through the dimensionless performance metrics presented in later sections that such thin cathodes may not be an optimal geometry for mass transport performance when paired with typical SOFC interconnect designs.

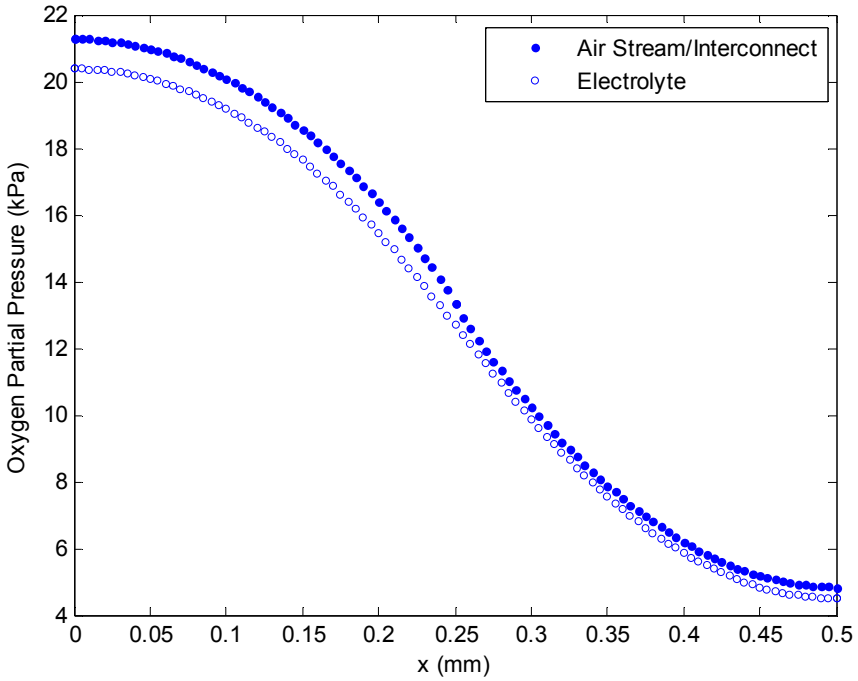

Figure 4.10 DGM prediction of the oxygen partial pressure distribution for a cathode with thickness 50 μm and 1 mm unit cell width (0.5 A/cm^2, 21% O_2, $\varepsilon = 0.3$ and $\tau = 5$)

4.3 Model Comparisons

4.3.1 One-Dimensional Model Comparisons

Key discrepancies in the one-dimensional anode models (potential flow and DGM) occur in the prediction of interfacial partial pressures and limiting current densities. One such discrepancy is shown for limiting current predictions produced by the potential flow and dusty-gas models in Figure 4.11 for the nominal anode geometry with porosity of 0.3 and tortuosity of 5. This unmodified tortuosity is used based on the common range of geometric anode tortuosities noted above. An elevated effective tortuosity is not applied because it may inaccurately account for the influence of phenomena that are neglected in the present model [22, 58]. Variations in interfacial partial pressure predictions will be discussed in the comparison of the two-dimensional models. Limiting current densities predicted using the potential flow models are generally higher than those produced using the DGM, but the error between the two (treating the DGM results as the true value) decreases as hydrogen composition increases. While the agreement in the models is better, in a relative sense, at higher compositions, both approaches overpredict the limiting current density when compared to published experimental values [20, 21]. For reference, a potential flow estimate based on an elevated effective tortuosity is also shown in Figure 4.11. As for the initial fuel depletion current density results, both models would require application of a higher effective tortuosity to produce more reasonable estimates.

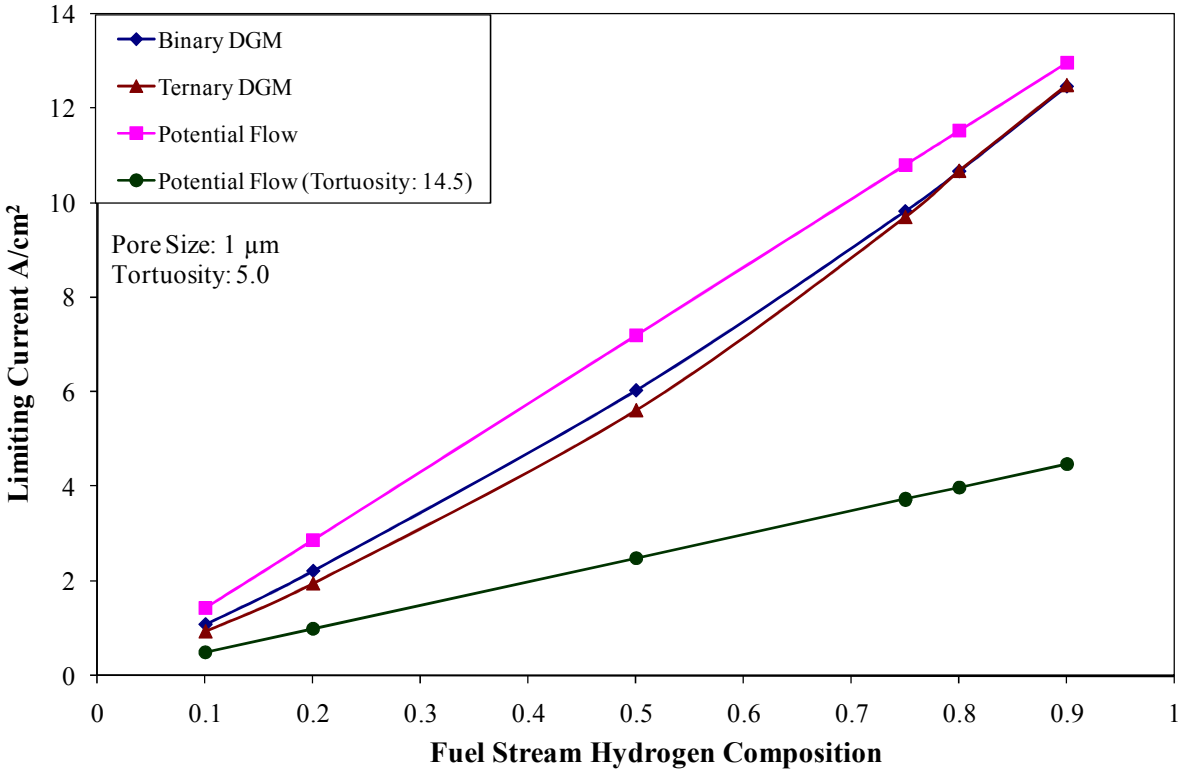

Figure 4.11 Fuel depletion current density predicted by the one-dimensional DGM and potential flow models for a 750 µm thick anode, $\varepsilon = 0.3$ and $\tau = 5$

Within the cathode, oxygen transport was examined in the one-dimensional case for three models: one applying the stationary medium approximation and two based on solution of the convection-diffusion equation [21]. Differences between the solutions produced with these three models are outlined in the previous chapter. The most important difference is that application of the stationary medium approximation produces a conservatively lower estimate of oxygen partial pressure. For example, for a 50 µm thick cathode ($\varepsilon = 0.3$ and $\tau = 5$) operating at 1.0 A/cm^2, the stationary medium solution predicts an interfacial partial pressure that is ~1% lower. The magnitude of this error increases with current density.

4.3.2 Two-Dimensional Model Comparisons

A representative prediction of the hydrogen partial pressure distribution produced from the finite element solution of the DGM is compared to the potential flow model in Figure 4.8. The discrete points represent the FEA solution, and the solid and dashed lines represent the analytical solution. The trend seen here, at the higher concentration, is comparable to that seen in previous comparisons of the one-dimensional case. Specifically, the potential flow model produces a conservative, lower estimate of interfacial partial pressure. The minimum hydrogen partial pressure predictions at the anode-electrolyte interface are summarized in Table 4.2 to further illustrate this point. The highest of these predictions is associated with the application of a Dirichlet boundary condition at the anode-fuel stream interface. For reference, the 1-D DGM estimates a minimum H_2 partial pressure of 85.66 kPa. Both of the constant flux (Neumann) boundary conditions produce lower estimates. For the DGM, this will remain true for all fuel stream compositions. However, the potential flow model does not always produce a conservative estimate of interfacial partial pressure. Obtaining a conservative (lower) partial pressure estimate from the potential flow models is dependent on mixture composition and its influence on the diffusion coefficients associated with the DGM and potential flow models.

Table 4.2 Minimum interfacial p_{H2} predictions for dusty-gas and potential flow models

Approach/Gas Stream B.C.	p_{H2} **(kPa)**
Potential Flow/Neumann	82.39
Dusty-gas/Neumann	84.23
Dusty-gas/Dirichlet	84.82

Comparisons of interfacial hydrogen partial pressure and fuel depletion current densities from anode models for the potential flow and dusty-gas model (DGM) results are shown in Figures 4.12 and 4.13. For the DGM two boundary condition cases are considered within the fuel stream: Dirichlet (constant composition) and Neumann (constant hydrogen flux). The potential flow models use a Neumann boundary condition within the fuel stream. The cases shown are for SOFC operation at 1073 K and 1 atm. Due to the geometry effects outlined above and in previous work [6, 39, 56], the two-dimensional models predict lower minimum partial pressures near the anode-electrolyte interface when compared to the button-cell prediction. Additionally, the fuel depletion current densities predicted by each case show a distinct reduction compared to the results shown in Figure 4.11.

For the predictions of interfacial partial pressure there is a shift between the models with respect to which model predicts a lower value. At lower compositions, the DGM predicts lower interfacial partial pressures with a shift between the models occurring around 50% composition. This shift occurs for the one-dimensional models as well. The cause of this shift can be seen through examination of the diffusion coefficients. For the potential flow models the diffusion coefficient is predicted as a function of temperature using the Chapmann-Enskogg model. Only the binary diffusion coefficient is used and Knudsen diffusion is not included. For the DGM the diffusion coefficient is a function of composition as well as temperature, and Knudsen diffusion is included. This difference in coefficients can be seen by comparing the molar flux, N_i, for the potential flow and DGM, as applied to a SOFC electrode. These molar flux terms are defined in Equations 3-1 and 3-2 in the previous chapter. As the mixture moves toward higher hydrogen

content Knudsen diffusion of this light species becomes dominant due to the dependence on composition in the DGM coefficient. This causes the effective diffusion coefficient to become higher than the binary diffusion coefficient; thus the lower hydrogen partial pressure prediction for the potential flow case is inaccurate.

A similar shift is seen for fuel depletion current density predictions from the two-dimensional DGM using a Dirichlet boundary condition, which produces a higher driving potential for mass transport along the electrode-fuel stream interface. This shift is not seen for the DGM cases where a Neumann boundary condition is applied, and it is absent in the one-dimensional cases where both the DGM and potential flow models effectively apply a Dirichlet boundary condition. However, as hydrogen concentration increases the potential flow and DGM predictions do appear to converge. The absence of a shift between the fuel depletion current density predictions for these similar cases is likely due to the fact that near limiting current the average composition in the electrode may still result in a lower effective diffusion coefficient.

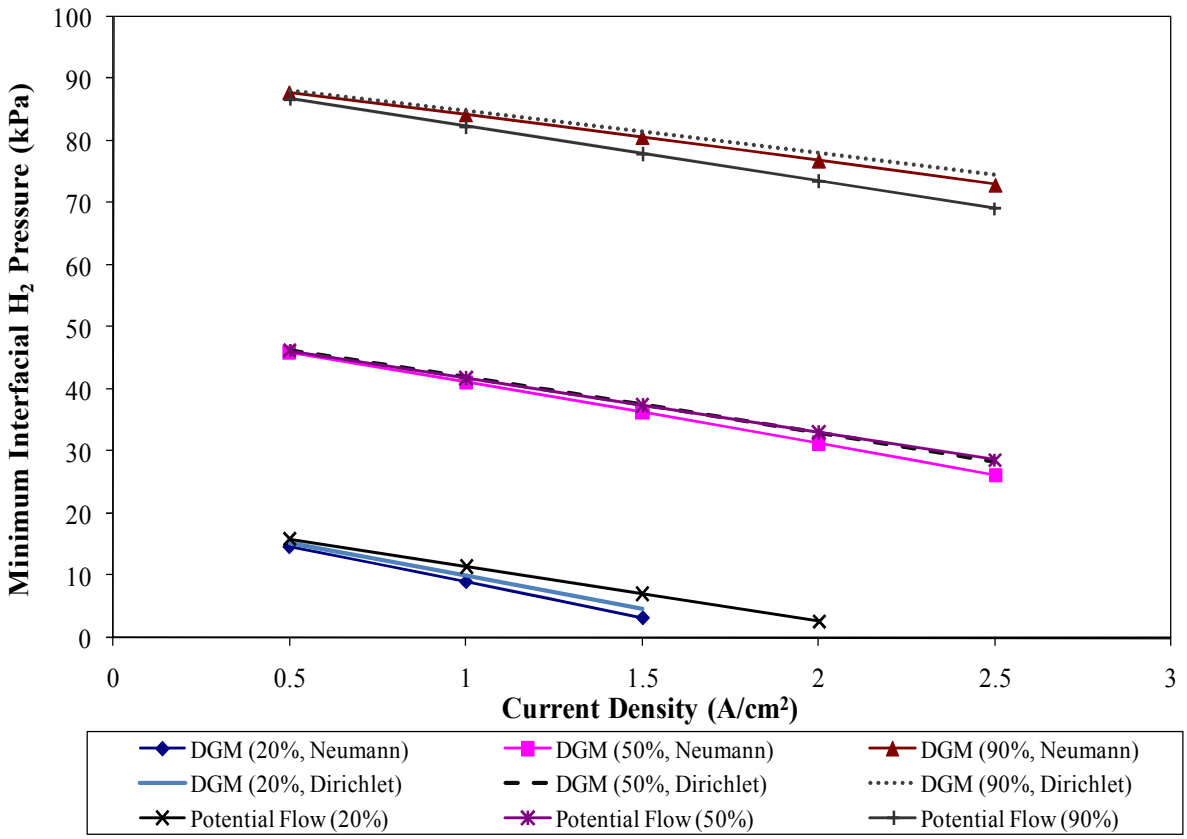

Figure 4.12 Minimum interfacial pressures predicted by the two-dimensional DGM and potential flow models for a 750 μm thick anode, $\varepsilon = 0.30$ and $\tau = 5.0$; percentages shown are for hydrogen in a binary H_2-H_2O mixture

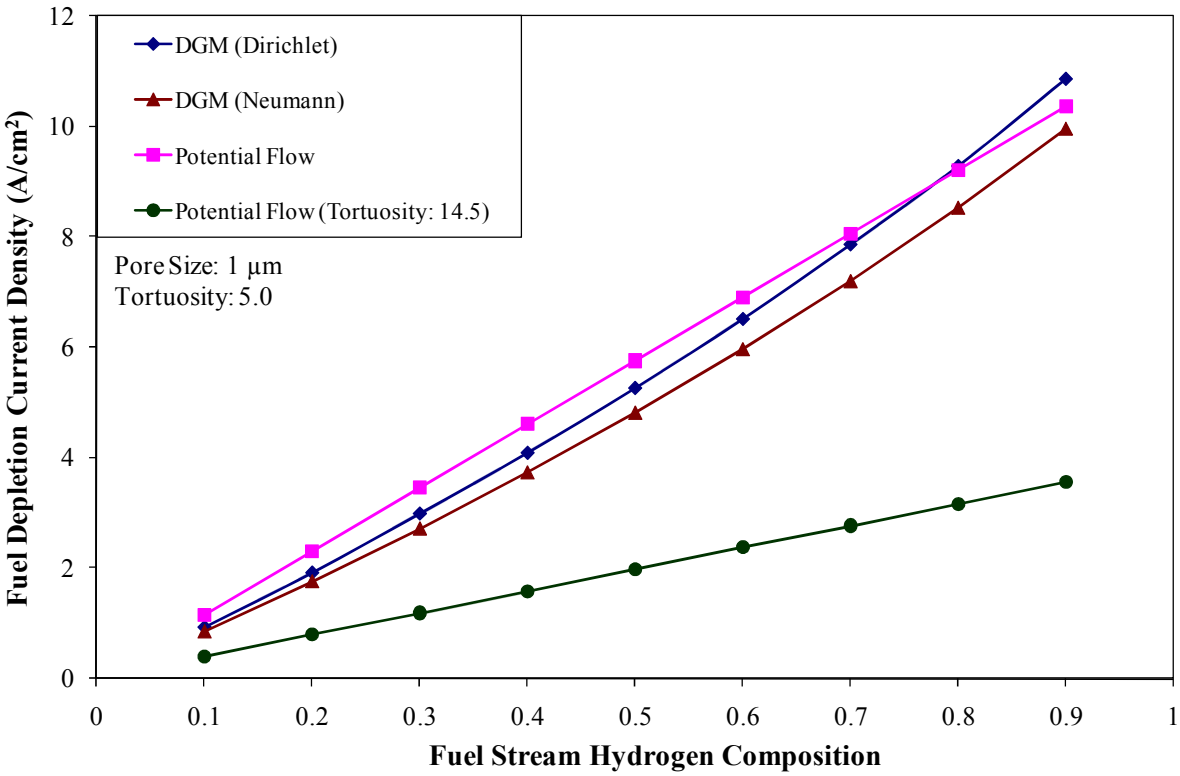

Figure 4.13 Fuel depletion current density predicted by the two-dimensional DGM and potential flow models for a 750 µm thick anode, $\varepsilon = 0.3$ and $\tau = 5$; for a binary H_2-H_2O mixture

For the cathode model a fixed oxygen concentration was used, assuming air was the oxidant. Three cathode thicknesses (50, 100, and 250 µm) with a unit cell width of 1 mm were modeled using the previously described finite element approach. Minimum partial pressure predictions for these cathode thicknesses are shown in Figure 4.14 for the potential flow model and DGM with a Neumann boundary condition applied at the cathode-air stream interface. The potential flow models also rely on this Neumann boundary condition. Applying a Dirichlet boundary condition at the cathode-air stream interface results in DGM predictions comparable, yet slightly higher, than those produced with the potential flow models. To preserve clarity on the plot the Dirichlet boundary condition cases are not displayed. The dusty-gas model with a Neumann boundary

condition applied at the cathode-air stream interface predicts a lower interfacial partial pressure in all of the cases examined. This lower prediction is comparable to the behavior seen on the anode side where, due to composition effects, the overall diffusion coefficient is reduced when accounting for Knudsen diffusion within the porous electrode. Thus, for air as an oxidant the dusty-gas model is preferred for predicting continuum partial pressure distributions within the bulk cathode. Application of the DGM is preferred in such cases because it would prevent overpredicting cathode mass transport performance. Also demonstrated in Figure 4.14 is the fact that the thickest cathode geometry among the three cases shows the best performance as indicated by the range of non-depleted current densities achieved.

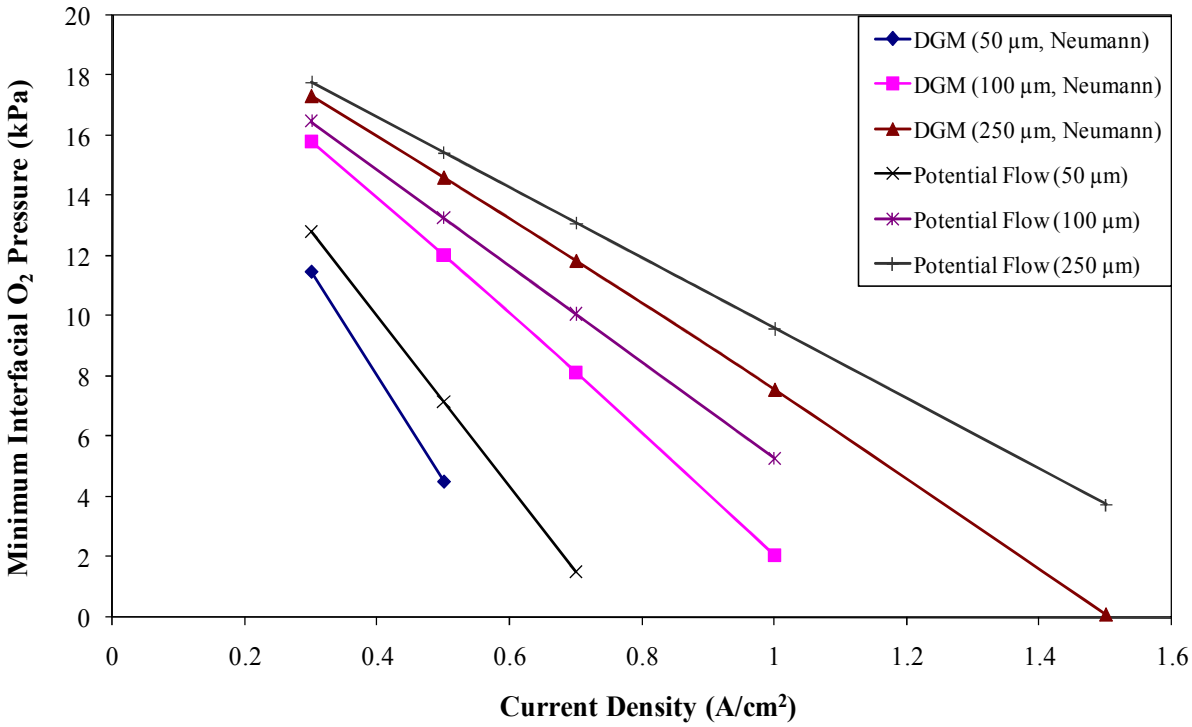

Figure 4.14 Minimum interfacial pressures predicted by the two-dimensional DGM and potential flow models for several cathode thicknesses, $\varepsilon = 0.30$ and $\tau = 5.0$

4.4 Dimensionless Performance Metrics for SOFC Electrodes

4.4.1 Mass Transport Performance Metrics

The performance metrics for SOFC electrodes developed in the previous chapter include a correction factor that can be applied to button-cell predictions of pressure distribution and two forms of dimensionless reactant depletion current density. The first of these metrics provides a means of incorporating interconnect geometry effects into higher level models without incurring an excessive computational burden. As a demonstration of this capability interfacial partial pressure predictions from the DGM finite-element model are compared to predictions produced with a corrected Runge-Kutta solution for the one-dimensional DGM in Figure 4.15. One-dimensional predictions for the binary mixture were corrected to account for interconnect geometry using Equation 3-32. In these calculations, Knudsen diffusion is accounted for using the Bosanquet formula, Equation 4.1.

$$\frac{1}{D_i^{eff}} = \frac{1}{D_{ij}^{eff}} + \frac{1}{D_{ik}^{eff}} \tag{4-1}$$

There is clear agreement between the corrected one-dimensional value and the two-dimensional finite element solution. For the corrected pressures this agreement is aided by accounting for Knudsen diffusion in the diffusion coefficient. The error seen in these predictions is largest at low concentration and higher current density. It is also particularly sensitive to the definition of diffusion coefficient applied in the correction factor calculation. If the binary diffusion coefficient is used the average error is 3.37%,

but the maximum error is ~27% at 20% fuel stream hydrogen and 1.5 A/cm^2. Adding Knudsen effects reduces the average error to 1.74% and the maximum error to ~3.2%.

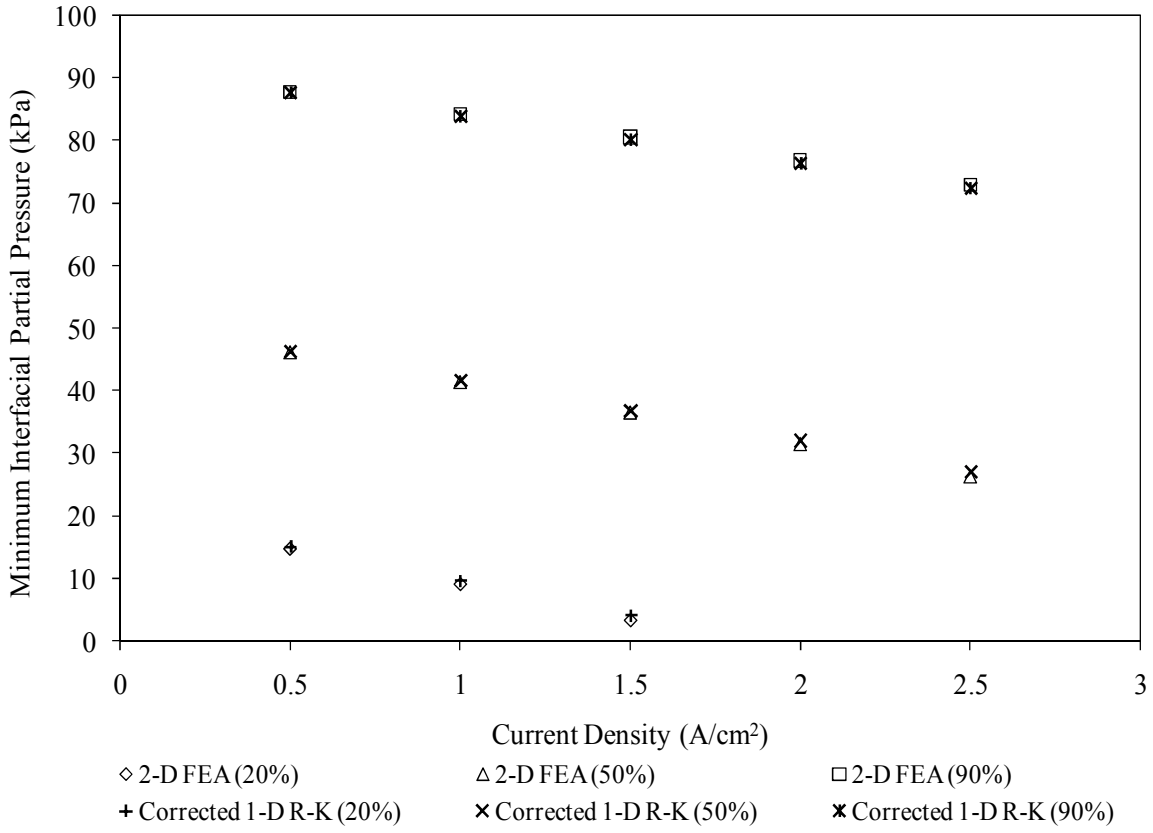

Figure 4.15 Predictions of minimum hydrogen partial pressure at the anode-electrolyte interface based on 2-D finite element DGM solution and corrected 1-D Runge-Kutta solution for three fuel stream hydrogen compositions.

The heightened pressure drop across the lateral direction in SOFC electrodes, seen for the anode in Figure 4.5b and for the cathode in Figure 4.3, could be mitigated by increasing the electrode thickness and button-cell performance can be approached, as shown in Figure 4.5a. These optimal designs can be achieved when the transverse and lateral mass transport resistances are balanced. Defining general electrode geometries based on non-dimensional terms, specifically the length fraction and dimensionless

thickness t^*, provides two means of mapping the inherent trade-offs between mass transport resistance across the electrode thickness and lateral "sheet" resistance effects and determining such designs.

The first method of mapping electrode design trade-offs is through the dimensionless depletion current density, i^*_{dep}. This dimensionless form of the depletion current density, defined in Equation 3-33, provides a gage of the influence of sheet resistance effects on reactant depletion, as shown in Figure 4.16. Here, results for representative length fraction values are mapped over a range of dimensionless thicknesses. As noted, this dimensionless current density can be used to discern where reducing electrode thickness provides a diminishing return for a given interconnect geometry. In general higher length fractions are shown to achieve better performance with respect to mass transfer, demonstrating higher depletion current densities. This enhancement results from reduced constriction, and therefore reduced average transport path lengths, of the molar flux of consumed species. However, this improved performance results in an electrode that is more sensitive to lateral transport effects. Specifically, as t^* is reduced the multi-dimensional effects in the depletion current density (accounted for by the series term in Equations 3-25 and 3-33b) become dominant. For higher length fractions in particular, this influence increases rapidly once t^* is reduced past the optimal value for mass transport performance, the dashed line in Figure 4.16. Thus, sharper peaks are seen for higher length fractions. In addition to considering this increased sensitivity to lateral transport effects, mass transport improvements must ultimately be balanced with ohmic losses caused by geometric effects on electronic transport within the electrode [6, 39, 56].

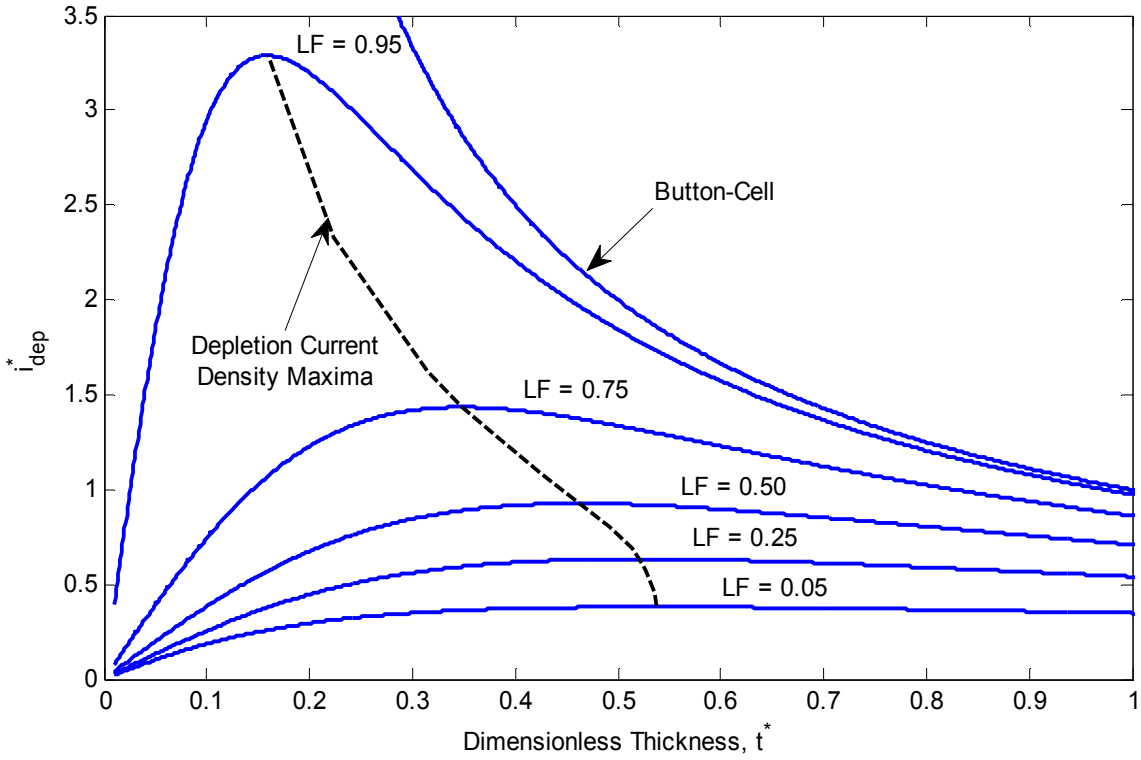

Figure 4.16 Dimensionless depletion current density (—) for a single electrode as a function of dimensionless thickness with a trace of the depletion current density maxima for each length fraction (- -)

The influence of each electrode dimension on this sensitivity can be seen by comparing the terms in the denominator of Equation 3-33b. Investigation of the behavior of each term reveals that before the depletion current density maximum for each length fraction (i.e., the dotted black line in Figure 4.16) the series term that represents multidimensional effects on mass transport overtakes the value of t^*, which represents the influence of electrode thickness, as the dominant term. Each of these terms, and their combined value, are plotted for two different electrode geometries in Figure 4.17. These geometries represent the extremes of the length fraction cases examined (0.95 and 0.05). It is clear that the multidimensional term increases rapidly as t^* is decreased past the optimal value, particularly for higher length fraction values (Figure 4.17a). This stiffness

is mitigated for intermediate length fractions because there is a better balance between the two terms (i.e., the thickness and multidimensional effects). For the lowest length fraction values the influence of the thickness rarely exhibits dominance over transport as shown in Figure 4.17b, and the depletion current density is relatively consistent over the range of t^* values.

The physical basis of this trade-off between electrode thickness and unit cell width can be seen by examining the partial pressure distributions within the electrodes and the corresponding flow fields for reactant diffusion. Four such cases are outlined for anodic hydrogen transport in Figures 4.18 and 4.19. In each of these figures the extreme length fraction cases of 0.95 and 0.05 are examined. Figure 4.18 focuses on an electrode with a higher dimensionless thickness ($t^* = 1.5$), while Figure 4.19 focuses on an electrode with a lower value ($t^* = 0.1$). In the first case, the dominance of thickness is indicated by the orientation of the partial pressure contours and hydrogen flux lines lying primarily across the electrode thickness. This dominance is most evident for the case of $LF = 0.95$ in Figure 4.18a. For the lower length fraction case (Figure 4.18b) the multidimensional effects arising from the constriction of the reactant flow can be seen particularly in the vicinity of the gas channel. Here, the diffusing hydrogen must spread to a greater degree to occupy the anode regions beneath the interconnect rib. These multidimensional effects are amplified for the thin electrode geometry shown in Figure 4.19. Here even the case with the greatest gas channel contact ($LF = 0.95$ in Figure 4.19a) shows multidimensional behavior arising from the constriction of the diffusive hydrogen flow, as noted by the overall composition variation being greatest across the electrode width. For the lowest length fraction in Figure 4.19b, the dominant influence of the unit cell width over

diffusive transport is most evident, with the concentration gradient moving almost exclusively in the lateral direction across the electrode.

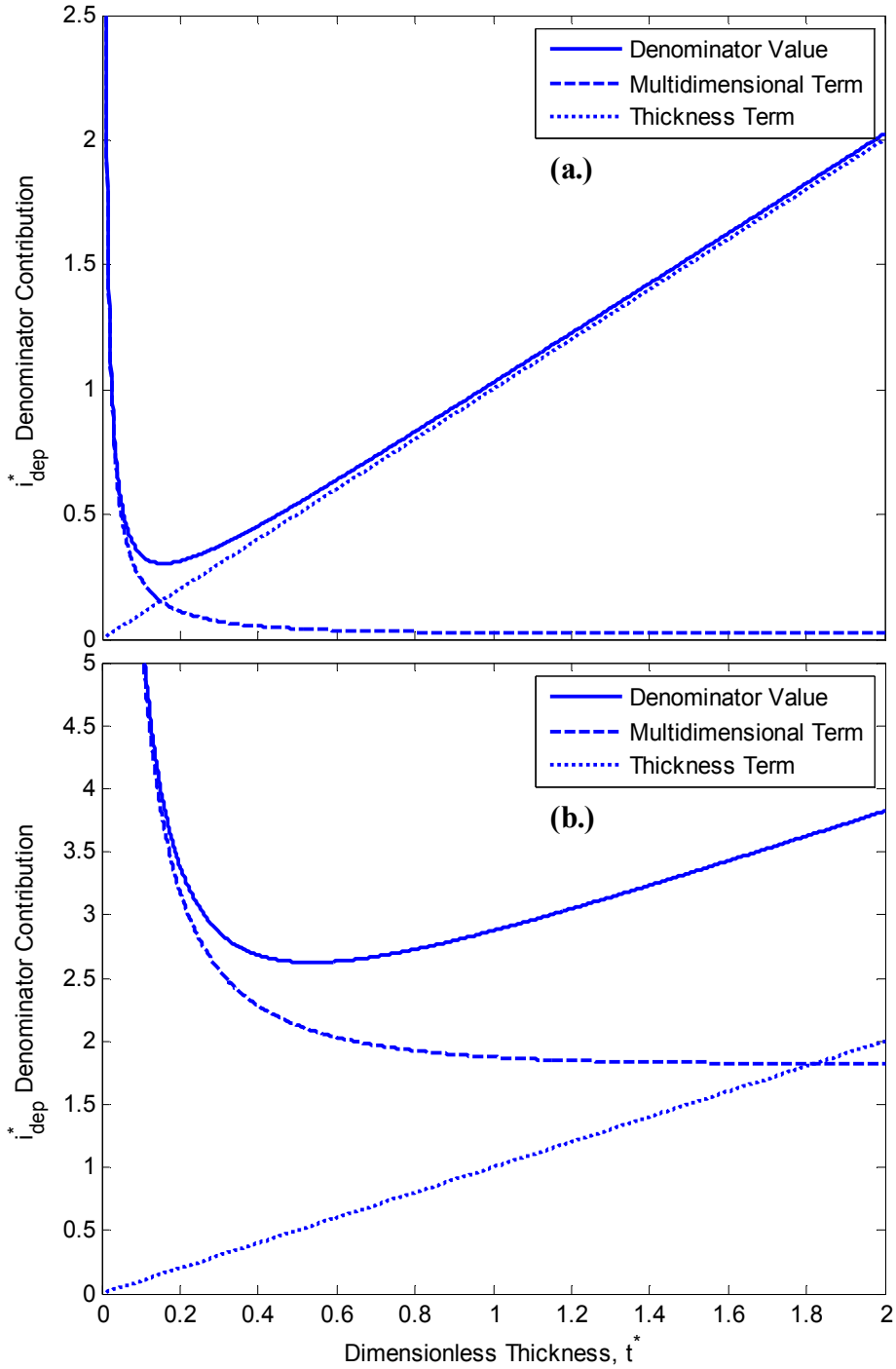

Figure 4.17 Comparison of the contributions of thickness and multidimensional effects to the dimensionless depletion current density for (a.) $LF = 0.95$ (b.) $LF = 0.05$

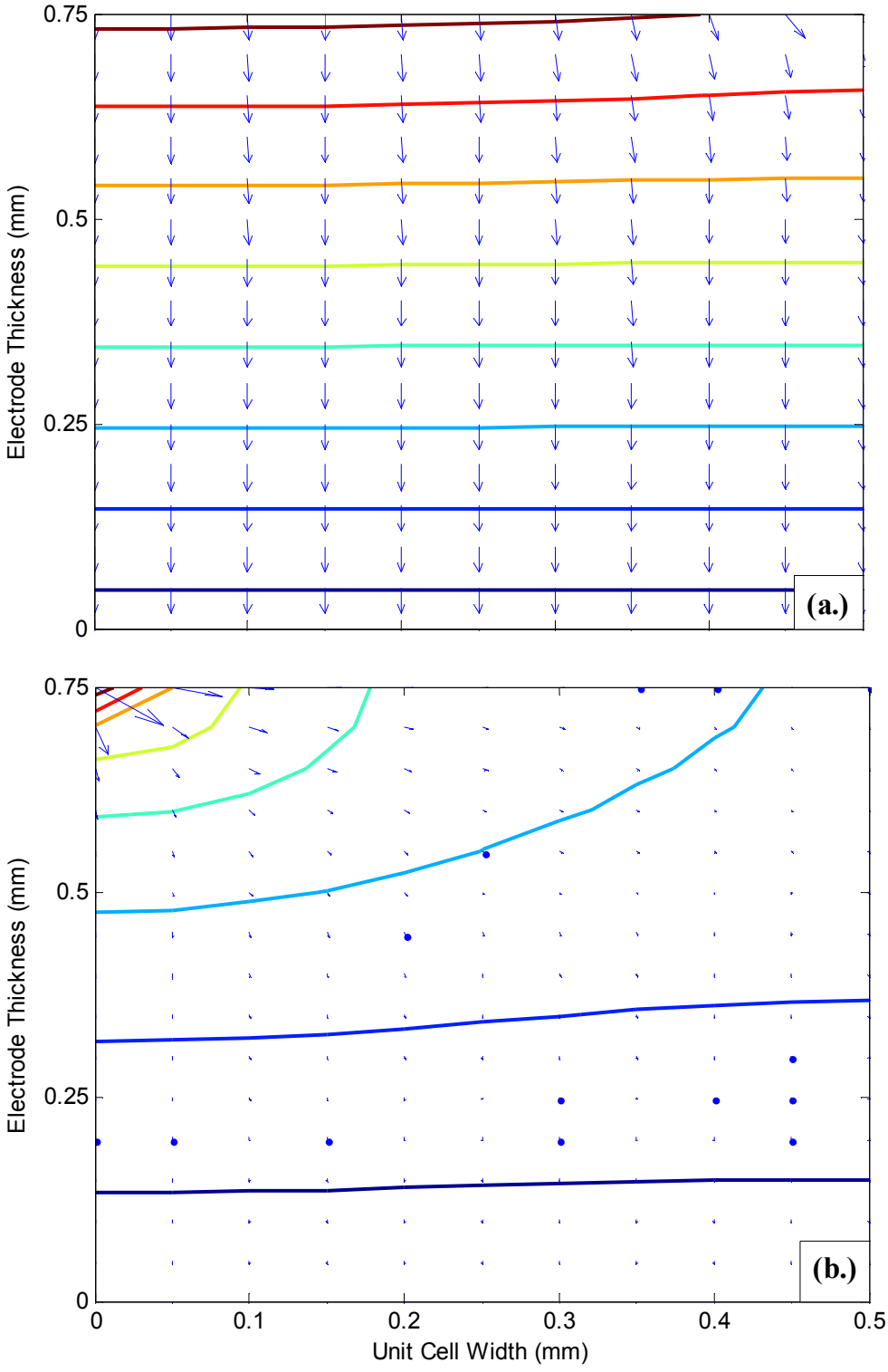

Figure 4.18 Hydrogen partial pressure contours and diffusive flow field for two anodes (a.) $LF = 0.95$ (b.) $LF = 0.05$ with a common dimensionless thickness $t^* = 1.5$

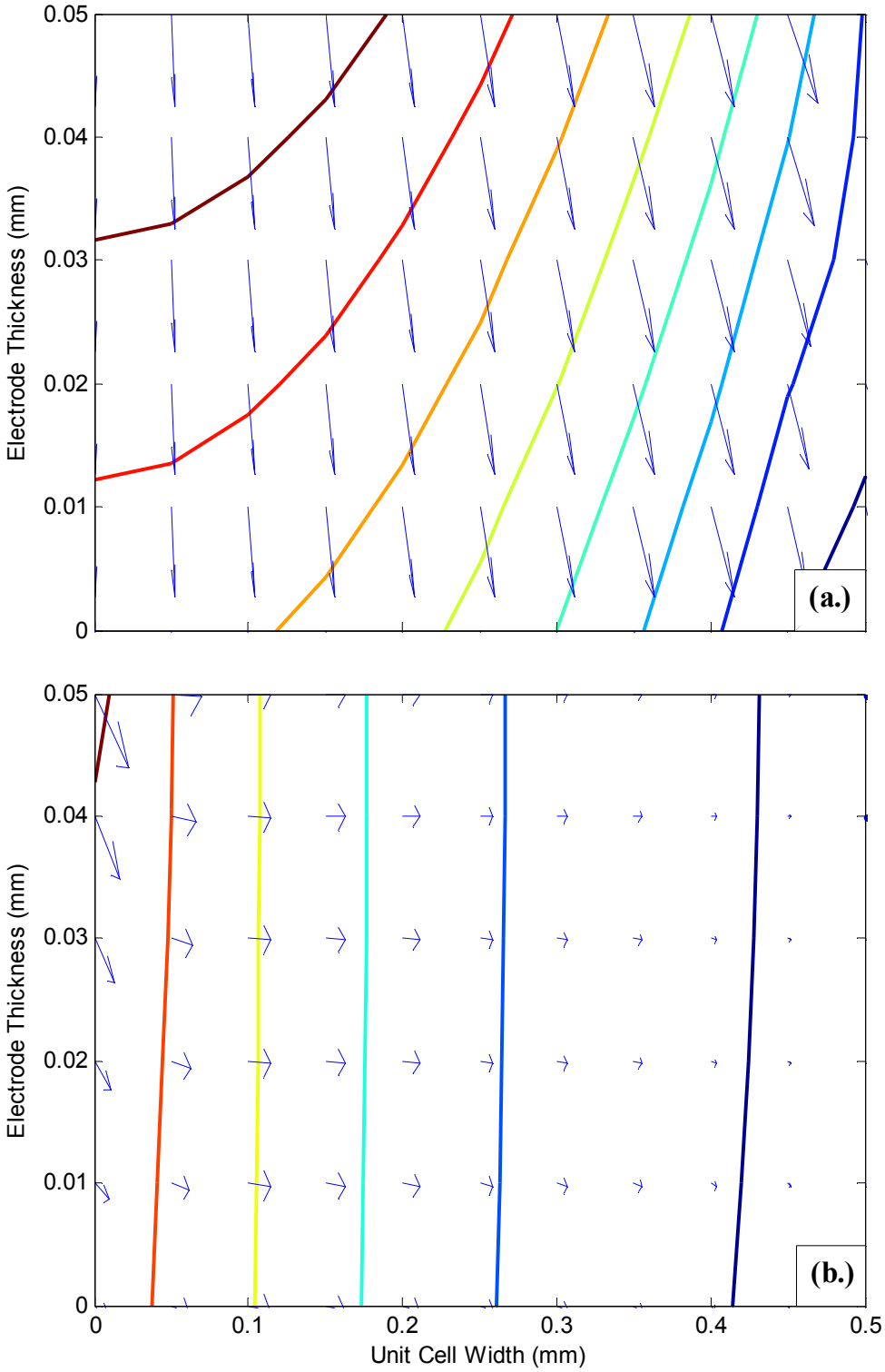

Figure 4.19 Hydrogen partial pressure contours and diffusive flow field for two anodes (a.) $LF = 0.95$ (b.) $LF = 0.05$ with a common dimensionless thickness $t^* = 0.1$

A second tool for mapping SOFC mass transport design trade-offs can be obtained by plotting normalized depletion current density versus the dimensionless thickness, as shown in Figure 4.20. As above, several representative length fractions are shown. This plot allows for prediction of reactant depletion behavior with respect to a button-cell baseline. Thus, performance measurements made from button-cell experimental tests can be modified according to specific interconnect geometry to produce estimates of actual cell performance. The points corresponding to the maxima in Figure 4.16 are also superimposed to provide reference to the limit for electrode thickness reduction.

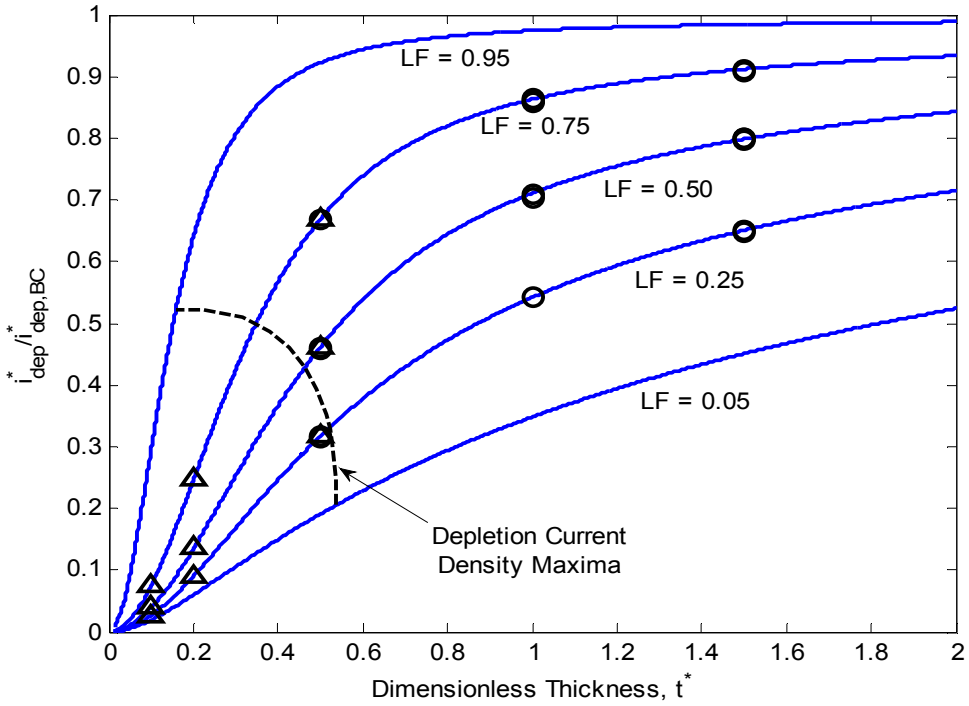

Figure 4.20 Dimensionless depletion current density normalized by the dimensionless depletion current density for the button-cell case as a function of t^* (—) as compared to predictions based on the finite element solution of the dusty-gas model (anode: ○, cathode: Δ); values corresponding to the maxima in Figure 4.16 are also included on the plot (- -)

As with the dimensionless depletion current density, the normalized depletion current density is strictly a function of electrode geometry. As expected, there is strong agreement between this dimensionless performance metric and the DGM finite element results for both the anode and cathode geometries outlined above. These results, based on separate FEA studies of mass transport in single electrodes, are also superimposed on the plot in Figure 4.20. Disagreements for these results primarily stem from variation in numerical accuracy, particularly with respect to predicting a depletion current density based on approximate reactant concentration profiles. Specifically, iteration for depletion phenomena was stopped once a minimum concentration less than 10^{-3} was achieved. There is also some influence of mixture composition on the numerical results, as slight variation is seen in the DGM results depending on whether air (on the cathode side) or binary hydrogen-steam mixtures of varying composition (on the anode side) are considered. For all of the cases shown the average magnitude of error between the predictions is ~0.20 %. The error of greatest magnitude is ~2.1 %, seen for the cathode side with $t^* = 0.1$ and $LF = 0.50$.

Two more key points can be taken from the results shown in Figure 4.20. First, it should be noted that based on the continuum-level models presented electrode geometries commonly applied to cathodes may not be optimal from the standpoint of reactant depletion performance. This observation is corroborated by comparing the pressure distribution in a thicker cathode, shown in Figure 4.21 to that shown in Figure 4.3. The thicker geometry corresponds to a length fraction and dimensionless thickness of 0.50, and produces a significantly higher oxygen partial pressure underneath the interconnect. Thus future air channel and cathode design efforts would benefit from reconsidering the

assumption that cathode mass transport resistance effects can be neglected. Additionally, as the normalized depletion current density approaches unity one can expect that a uniform reactant partial pressure will be seen across the electrode-electrolyte interface when reactant depletion is encountered. Such results are seen in previous modeling efforts based on an anode with t^* = 4 and a length fraction of 0.50 in Figure 4.9. Furthermore, for electrodes with intermediate t^* values relatively uniform reactant distributions may be achieved across the electrode-electrolyte interface, as seen in Figures 4.1, 4.2, and 4.5a. In general, a higher ratio of electrode thickness to unit cell width (i.e., a higher t^*) will result in a more uniform reactant distribution and mass transport performance that asymptotically approaches button-cell performance. Such behavior results from the electrode thickness dominating mass transport as thickness is increased and width is held constant. The increased electrode thickness allows space for reactants to spread more evenly across the unit cell width.

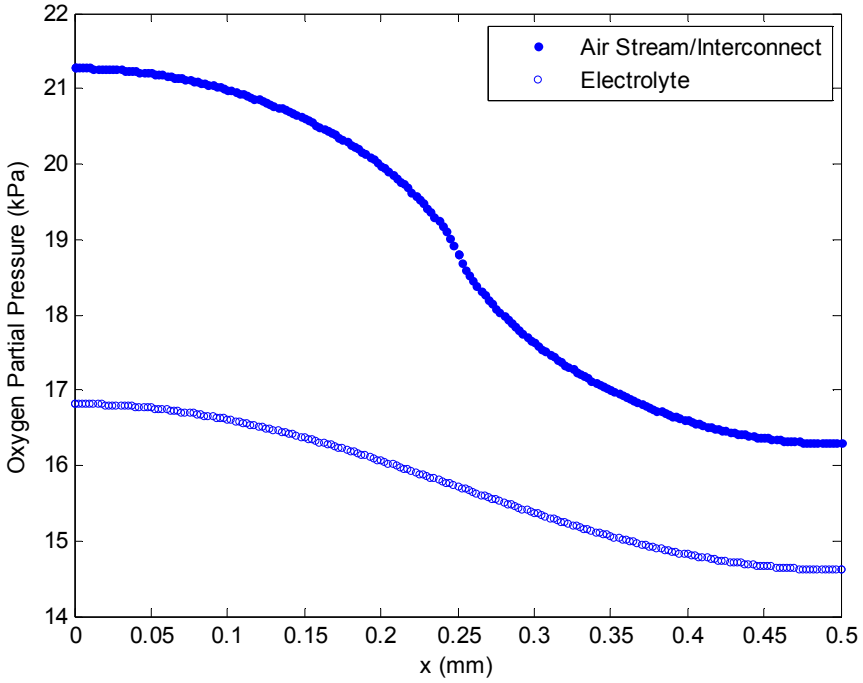

Figure 4.21 DGM prediction of the oxygen partial pressure distribution for a cathode with thickness 250 μm and 1 mm unit cell width (0.5 A/cm^2, 21% O2, $\varepsilon = 0.3$ and $\tau = 5$)

Considering common electrode geometries in light of the trade-offs outlined by the performance metrics above underscores the potential pitfalls of using excessively thin electrodes, which are typically used on the cathode side. The regions where common electrode geometries tend to fall are illustrated in Figure 4.22. Here, common anode and cathode regions are highlighted in blue and red, respectively. The anode commonly serves as the thicker support electrode in SOFCs. As shown in Figure 4.22 anode geometries balance losses associated with the electrode thickness and width and are likely to be less susceptible to pronounced lateral depletion. These thicker geometries are also expected to be less susceptible to molar flux variations along the electrode-electrolyte interface that arise from non-uniform current along the interconnect. On the other hand, common cathode geometries are expected to experience significant lateral variations in reactant composition. Furthermore, these thin geometries are likely to experience

localized increases in molar flux along the electrode-electrolyte interface due to the influence of interconnect contact. For these reasons electrode geometries that balance the key cross-sectional dimensions may be more desirable for mass transport performance.

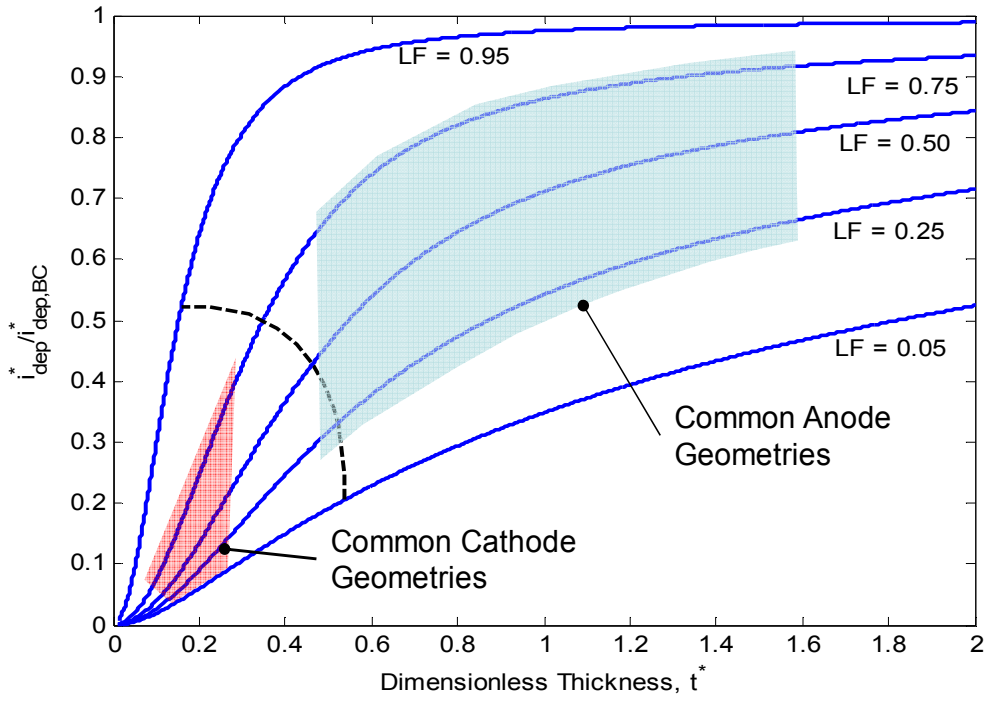

Figure 4.22 Regions representing common anode and cathode geometries (highlighted in blue and red) shown in relation to the normalized form of the dimensionless depletion current density

4.5 Summary

The dimensionless performance metrics presented and analyzed above allow for the straightforward description of how bulk electrode and interconnect design impacts electrode mass transport performance. These metrics lead to the development of design maps that can be readily applied to planar SOFC design. Analysis of these maps highlight potential performance challenges associated mass transport in thin electrodes. These metrics and their associated design maps present useful tools for SOFC design, but

there are possible limitations on the applicability of these metrics and the models applied in their development. As noted, the results presented above are primarily for binary diffusion through SOFC electrodes in the absence of a pressure gradient, and, for thin electrodes, the interaction between mass and electronic transport within the electrode requires more detailed consideration. More notably the application of average microstructural parameters within these models could be fortified by greater consideration of the non-uniform nature of the porous electrode microstructure. The dusty-gas model that is applied as a state-of-the-art benchmark of the simpler potential flow models does not account for this non-uniformity, and alternative models that claim to address shortcomings in the DGM also rely on average properties for the porous medium [62-64]. Finally, the models developed apply the assumption of a planar reaction zone at the electrode-electrolyte interface. In the following chapters fractal modeling approaches common in the study of porous media will be applied toward modeling diffusion within SOFC electrodes. The modeling approach presented applies a more detailed description of the reaction zone in an effort to capture the effects of microstructural variation on electrode performance.

CHAPTER 5

A FRACTAL MODEL FOR SOFC ELECTRODE MASS TRANSPORT

In the present chapter the application of fractal structures as templates for the geometry of the pore space in an SOFC electrode is explored. The simulated fractal pore space serves as the geometric domain for the numerical solution of diffusive mass transport equations within the reaction zone near the electrode-electrolyte interface of the SOFC. In this role, the fractal templates demonstrate the application of fractal modeling approaches to SOFC neutral species transport and enable the investigation of the influence of reaction zone microstructure. Modeling results are compared to published experimental results for concentration polarization measurements [90] and voltage-current characteristics [22].

5.1 Fractal Pore Constructs and Templates

Previously, the term fractal was defined generally as a countable system or set that possesses the same general geometry regardless of scale at which it is viewed. Since each part is geometrically similar to the whole a fractal is self-similar or possesses the characteristic of scale symmetry [65, 67, 68]. In a deterministic sense, fractals are produced by applying contractive transformations to a set with a basic geometry [67]. For example, a line may be reduced in scale and rotated in an iterative manner to form a fractal curve, such as the quadratic Koch curve shown in Figure 5.1. The basic features of this fractal curve may also be constructed by applying a perturbation, or *generator*, to a basic *initiator* as shown. The initiator for the quadratic Koch curve fractal, shown at k

= 0, is a line segment, and the generator for the fractal curve contains a square perturbation, as shown at k = 1. Successive applications of the generator are referred to as *fractal generations* and are numbered accordingly. The second and third generations for the quadratic Koch curve are also shown in Figure 5.1.

A system or set is considered *mathematically fractal* if the process of size reduction can be continued infinitely based on a consistent scaling relation. The scaling nature of such a fractal is described by the *fractal dimension* (D_f), which is defined using Equation 5-1 based on the number of open sets (N line segments, disks, or spheres) of size r covering a given geometry. For example, starting at k = 1 the curves shown in Figure 5.1 may be covered by N = 5, 25, and 125 line segments of length r = 1/3, 1/9, and 1/27. Thus the quadratic Koch curve has a fractal dimension of ~1.465. For a given fractal set D_f has a lower limit based on the topological dimension of the fractal and an upper limit set by the Euclidean dimension of the occupied space. The fractal curves shown below in the two-dimensional plane have a fractal dimension between one (the topological dimension of the curve) and two (the Euclidean dimension of the plane).

$$N(r) = r^{-D_f} \tag{5-1}$$

$$D_f = \frac{\ln N}{\ln(1/r)} \tag{5-2}$$

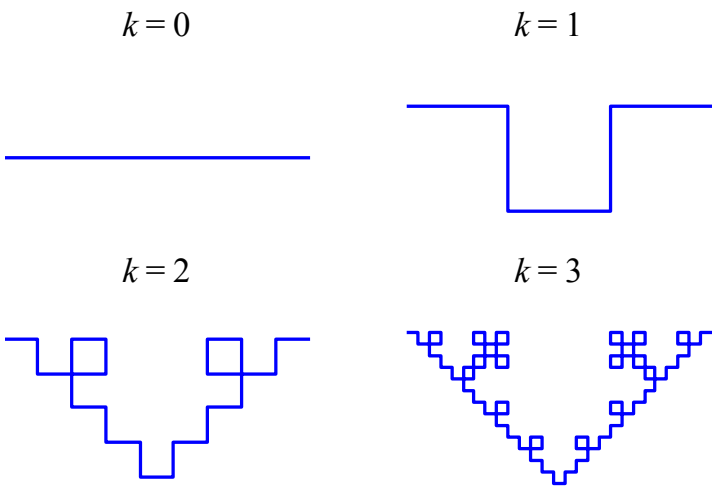

Figure 5.1 Quadratic Koch curve at several fractal generation levels, k (k = 0 represents the initiator of the fractal and k = 1 represents the basic generator that is iterated)

For finite systems, fractal geometric descriptions may be applied if the system can be considered statistically self-similar or treated as prefractal. Such finite systems may also be referred to as a *natural fractal* [68]. The statistically self-similar description of natural fractals applies to geometries with a sufficiently broad range of feature sizes present within the system, e.g. a porous medium where the smallest pore is $1/100^{th}$ the size of the largest pore [65, 69]. The latter description applies to a finite size system in which feature size obeys a scaling relation similar to a mathematically fractal system [70]. These prefractal descriptions may also be applied to porous media, and have received considerable attention in the study of porous catalyst performance [70-74]. Through application of a similar morphological approach fractal structures can serve as templates for the pore structure and allow for the more detailed examination of diffusion phenomena within SOFC pore structures.

In the present work, the quadratic Koch curve geometry illustrated in Figure 5.1 is used to produce basic pore constructs that are combined to simulate a cross-section of the

porous electrode, as shown in Figure 5.2. These constructs are produced starting with an initiator ($k = 0$) with a length equal to a typical pore diameter in an SOFC electrode. This approach allows for the dominant pore size to be constrained while the varying the active boundary geometry and simulating a range of electrode pore sizes comparable to those reported in the literature [21, 51, 90, 91]. The total curve length, surface area, and pore volume for these fractal templates follow basic scaling relations as functions of the initiator length. For a single side of the basic constructs shown the length and surface area of the pore walls can be calculated using Equations 5-3 and 5-4 based on the main pore diameter, d_p, as the initiator length. In the present work, these pore diameters are set based on experimentally observed pore sizes for SOFC electrodes [51, 90, 91]. As will be discussed in later sections, these relations can be used to determine scaling relations between the apparent and actual active lengths for a pore cross-section that may affect electrode transport. Although the present work focuses on length scaling for a two-dimensional cross-sectional model, similar scaling between the apparent and actual surface areas may apply for three-dimensional models.

$$L_{Total} = \left(\frac{5}{3}\right)^{i} d_p \tag{5-3}$$

$$A_{S,Total} = d_p^2 + 4 \cdot \sum_{i=1}^{k} 13^{(i-1)} \left(\frac{d_p}{3^i}\right)^2 \tag{5-4}$$

Due to its scaling nature, the fractal template geometry allows for constraint of the porosity of the medium independent of the pore size. This point is demonstrated by examining the dependence of pore space and total volume for the geometry illustrated in

Figure 5.2. For a given main pore diameter, d_p, volume of the simulated pore space can be defined based on the fractal generation using Equation 5-5 for the cross-sections shown in Figures 5.2a-c, respectively. Similarly, the total volume of the geometry, as bounded by the gray dashed lines in Figures 5.2a-c, can be defined based on the main pore diameter and fractal generation, as in Equation 5-6. Thus, the scaling nature of the fractal structure allows for the constraint of key microstructural parameters.

$$V_p = d_p^3\left[1+4\cdot\sum_{i=1}^{k}13^{(i-1)}\left(\frac{1}{3^i}\right)^3\right] \tag{5-5a}$$

$$V_p = d_p^3\left[1+5\cdot\sum_{i=1}^{k}13^{(i-1)}\left(\frac{1}{3^i}\right)^3\right] \tag{5-5b}$$

$$V_p = d_p^3\left[1+6\cdot\sum_{i=1}^{k}13^{(i-1)}\left(\frac{1}{3^i}\right)^3\right] \tag{5-5c}$$

$$V_{Total} = d_p^3\left[1+2\cdot\sum_{i=1}^{k}\frac{1}{3^i}\right]^2 \tag{5-6a}$$

$$V_{Total} = d_p^3\left[1+\sum_{i=1}^{k}\frac{1}{3^i}\right]\left[1+2\cdot\sum_{i=1}^{k}\frac{1}{3^i}\right]^2 \tag{5-6b}$$

$$V_{Total} = d_p^3\left[1+2\cdot\sum_{i=1}^{k}\frac{1}{3^i}\right]^3 \tag{5-6c}$$

The present work focuses on the application of third generation quadratic Koch curve structures as templates for the geometry of the pore space in an SOFC electrode. Based on Equations 5-5 and 5-6 the third generation fractal constructs shown in Figures 5.2a

and 5.2b have approximate porosities of 0.231 and 0.325, respectively. A third, lower porosity construct can also be introduced (~0.182 for $k = 3$), as shown in Figure 5.2c. Intermediate porosities can be simulated using combinations of these constructs. Furthermore, by varying the fractal generation number and combining basic constructs a broader range of porosities can be simulated. This range of porosities, based on Equations 5-5 and 5-6, is outlined in Figure 5.3. Note that as the fractal generation is increased the porosity for a given construct converges to a set value after approximately the fifth generation.

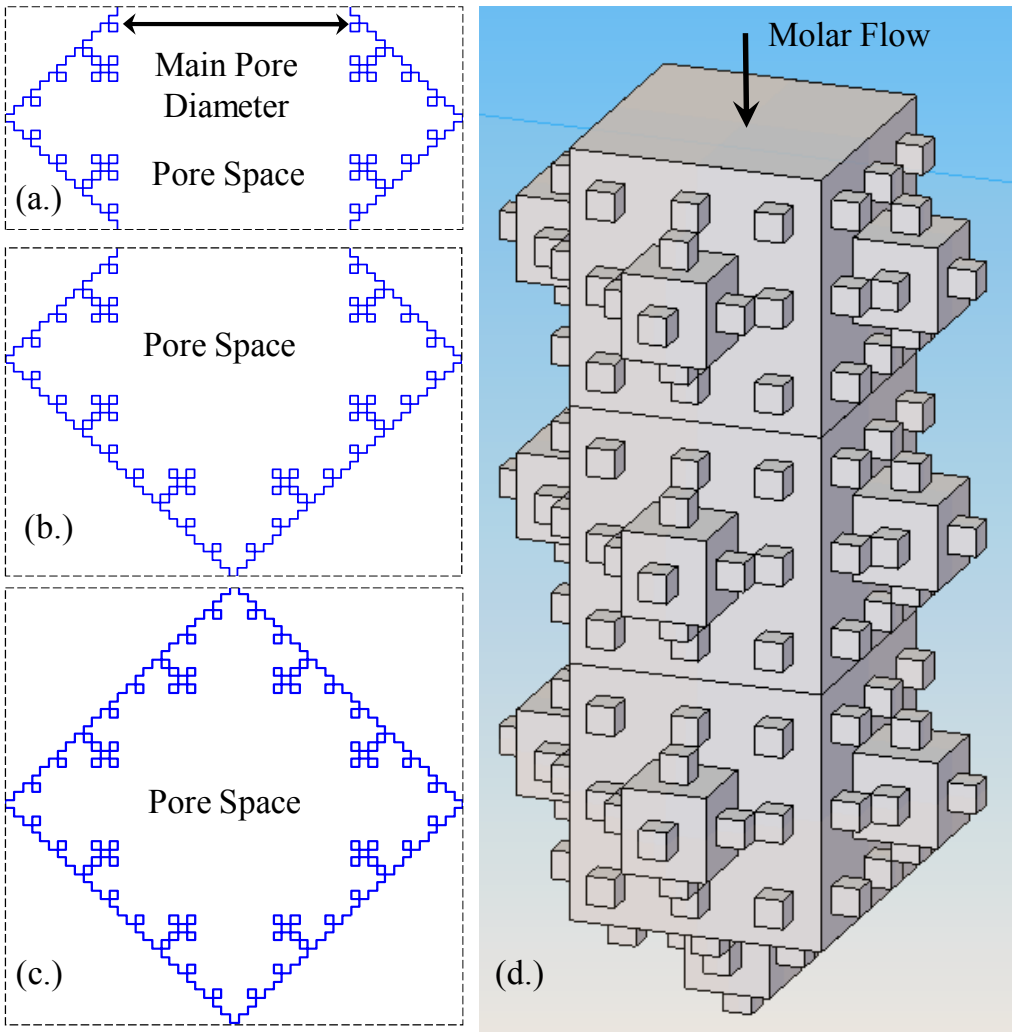

Figure 5.2 Fractal pore constructs (3rd fractal generation) used to simulate multiple porosity values these segments can be combined to simulate the pore space (d.) shown here for the 2nd fractal generation using constructs similar to those shown in (a.) and (b.)

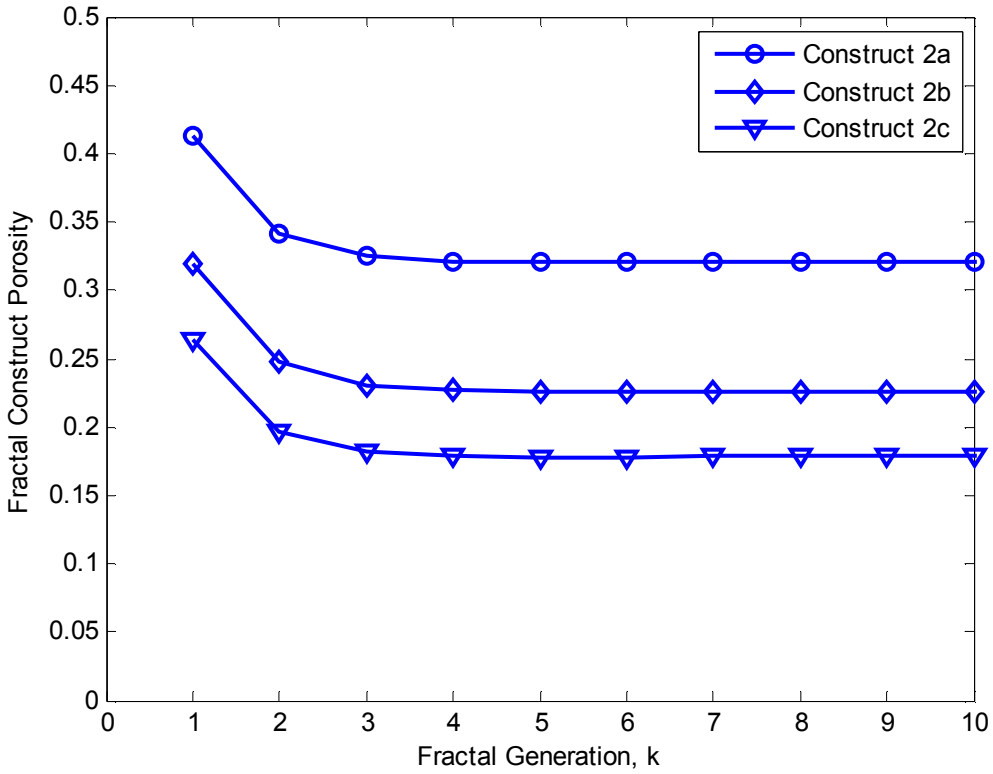

Figure 5.3 Outline of the range of porosities simulated by the fractal constructs shown in Figures 2a-2c as a function of the fractal generation, *k*

5.2 SOFC Electrode Mass Transport Model

In the present work a prefractal model of the pore structure is applied toward modeling diffusion within the electrochemically active region of an SOFC electrode. The porous electrode is separated into bulk and electrochemically active regions. The electrochemically active region is modeled in two-dimensions using a fractal template based on a quadratic Koch curve, which is used to simulate the open pore space. Within the bulk electrode a one-dimensional model is applied based on the dusty-gas formalism, with the molar flux defined for the anode as shown in Equation 5-7. This model is solved for the one-dimensional case using a Runge-Kutta method as outlined in previous chapters. Initially, volume average microstructural parameters, specifically porosity,

tortuosity, and pore size, have been applied within this region in determining the diffusion coefficients. Compared to the standard planar reaction zone assumption, the electrochemically active region of the electrode is modeled in greater detail with a finite element model using a regular Koch pore cross-section as a template for the pore structure, shown in Figures 5.4 and 5.5. The basic fractal structure is iterated to simulate these larger cross-sections of the reaction zone, with the size of this region established *a priori* based on standard estimates of the reaction zone size [21, 22]. While this structure presents an idealized form of the reaction zone, general scaling relations based on such geometries may be applicable to more complex structures [78]. Within the pore space, the gray region shown in Figure 5.5, the molar flux is defined based on separate Knudsen diffusion coefficients for each branch of the fractal structure, as indicated by the superscript *n* in Equation 5-8. This molar flux is applied as the operand in Equation 5-10, and the resulting transport problem for the reaction zone is solved using a finite element approach. A constant composition boundary condition is applied at the opening of the reaction zone region, and constant flux boundary conditions are set within specific branches of the reaction zone structure based on Faraday's law. An example of an active boundary arrangement is shown in Figure 5.5, as indicated by the blue lines.

$$N_i = -\left[\frac{1-\alpha y_i}{D_{ij}^{eff}} + \frac{1}{D_{ik}^{eff}}\right]^{-1} \vec{\nabla} \cdot C_i \tag{5-7}$$

$$N_i = -\left[\frac{1-\alpha y_i}{D_{ij}} + \frac{1}{D_{ik}^{n}}\right]^{-1} \vec{\nabla} \cdot C_i \tag{5-8}$$

$$\alpha = 1 - \sqrt{M_i / M_j} \tag{5-9}$$

$$\vec{\nabla} \cdot N_i = 0 \tag{5-10}$$

Since diffusion within only the open pore space is examined for the prefractal reaction zone structure, the bulk and Knudsen diffusion coefficients applied in Equation 5-8 are left unmodified. Applying unmodified diffusion coefficients will result in higher diffusion coefficients, since the effects of porosity and tortuosity are not contained in the modified coefficient. While the use of modified coefficients is standard, effective coefficients and the associated microstructural parameters are often treated as fitting parameters [21, 22, 58] and thus can mask key physical phenomena within the pore and near the active surface [58, 61]. These modifications were withheld because exploration of microstructural effects was desired.

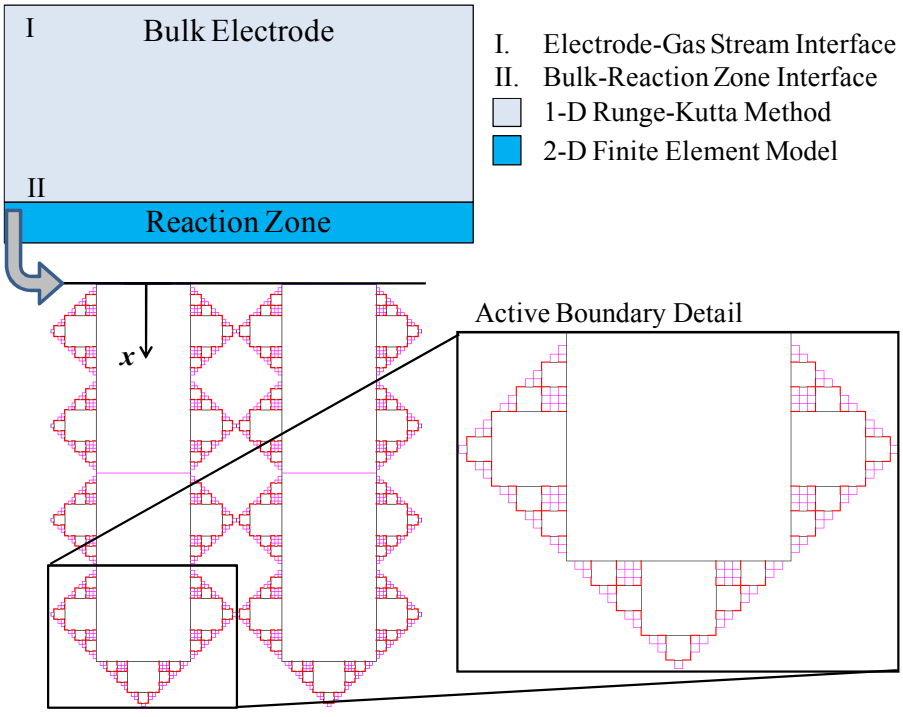

Figure 5.4 Electrode regions and division of modeling types for the fractal SOFC electrode model, for the reaction zone a template based on a 3rd generation Koch curve is shown

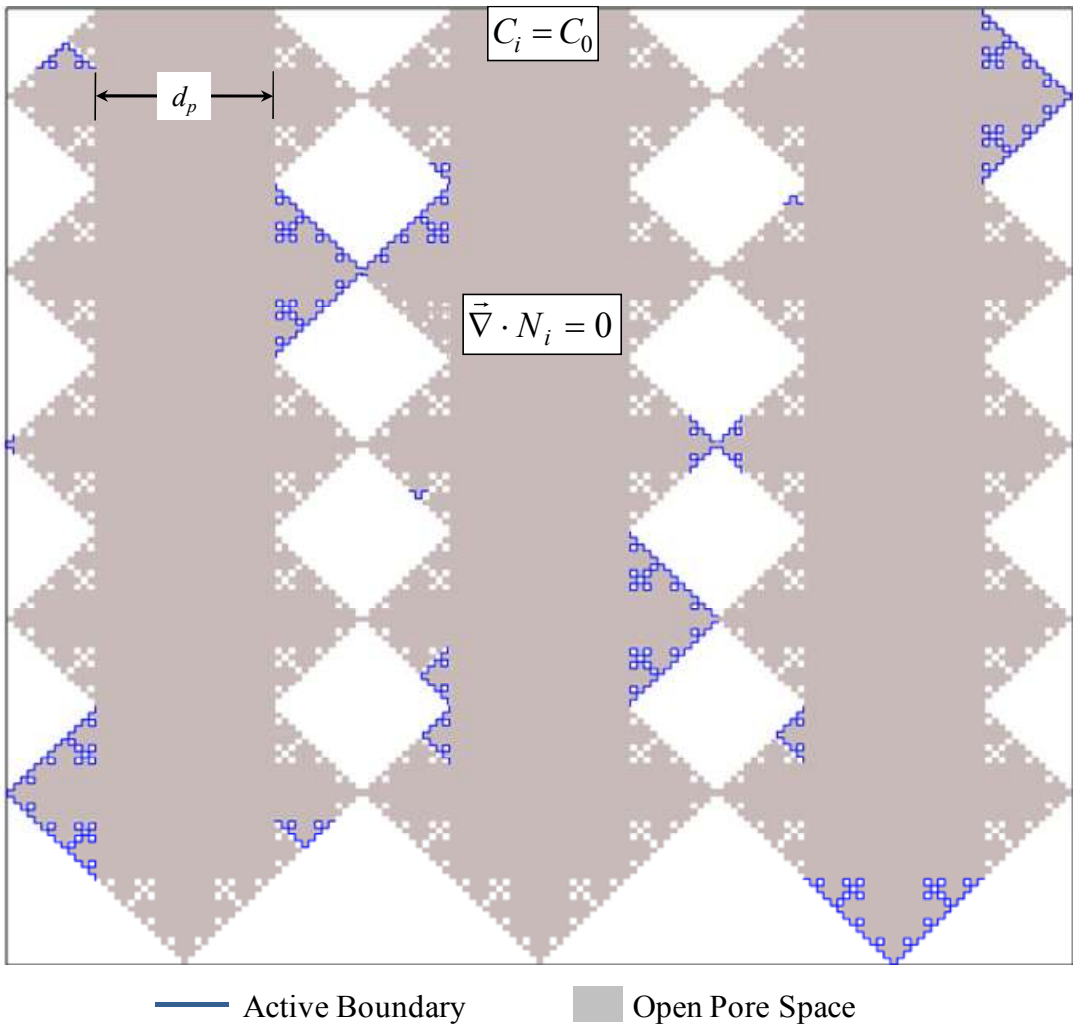

Figure 5.5 Example of pore space domain for the fractal reaction zone model with a dispersion of active boundaries subject to constant Faradaic molar flux; in the open pore space the molar flux (N_i) is defined using the dusty-gas model (Equations 5-8 and 5-12)

For oxygen molar flux through the cathode, expressions similar to Equations 5-7 and 5-8 can be defined, as shown in Equations 5-11 and 5-12. As with previous cathode mass transport expressions, the constant α is not present because the nitrogen in the oxidant mixture (air) is considered stagnant.

$$N_i = -\left[\frac{1-y_i}{D_{ij}^{eff}} + \frac{1}{D_{ik}^{eff}}\right]^{-1} \vec{\nabla} \cdot C_i \tag{5-11}$$

$$N_i = -\left[\frac{1-y_i}{D_{ij}} + \frac{1}{D_{ik}^n}\right]^{-1} \vec{\nabla} \cdot C_i \tag{5-12}$$

In the one-dimensional case, applying the flux expressions in Equations 5-7 and 5-10 as the operand in Equation 5-10 produces a second order ODE for the one-dimensional model, as shown in Equations 5-13 and 5-14. In the reaction zone model, the flux in Equations 5-8 and 5-11 are applied as the operand in Equation 5-10.

$$\frac{d^2 y_1}{dx^2} + \frac{\alpha}{D_{12}^{eff}}\left[\frac{1-\alpha y_1}{D_{12}^{eff}} + \frac{1}{D_{1k}^{eff}}\right]^{-1}\left(\frac{dy_1}{dx}\right)^2 = 0 \tag{5-13}$$

$$\frac{d^2 y_1}{dx^2} + \frac{1}{D_{12}^{eff}}\left[\frac{1-y_1}{D_{12}^{eff}} + \frac{1}{D_{1k}^{eff}}\right]^{-1}\left(\frac{dy_1}{dx}\right)^2 = 0 \tag{5-14}$$

The equations shown above describe binary diffusion and neglect the possible influence of a pressure gradient on transport. An additional case for a ternary mixture (H_2-H_2O-Ar) has been modeled on the anode side to allow for comparison to experimental measurements of concentration polarization. The general molar flux expression and the resulting one-dimensional ODE are shown in Equations 5-15 and 5-16, respectively. The argon diluent in this model is treated as a stagnant gas. Additionally, the fractal reaction zone model for the ternary mixture does not apply effective coefficients, and Knudsen diffusion coefficients are applied for individual branches, as shown in Equation 5-11.

$$N_i = -\left[\frac{1-\alpha y_i}{D_{ij}^{eff}} + \frac{y_{Ar}}{D_{iAr}^{eff}} + \frac{1}{D_{ik}^{eff}} \right]^{-1} \vec{\nabla} \cdot C_i \tag{5-15}$$

$$\frac{d^2 y_1}{dx^2} + \frac{\alpha}{D_{12}^{eff}} \left[\frac{1}{D_{1k}^{eff}} + \frac{1}{D_{1Ar}^{eff}} + (1-y_{Ar}) \left(\frac{1}{D_{12}^{eff}} - \frac{1}{D_{1Ar}^{eff}} \right) - \frac{\alpha y_1}{D_{12}^{eff}} \right]^{-1} \left(\frac{dy_1}{dx} \right)^2 = 0 \tag{5-16}$$

It has been noted that within the bulk electrode pressure gradients may be of significance, a point that has recently received consideration [57]. For the reaction zone, it is assumed that diffusion will dominate because the reduced length scale will result in negligible molar average velocity effects. Based on standard pore sizes for SOFC electrodes, this diffusion will fall within the transition regime. For the cases presented, the width of the main pore and subsequent branches within the fractal structure are set such that transition diffusion is maintained (Kn < 10). Potential surface diffusion effects and chemical reaction mechanisms are not considered within the current fractal models. While these effects are of potential importance, they are removed to allow for focus on the influence of the pore structure.

For the bulk electrode model, the second order ODE describing transport is reduced into two first order ODEs and solved subject to constant composition and molar flux boundary conditions at the electrode-gas stream interface. If only the bulk electrode were modeled, the molar flux boundary condition would be revised based on Faraday's law in conjunction with an apparent electroactive area to ensure that conservation of species is satisfied across the electrode. This particular shooting method was described for the solution of the one-dimensional dusty-gas model in the previous chapter. As noted before, this approach presents a simplified description of the reaction zone region as a

thin plane where the reactant species are consumed. An attempt at relaxing this simplifying planar reaction zone assumption is made through the fractal reaction zone model and its connection with the bulk model, as will be described shortly. This approach focuses on the discrepancy between the real and apparent active length values that are set for the two-dimensional electrode reaction zone cross-section. In the present work, the current density is based on the total active length within the reaction zone region and designated at the active boundaries within the finite element model of the reaction zone; i.e., the electroactive area is not based upon a (nominal) "footprint" electroactive area. Furthermore, through the use of the fractal template for electrode pore geometry increased microstructural detail can be added to account for the impacts of varied pore sizes within the reaction zone. Thus, the shooting method used for solving the one-dimensional transport problem within the bulk electrode is refined through the incorporation of a more detailed description of transport and microstructure within the reaction zone region.

For the finite element model, the reactant composition is set at the opening of the porous structure, location II in Figure 5.4. Constant flux boundary conditions are applied at boundaries within the reaction zone structure that are considered active. An example of these active boundaries is shown in Figure 5.5, indicated by the lines highlighted in blue. The reaction zone model developed allows for variation of the boundaries based on location within the reaction zone and by fractal generation number. These active sites can be evenly distributed throughout the reaction zone or randomly distributed.

Developing an estimate of the hydrogen distribution within both regions of the anode requires connection of the one-dimensional bulk model and the detailed reaction zone

model. As implied above, it is assumed that flux at the active boundaries within the reaction zone drives the molar flux through the electrode. For convenience, this flux is currently set using Faraday's law assuming each boundary supports the same current density value. However, with proper implementation varying local current densities could be set at each boundary. A refined shooting method is applied in which an initial estimate of the molar flux boundary condition in the bulk electrode model is used to set the composition at the openings of the porous reaction zone structure within the finite element model. Based on this interfacial composition setting and the flux boundary conditions in each active branch of the prefractal structure, the finite element model is solved and the flux at the openings of the reaction zone structure is calculated. The hydrogen molar flow into the reaction zone, as calculated by the finite element model, is compared with the Runge-Kutta estimates of the molar flow at the electrode-gas stream interface and at the interface between the bulk electrode and the reaction zone. The flux applied in the one dimensional model is then modified based on continuity for the flow of hydrogen through the electrode until a satisfactory match is seen between all three values. This process is carried out iteratively as outlined in Figure 5.6.

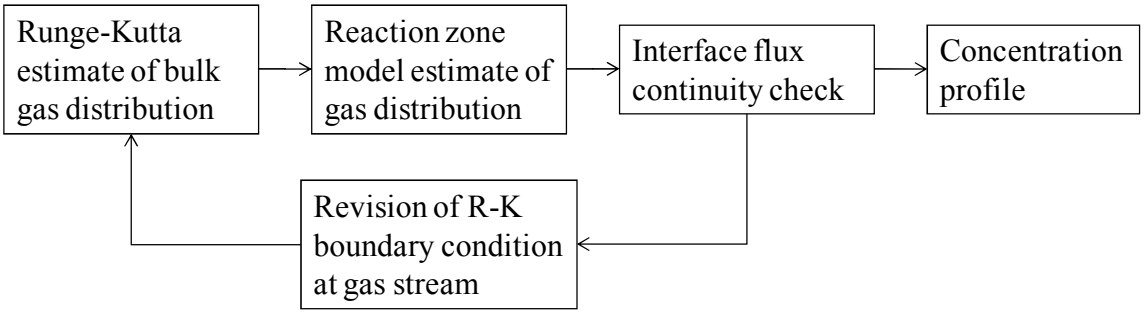

Figure 5.6 Iterative solution process for determining an electrode reactant distribution

5.3 Application to Cell Performance Predictions

The reactant concentration profiles produced by the fractal electrode model can be applied toward estimating cell performance through the calculation of concentration polarization terms, and their subsequent inclusion into the voltage-current relation. These terms are calculated according to Equations 5-17 and 5-18 for the anode and cathode, respectively. In the present work, the minimum reactant composition at each electrode-electrolyte interface was used in these calculations. Over the reaction zone regions examined, the discrepancy between these minimum values and the average values was sufficiently small, so the use of the minimum values was considered acceptable. Cell voltages were calculated according to Equations 5-19 and 5-20. The standard Nernst potential is established as a temperature dependent parameter using techniques outlined by Khaleel et al. [11]. Predicted voltage-current behavior was ultimately compared to experimental results from Zhao and Virkar, so the area specific resistance and activation polarization terms in Equation 5-19 are set using fitted parameters based on the published experimental results [22]. The extent of microstructural characterization varies for the two experimental cases used as benchmarks in the present work [22, 90]. Agreement between the microstructure of the experimental electrodes and the fractal models is addressed in the following sections.

$$\eta_{conc,an} = \frac{R_u T}{2F} \ln\left[\frac{p_{H_2,an-elec}(i'') p^0_{H_2O}}{p^0_{H_2} p_{H_2O,an-elec}(i'')} \right] \tag{5-17}$$

$$\eta_{conc,ca} = \frac{R_u T}{4F} \ln\left[\frac{p_{O_2,ca-elec}(i'')}{p^0_{O_2}} \right] \tag{5-18}$$

$$V_{cell} = E^o - i''\,ASR - a_{act} - b_{act} \ln i'' + \eta_{conc,an} + \eta_{conc,ca} \quad (5\text{-}19)$$

$$E^o = -\frac{\Delta G}{2F} \quad (5\text{-}20)$$

5.4 Comparison to Published Experiments

5.4.1 Prediction of Concentration Losses: Ternary Mixture

To assess the predictive capabilities of the fractal modeling approach the SOFC model using a fractal template for the reaction zone was initially compared to the experimental concentration polarization behavior measured by Yakabe et al. for a ternary mixture of H_2-H_2O-Ar. These published experimental results were chosen to allow for comparison to benchmark models from previous chapters. For the bulk electrode in these studies the average pore diameter and porosity were 2.6 μm and 46%, respectively. The total electrode thickness was set at 2 mm, and a tortuosity of 4.5 was applied within the bulk region. The active region size was set at 10 μm based on literature estimates [21] Fractal templates based on a third generation quadratic Koch curve were applied for the reaction zone model. This particular geometry was selected because its branch sizes cover a range of reported electrode pore sizes [21, 51, 52, 90, 91]. The active lengths shown, approximately 5 and 10 μm, lie below and above the total apparent length of the reaction zone modeled in this case. Based on the cross-sectional area of the region shown in Figure 5.7, these values correspond to an equivalent active length per unit area of approximately 4.2×10^4 and 8.4×10^4 m/m^2, respectively. These values fall within ranges for area specific triple-phase boundary lengths estimated using correlations from Nam and Jeon based on the specified average electrode pore diameter and the porosity [50]. The experimental results are shown in Figure 5.8a-c bracketed by two different active

lengths because few microstructural details are provided for the anode by Yakabe et al. beyond the average pore diameter, porosity, and tortuosity. For additional perspective on the quality of these predictions a one-dimensional DGM assuming a planar reaction zone is compared to the same experimental data in Figure 5.8d. Published modeling results for the one-dimensional DGM are included in this plot [36]. The model that applies a more detailed fractal reaction zone shows better agreement with the published experimental results shown.

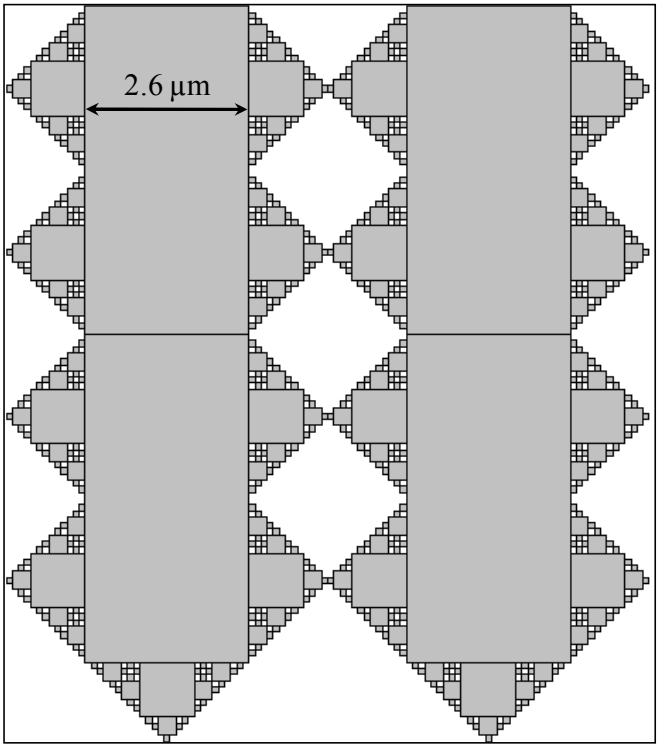

Figure 5.7 Simulated anode reaction zone cross-section applied for fractal model comparison to the experimental results of Yakabe et al. [90]

In general, the fractal model provides a reasonable prediction of performance compared to the experimental results. When compared to the model assuming a planar reaction zone, the detailed reaction zone model shows a tendency to predict higher

concentration polarizations. Most notably, allowing for more detailed description of the reaction zone shows the potential for predicting behavior as conditions that are more likely to result in diffusion limited operation are approached. This potential is particularly evident for the results at 1.0 A/cm^2, an operating point where the planar reaction zone assumption results in a discernible underprediction of concentration losses. While the fractal template approach presents a possible advantage in modeling the anode performance in these cases, there are caveats that must be considered. First, based on the relations outlined in the previous chapter the fractal template predicts a lower porosity within the active region than is seen within the bulk electrode. This lower prediction in the current model may contribute to an overestimate of concentration polarization. Additionally, the two-dimensional implementation of the fractal geometry does not fully account for the complexity of the three-dimensional porous electrode structure [53]. Finally, the intent of the current work is to present the application of the fractal template approach as a means of neutral species transport modeling. Thus, the charged species percolation aspects that would govern reaction zone penetration were not modeled. As noted the reaction zone size was set a priori, so a consistent size was applied for the current densities shown. Percolation aspects could be applied by incorporating solid phases into the template structures.

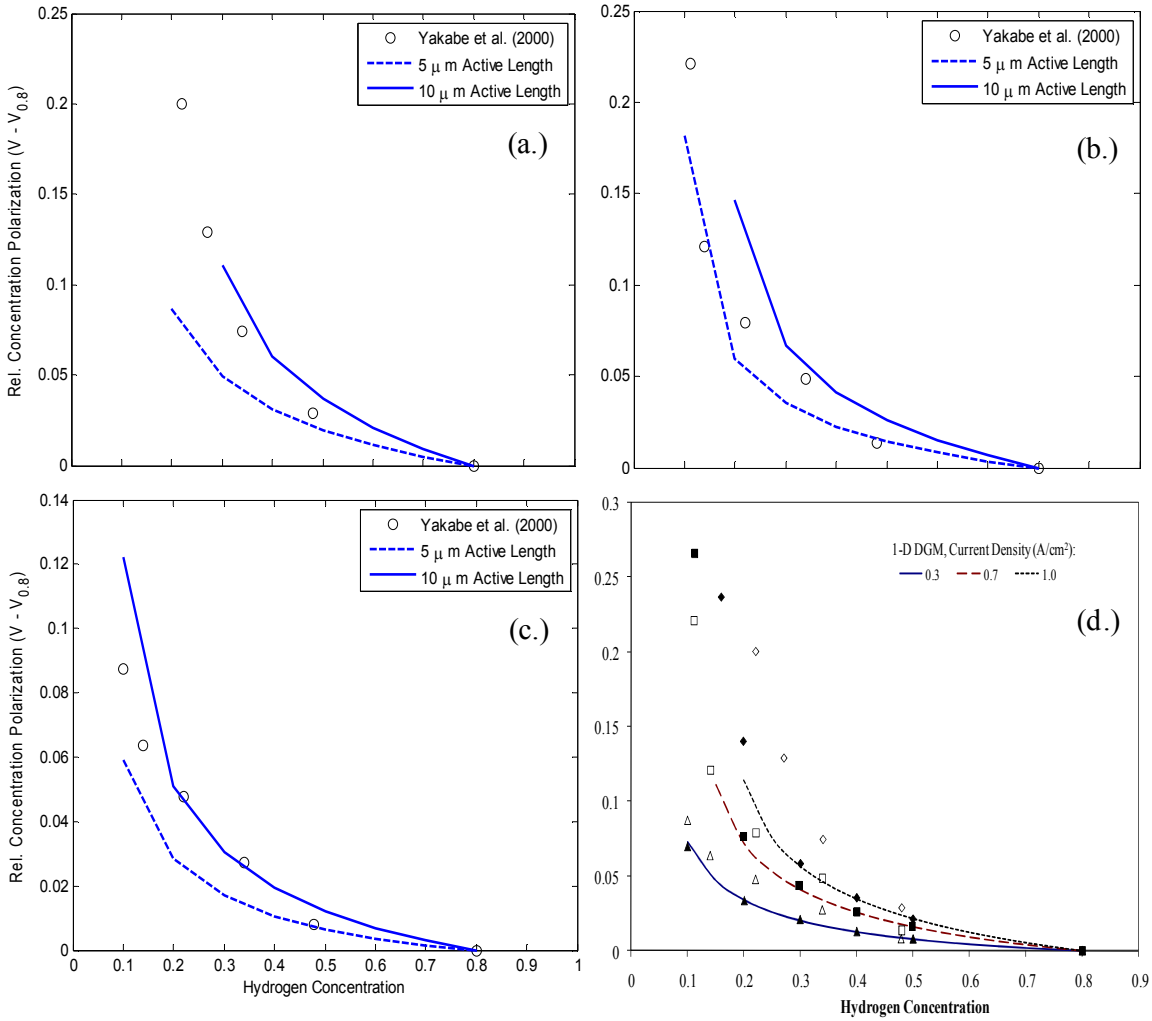

Figure 5.8 Comparison of fractal SOFC electrode model with two different active lengths (5 and 10 μm) to experimental results from Yakabe et al. [90] for a ternary H_2-H_2O-Ar mixture at (a.) 1 A/cm^2 (b.) 0.7 A/cm^2 and (c.) 0.3 A/cm^2; for additional reference, a reproduction of Figure 4-7 is shown in (d.) comparing predictions of the 1-D DGM to the experimental results.

5.4.2 Voltage-Current Performance Predictions

The fractal modeling approach was applied in the calculation of voltage-current characteristic curves with the results compared to the experimental results of Zhao and Virkar [22] to further review the predictive capabilities of the fractal electrode modeling approach while mitigating the discrepancy seen between the porosity of the anode and the simulated reaction zone in the results above. These experiments were chosen because the

electrodes (both the anode and the cathode) were produced in two distinct regions: a bulk support region and an active interlayer. The interlayer regions for the anode and the cathode have substantially lower porosities than the bulk region (23% and 26%, respectively). These interlayer regions can be simulated to within a reasonable accuracy using the fractal constructs outlined in the previous chapter. The cross-sections of these simulated interlayer regions, which will be analyzed using the combined bulk-reactive zone model, are shown in Figures 5.9a and 5.9b for the anode and cathode interlayers, respectively. Both simulated interlayers have approximate thickness of 20 and 20.7 μm for the anode and 20.8 μm for the cathode, respectively. The simulated anode region corresponds to a porosity of 23.1%, and the simulated cathode region to a porosity of 26.6%.

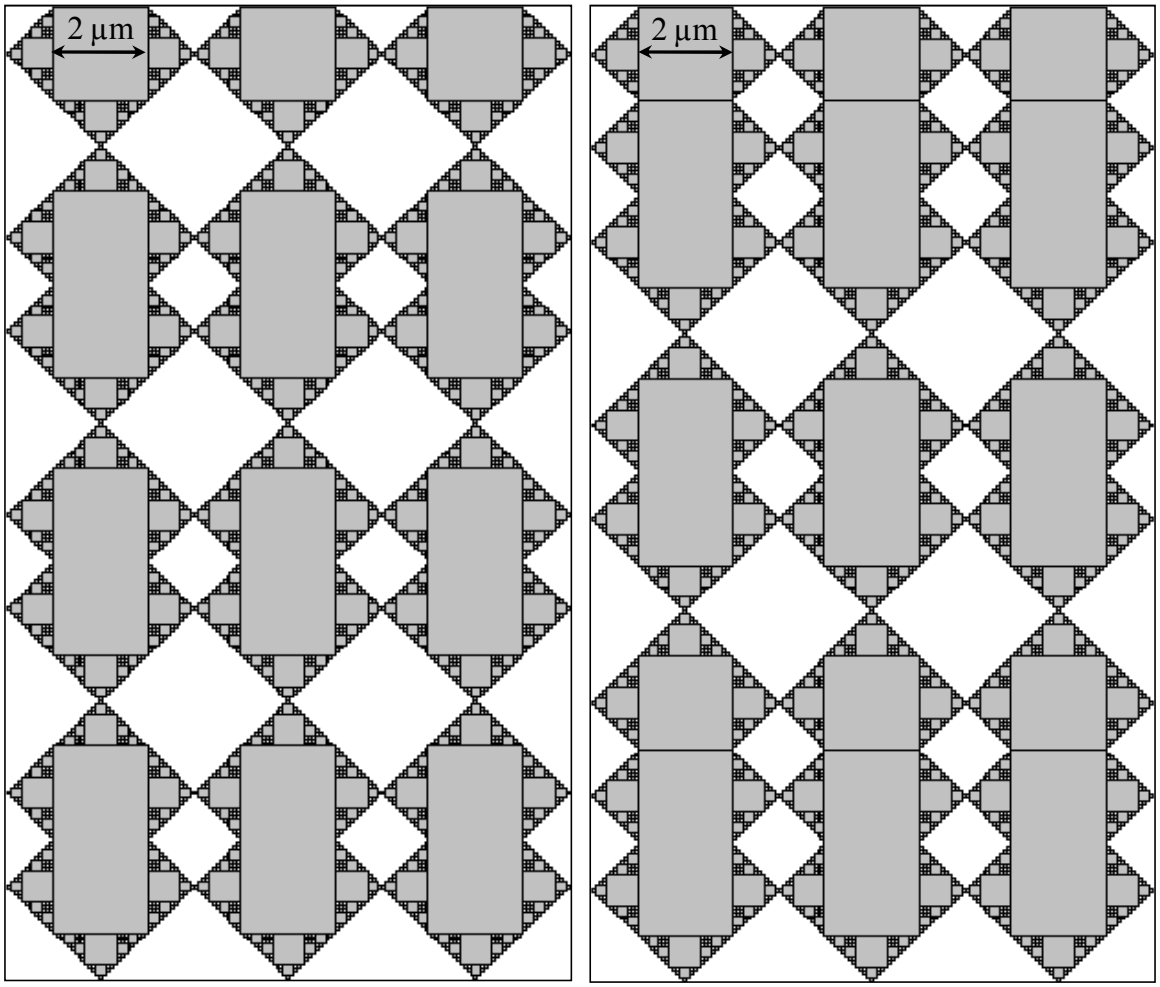

Figure 5.9 Simulated interlayer region cross-sections for (a.) the anode and (b.) the cathode applied for fractal model comparison to the experimental results of Zhao and Virkar [22]

One key shortcoming of the electrode microstructural parameters provided by Zhao and Virkar is that pore sizes for the electrodes examined are not provided. Instead, empirically modified effective diffusion coefficients are applied to standard binary diffusion coefficients. The above plots were produced assuming a 2 μm pore diameter. To check the quality of this assumed pore size and provide a benchmark to the performance of the combined model, tests based on a dual zone dusty-gas model of

electrode transport were run for of the electrode geometries examined. These include four cases with variable anode support porosity and fixed anode support thickness (1 mm, Figure 5.10) and four cases with variable anode support thickness and fixed anode support porosity (48%, Figure 5.11). In all the cases shown the cathode current collector region was 50 μm thick with a porosity of 45%. Based on the effective diffusion coefficients presented by Zhao and Virkar, estimated tortuosity values ranged from 5-11 for the anode support and were consistent at 5.74 for the cathode current collector. For the interlayer regions of each electrode the corresponding tortuosities are significantly higher (20-22 for the anode and 11-12 for the cathode). Experimentally measured geometric tortuosities are typically in the range of 2-6, but may be as high as 10 [21, 58]. Thus, values for the support regions can be considered reasonable. For the interlayer regions the elevated tortuosity values are questionable. For the standard 1-D DGM applying the planar reaction zone assumption the elevated tortuosity values were preserved for the interlayers. These tortuosity values were not applied to the fractal interlayer models.

In general the DGM results with the assumed pore size of 1 μm compare well to the experimental results. However, as shown in the case for 32% porosity in Figure 5.10a even with the elevated tortuosity values the DGM does not capture the details of the concentration polarization behavior for the cell. This fact can also be seen in comparing limiting current values predicted by Zhao and Virkar to general trends seen in the voltage-current curves. For example, in the 32% porosity case (Figure 5.10a) and the 1.5 and 2.45 mm cases (Figures 5.11c and 5.11d) Zhao and Virkar predict limiting currents

of 4.49, 8.75, and 5.58 A/cm^2, all of which are well above the limiting current values suggested by the experimental trends.

Three active length cases were considered for the simulated reaction zones shown in Figures 5.10 and 5.11: 15, 20 and 25 μm. These larger values were used to investigate the impact of a larger active length on the voltage prediction capabilities of the fractal model. They correspond to a range of active lengths per unit area for 6.0x10^4 to 1.0x10^5 m/m^2, based on the cross-sectional area of the region. Similar to the cases compared to Yakabe et al., **t**hese values fall within ranges for area specific triple-phase boundary lengths estimated using correlations from Nam and Jeon. The ohmic and activation loss terms were based upon fitted parameters from Zhao and Virkar [22]. Thus the error seen between the model and experimental result in the operational regions dominated by activation loss is considered to be an artifact of these fitted parameters. Within the operational regions dominated by ohmic loss the standard DGM and the lowest active length case (15 μm) exhibit the best match to the results. Due to prediction of higher concentration loss contributions the higher active length cases overestimate losses within these regions.

The key distinction between the fractal models and the standard DGM with a planar reaction zone is seen at higher current densities. This is evident for the case shown in Figure 5.10a. In these operational regions accounting for reaction zone detail captures concentration polarization for this case with the lowest bulk porosity (32% porosity). Concentration polarization behavior can also be seen for the case in Figure 5.11d (48% porosity and 2.45 mm thickness). For the other electrode geometries examined ohmic losses appear to dominate performance across the range of current densities examined.

However, the impact of accounting for reaction zone details can still be seen in most cases, particularly as current density increases. It is also evident that incorporating reaction zone details alone does not capture the full concentration loss behavior. This discrepancy suggests that while reaction zone details may be incorporated through the fractal modeling approach additional mechanisms may require consideration.

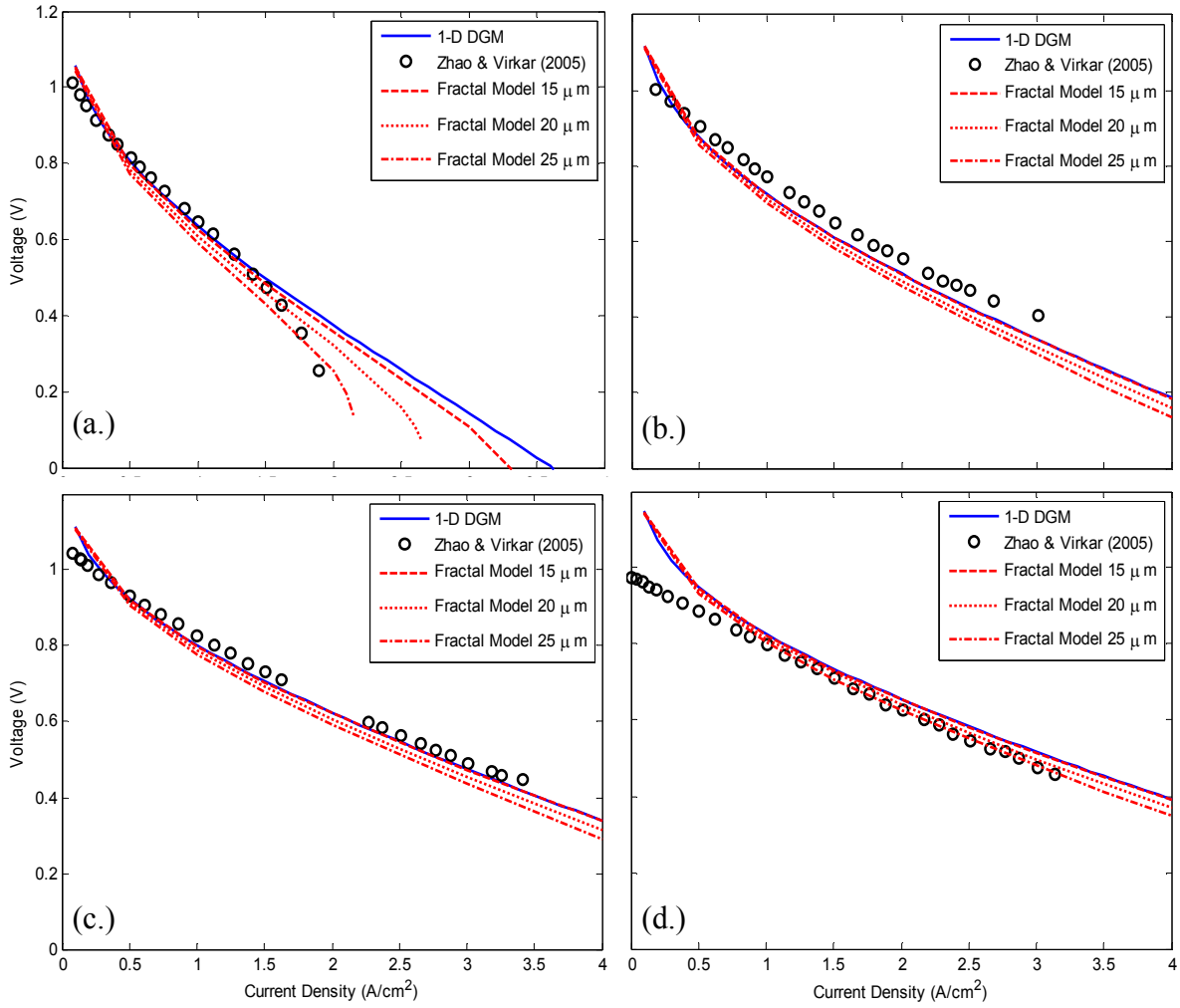

Figure 5.10 Voltage current characteristics for cells with anode support porosities of (a.) 32% (b.) 48% (c.) 57% and (d.) 76%; all case have anode support thickness of 1 mm based on experimental measurements [22]; numerical results included are for 1-D DGM and three cases of the fractal model with active lengths ranging from 15-25 μm

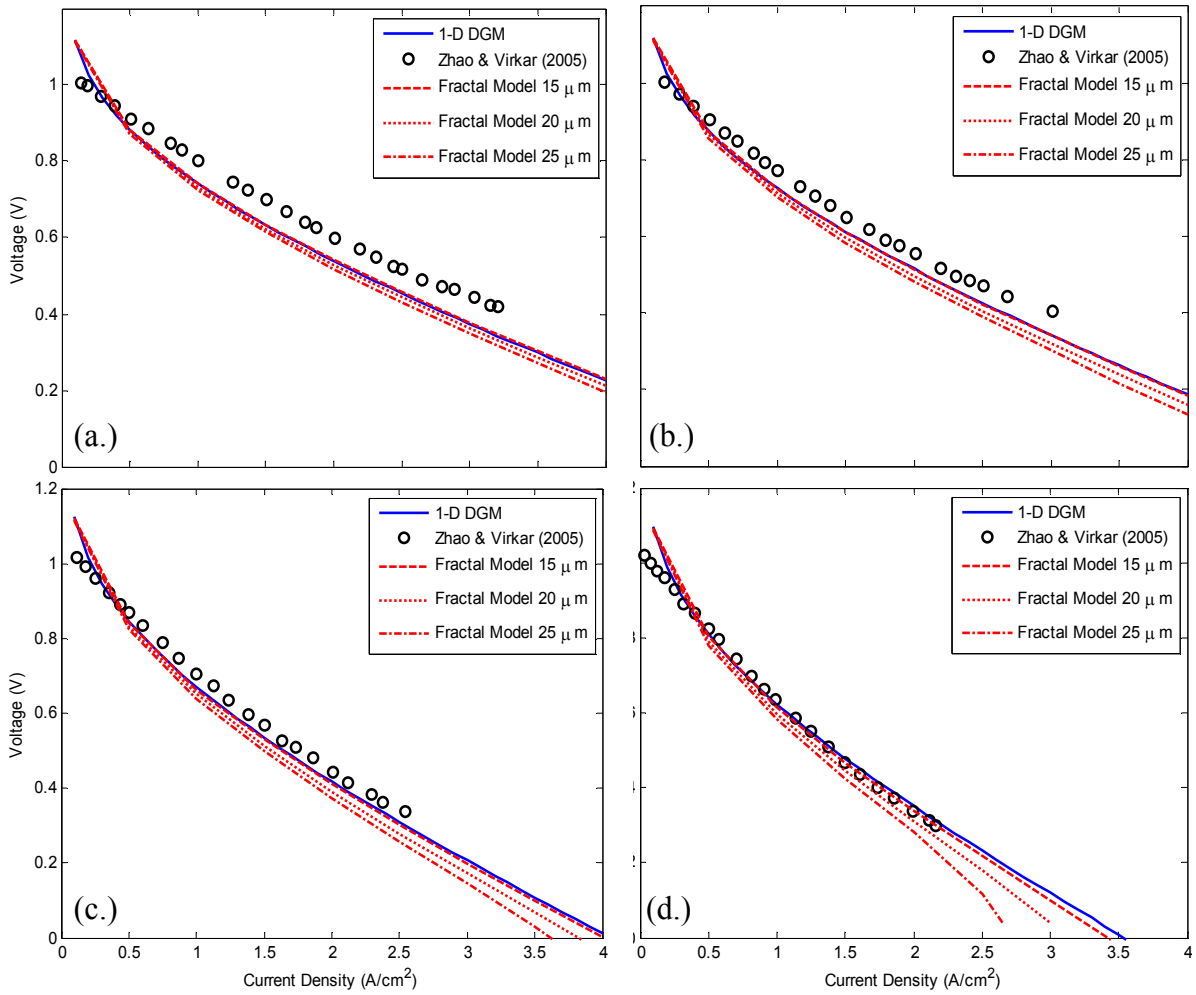

Figure 5.11 Voltage current characteristics for cells with anode support thickness of (a.) 500 μm (b.) 1.0 mm (c.) 1.5 mm and (d.) 2.45 mm; all case have anode support porosity of 48% based on experimental measurements [22]; numerical results included are for 1-D DGM and three cases of the fractal model with active lengths ranging from 15-25 μm

5.5 Summary

A fractal modeling approach for SOFC electrodes has been developed in which the electrode is separated into bulk and reaction zone regions. The bulk electrode region is modeled using a standard one-dimensional dusty-gas model approach. The reaction zone is modeled using a two-dimensional fractal template to simulate the structure of the open pore space. Within this domain the equations governing mass transport are solved using a finite element solution of the dusty-gas model. This combined model provides an

accessible means of numerically predicting electrode performance while giving greater consideration to important microstructural details within the reaction zone. Compared to published experimental measurements of concentration polarization and voltage-current performance for multiple electrode geometries this fractal electrode model presents reasonable performance predictions and captures concentration polarization behavior that is not predicted when assuming a planar reaction zone.

The fractal model presented above allows for the investigation of the performance impacts of the microstructure within the electrode reaction zone, particularly with respect to active length, pore size, and the placement of active boundaries. In the following chapter, numerical studies applying this fractal model will be used to determine the relative importance of these parameters. Furthermore, the fractal model presented leads to a method of assessing porous catalyst performance that can be readily adapted to the assessment of microstructural influence on SOFC neutral species transport.

CHAPTER 6

FRACTAL SOFC ELECTRODE MODEL: RESULTS AND ANALYSIS

The present work focuses on mass transport within the SOFC electrode; an array of modeling studies was run as a means of exploring the impact of operational and microstructural parameters on mass transport behavior. Fractal templates based on a third generation quadratic Koch curve were applied as models of the reaction zones within the anode and cathode. For the cases examined, the active length within the reaction zone model was set to a fixed value and specific branches were activated based on random placement of the flux boundary condition within the fractal model. These fixed active lengths correspond to concentrations of active boundaries per unit cross-sectional area. For the results presented, the pore walls and all of the fractal generations within the pore model were allowed to be activated. Initial studies on the anode side focused on the impact of active length setting and operational variables, current density and fuel stream composition. The effects of flux boundary condition placement and branch activity based on fractal generation are also addressed.

6.1 SOFC Performance Investigations Using a Fractal Approach

6.1.1 Investigations of Anode Performance

6.1.1.1 The Impact of Active Length and Operational Variables

For a binary H_2-H_2O mixture an SOFC anode with thickness of 750 μm, a bulk porosity of 0.3, and a bulk tortuosity of 5.0 was examined following previous studies [6, 39, 56]. An unmodified tortuosity is applied in these cases because, as noted above, an

elevated effective tortuosity may inaccurately account for the influence of phenomena that are neglected in the present model [57, 58, 61]. Initial studies were run for a fixed pore size with all levels of the fractal structure allowed to be active. The pore size was set at 2 μm (hydraulic) diameter for the main pore region, and active boundaries were set randomly throughout the structure. Two active length settings are shown for the reaction zone model: 15 μm and 20 μm. Based on the cross-sectional area of the region shown in Figure 6.1, these values correspond to an equivalent active length per unit area of approximately 1.16×10^5 and 1.55×10^5 m/m^2, respectively. These higher active lengths were chosen because they were greater than the apparent length of the reaction zone model for a 2 μm pore size (shown in Figure 6.1). Exploration of the impact of increased active length values was preferred. Three fuel stream hydrogen compositions were investigated: 20%, 50%, and 90%. Current density settings from 0.5-2.0 A/cm^2 were examined.

Initial modeling results for this anode geometry are shown in Figure 6.2. Here, the minimum hydrogen partial pressures predicted by a one-dimensional DGM assuming a planar reaction zone are compared to the model with the more detailed treatment of the reaction zone. The topmost curves on each of the plots represent the results for the dusty-gas model with a planar reaction zone. As the active length in the model is increased, indicating a higher concentration of reaction sites, the minimum partial pressure decreases. With increasing current density, a greater difference is seen between each case. This discrepancy suggests that reaction zone geometry may play a role in reduced limiting current predictions that are often produced through application of an elevated effective tortuosity.

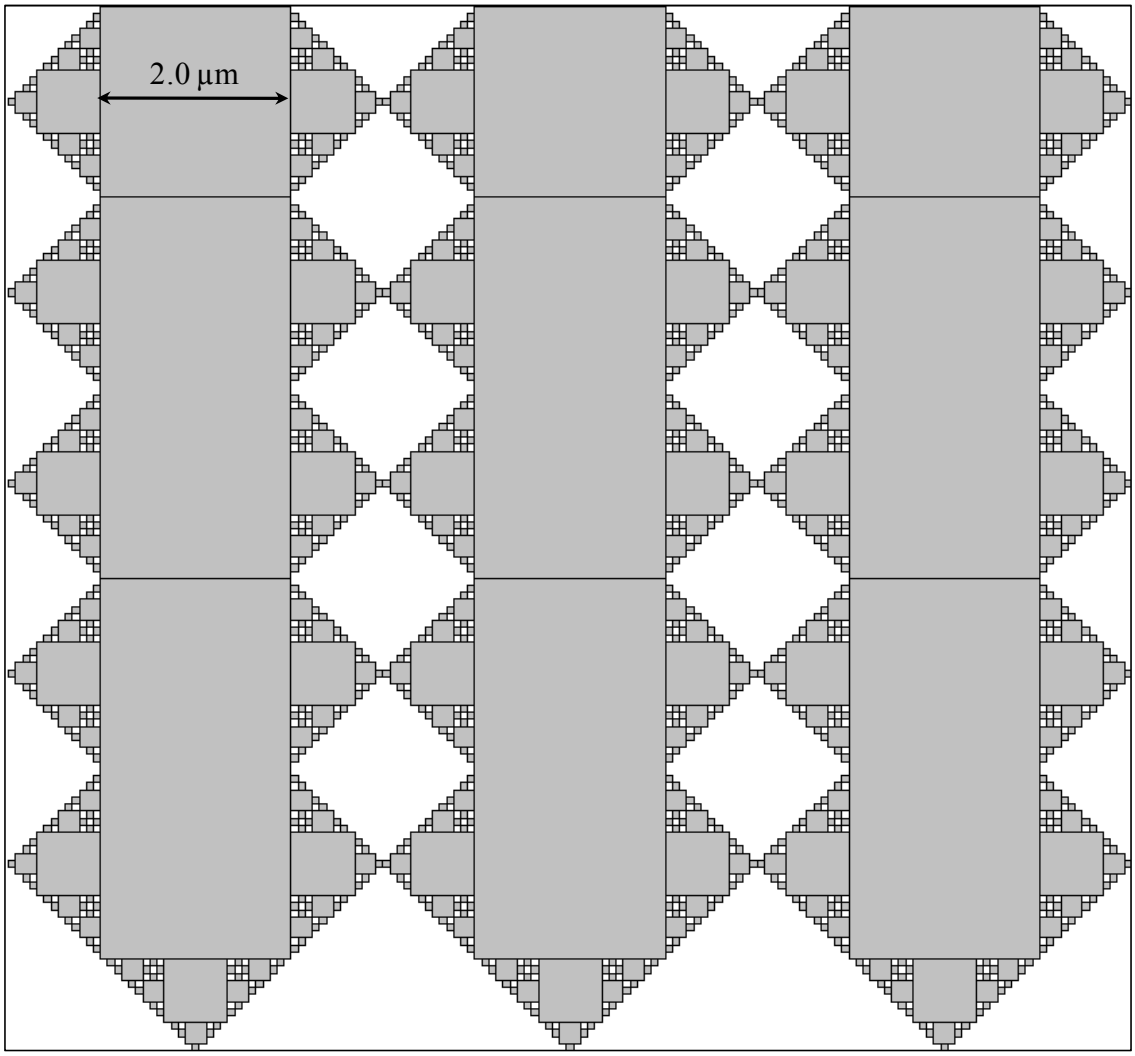

Figure 6.1 Simulated electrode reaction zone geometry for 2 µm pore size; approximate dimensions are 11.78 µm x 10.96 µm

One potential cause of the discrepancy between the fractal and planar reaction zone approaches lies in how the molar flux boundary conditions are scaled. The planar reaction zone approach applies the molar flux boundary condition over the apparent area of the electrode based on the "footprint" of the cell, which may underestimate the active area. The fractal reaction zone model applies an unreduced active area near the electrode-electrolyte interface and uses that active area (or length in the two-dimensional

model) as a basis for calculating the molar flow through the electrode. Thus, a flux based on Faraday's Law can be applied over an active area that may be larger than the apparent area based on the cell footprint. The molar flow at the gas stream-electrode interface is subsequently modified to reflect this reaction zone influence on molar flow. This approach establishes the current density based on the active area within the reaction zone, as opposed to being based on the apparent cell footprint area. However, it should be noted that designation of the current density could be based on the apparent footprint area, with the current densities at active boundary scaled accordingly. In either scenario, the more detailed fractal model of the reaction zone allows for investigation of the impacts of reaction zone geometry on cell performance.

If the effect of the more complex reaction zone geometry were a simple scaling relation based on the increased active length at the interface one would expect to see a single multiplier applied based on the ratio of the active and apparent lengths. While it is possible that such a scaling relation may dominate cell mass transport performance, Santra and Sapoval suggest that additional factors may arise from pore geometry that leads to the chemically active sites within a catalyst, including surface accessibility [70]. Discerning between these scaling and accessibility effects requires additional exploration of mass transport dependence on active length and the characteristics of the fractal template applied for the reaction zone.

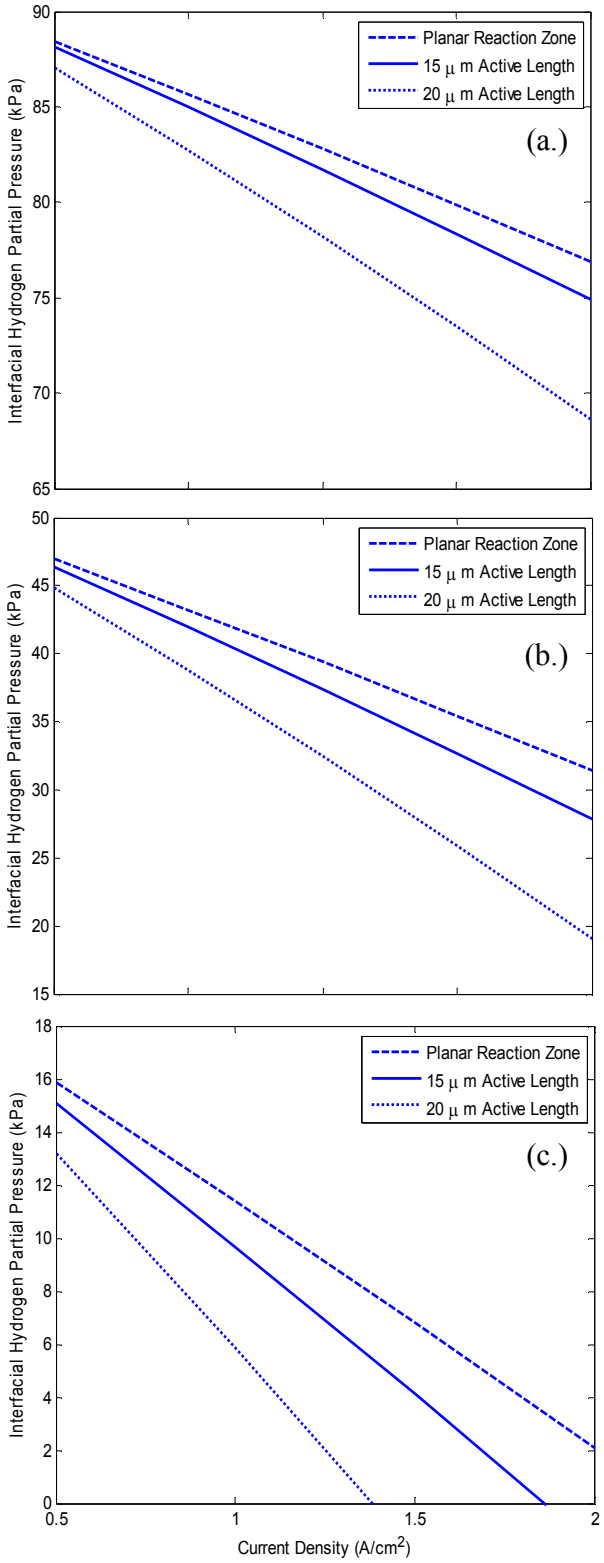

Figure 6.2 Comparison of minimum partial pressure predictions from fractal model with two different active length settings (15 and 20 μm) and a binary DGM with a planar reaction zone at (a.) 90% H2 (b.) 50% H2 and (c.) 20% H2 (anode thickness 750 μm, ε = 0.3, and τ = 5.0)

An expanded set of computational studies was run to further compare the scaling impact of the active length setting to the operational variables of current density and fuel stream hydrogen composition. The number of active length settings was increased to six with the addition of cases for 25 μm, 30 μm, 40 μm, and 50 μm. The fractal reaction zone template shown in Figure 6.1 was retained in these studies. A broader range of current densities was also examined, with eight settings employed covering the range of 0.5-4.0 A/cm^2 in increments of 0.5 A/cm^2. As in the initial studies, the Faradaic current boundary condition applied for the molar flux at the active sites was set randomly throughout the reaction zone geometries. Since this boundary condition was applied randomly three cases were run at each active length to allow for the comparison of replicate studies. The boundary conditions for each case were stored in separate data files to note which boundaries within the finite element model were activated. These data files allowed for loading specific boundary condition placements within the reaction zone model independent of the bulk electrode type and geometry.

The nature of the solution process outlined in Chapter 5 results in a basic scaling factor that is applied to the molar flux condition applied at the electrode-gas stream boundary in the one-dimensional bulk electrode portion of the model. The basic scaling factors seen for each active length setting are plotted in Figure 6.3. Over the range of active lengths studied it is apparent that this scaling factor largely follows a direct scaling behavior based on average length. However, the departure from direct scaling behavior increases marginally as the active length is increased. The modeling studies above follow a three-way layout experimental arrangement, so their results can be investigated using ANOVA to better determine the influence of each factor. A subsequent analysis of the

scaling behavior based on the three factors active length, current density, and hydrogen composition confirms the dominance of the active length setting, as outlined in Table 6.1. The current density and composition exhibit some significant influence on the behavior of the scaling factor, but this influence is much lower than that of active length setting.

A similar analysis of the minimum hydrogen composition behavior for the reaction zone demonstrates that each of these factors is of comparable significance, with no factor exerting an overwhelmingly dominant influence. This result is expected from the nature of the model. Since active length is established *a priori* in the present work, conservation of species would dictate that it is the dominant factor with respect to the scaling of molar flux between the active sites and the gas stream supplying the reactants. While basic, this insight demonstrates the importance of accounting for scaling between the apparent and real active lengths in performance predictions. Alternatively, composition within the reaction zone may vary and exhibits dependence on all three of the factors examined. Thus, the composition dependence on the reaction zone microstructure may be considered more susceptible to the influence of reaction zone microstructural details.

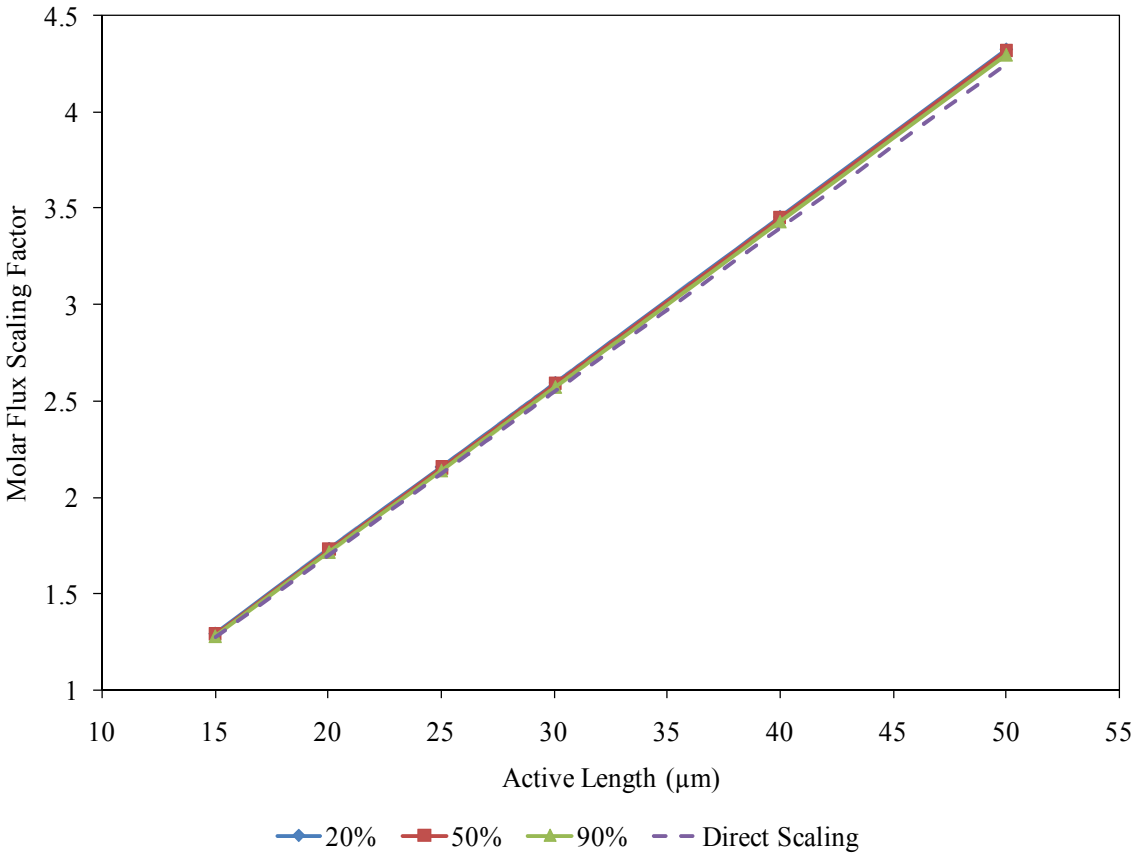

Figure 6.3 Molar flux scaling behavior observed over a range of active length settings for fractal reaction zone model with pore size of 2 µm; the results are compared to direct scaling behavior based on the ratio of apparent to actual active length

Table 6.1 ANOVA for current scaling in initial anode performance studies

Model Term	**DoF**	**Sum Sq**	**Mean Sq**	**F value**	**Pr(>F)**
Active Length (A)	5	455.93	91.186	1845002	<0.001
Current Density (B)	7	0.017	0.0025	50.46	<0.001
Composition (C)	2	0.029	0.0143	288.52	<0.001
factor(A):factor(B)	35	0.008	0.0002	4.35	<0.001
factor(A):factor(C)	10	0.002	0.0002	4.99	<0.001
factor(B):factor(C)	14	0.001	0.0001	1.02	0.4311
Residuals	358	0.018	$5x10^{-5}$		

6.1.1.2 Comparison of Microstructural Factors

In addition to the active length within a given reaction zone, electrode performance may be influenced by the pore size and the general accessibility of active sites. To further analyze the scaling and accessibility effects of the simulated fractal structure, as influenced by these microstructural factors, numerical studies were run with varying levels of these three parameters. Again, a standard anode thickness of 750 μm was modeled with reaction zones for each case having a size of ~10 μm. Pore sizes of 1 μm and 3 μm were modeled in addition to the 2 μm pore size examined above. The fractal templates applied for these two pore sizes are shown in Figure 6.4 and 6.5. For the 3 μm geometry the active lengths from the previous studies were applied (15-50 μm). However, for the 1 μm case both the width of the active region and the active lengths applied were reduced by a factor of two. This change allowed for a reduction in computational burden for the finite element model, due to a lowered number of elements required, while retaining the same concentration of active length per unit cross-sectional area. In the present work, the setting of active boundaries within a given branch of the reaction zone is considered as a descriptor of the active site accessibility. Two settings were applied for this factor. For a high level of accessibility, boundaries at all level within the fractal structure were allowed to be active, as in the active length and operational variable studies above. To simulate a low level accessibility activity was restricted to boundaries that lay within the third fractal generation of the porous structure. Multiple cases were applied for these boundary settings and stored for application in additional numerical studies. Finally, the fuel stream composition and current density were fixed at 90% hydrogen and 3.0 A/cm^2. This setting was chosen because in the

previous studies it was found to exhibit minimum hydrogen compositions that covered a range of possible polarization regimes, from ohmic loss dominance to concentration loss dominance.

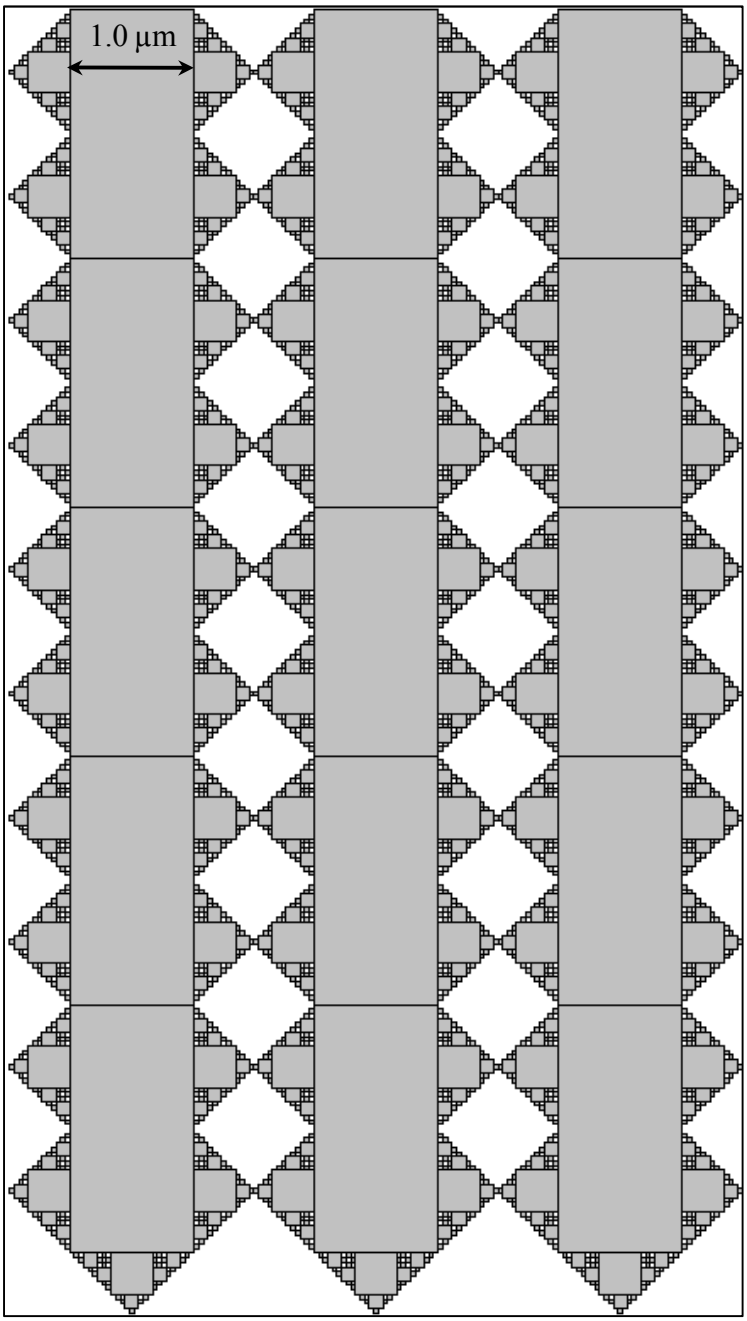

Figure 6.4 Simulated electrode reaction zone geometry for 1 µm pore size, approximate dimensions are 5.889 µm x 10.48 µm; a reduced reaction zone width was applied to maintain a lower number of elements in the finite element model

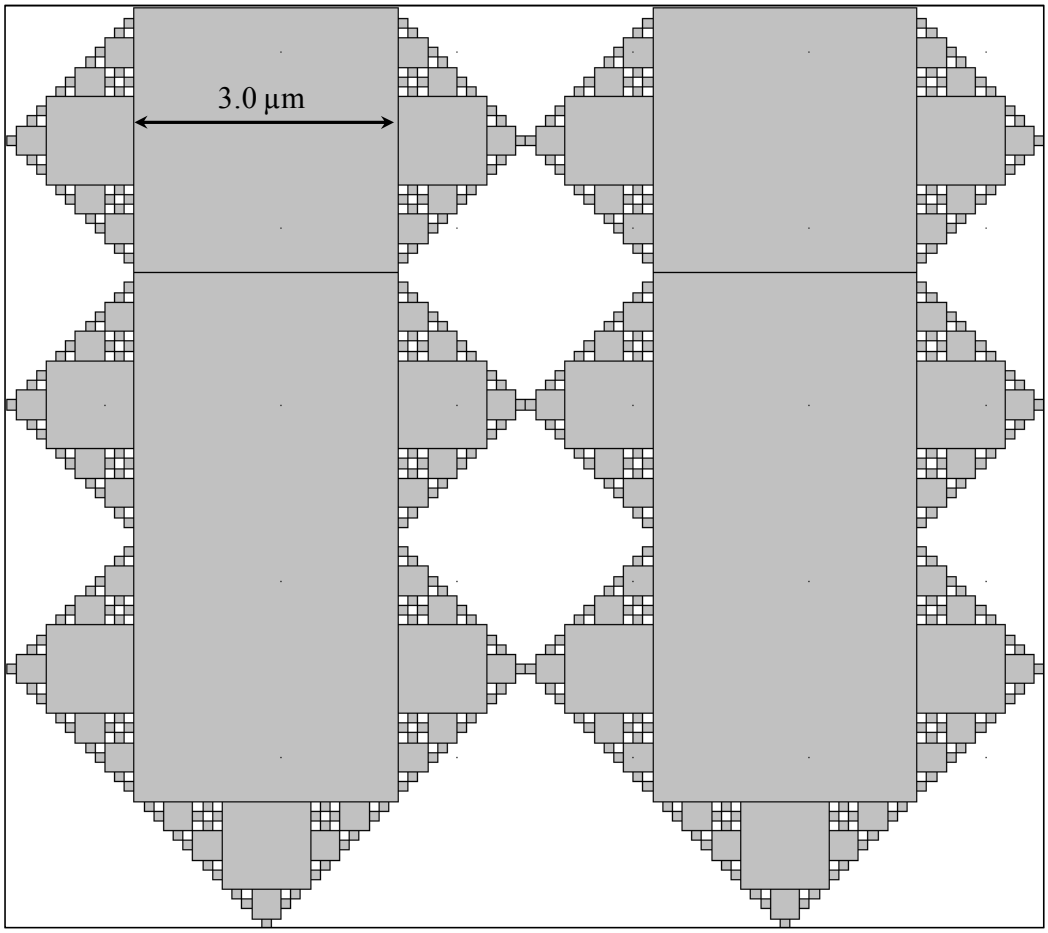

Figure 6.5 Simulated electrode reaction zone geometry for 3 μm pore size; approximate dimensions are 11.78 μm x 10.44 μm

The results of the modeling studies above can be investigated using ANOVA to better determine the influence of each microstructural factor. Analysis of the modeling results for all cases of the active length, pore size, and active level show that pore size and active length are the dominant factors with respect to current scaling, Table 6.2. On its own, the active level setting does not exhibit significant influence, but interaction effects including this setting appear significant, particularly with respect to the interaction between pore size and active level setting. Similar behavior is seen for the minimum partial pressure

dependence on the microstructural parameters, Table 6.3, with pore size and active length dominating the performance. While it is still not a significant factor, the active level (i.e. site accessibility) setting does show a slightly higher level of influence with respect to the minimum hydrogen partial pressure. As in the previous studies, the active length setting effectively controls the flow of reactants to the active zone and therefore shows the greatest influence over molar flux scaling and minimum hydrogen partial pressure within the reaction zone. The secondary pore size influence is the result of its presence in the calculation of the Knudsen diffusion coefficient for both the bulk electrode and the reaction zone.

Table 6.2 ANOVA for current scaling in anode microstructural studies

Model Term	**DoF**	**Sum Sq**	**Mean Sq**	**F value**	**Pr(>F)**
Active Length (A)	5	113.32	22.66	122287	<0.001
Active Level (B)	1	0	0	0.01	0.922
Pore Size (C)	2	0.058	0.029	156.32	<0.001
factor(A):factor(B)	5	0.002	0.0004	1.93	0.0976
factor(A):factor(C)	10	0.007	0.0007	4.03	0.0002
factor(B):factor(C)	2	0.002	0.0008	4.19	0.0185
Residuals	82	0.015	0.0002		

Table 6.3 ANOVA for minimum hydrogen partial pressure, anode microstructural studies

Model Term	**DoF**	**Sum Sq**	**Mean Sq**	**F value**	**Pr(>F)**
Active Length (A)	5	8.558	1.712	175506	<0.001
Active Level (B)	1	0	0	0.02	0.8796
Pore Size (C)	2	2.173	1.087	111421	<0.001
factor(A):factor(B)	5	0.0001	0.00002	1.93	0.0987
factor(A):factor(C)	10	0.508	0.0508	5205	<0.001
factor(B):factor(C)	2	0.0001	0.00005	5.29	0.0069
Residuals	82	0.0008	0.00001		

6.1.2 Investigations of Cathode Performance

6.1.2.1 Comparison of Microstructural Factors

To discern the influence of microstructural characteristics on cathode performance numerical studies similar to those for the anode microstructure were run for a cathode with a standard size of 50 μm, with ~10 μm of the electrode treated as the active region. The active length, pore size, and active boundary settings from the anode studies were used. The data files produced for the anode boundary conditions were used to designate the activate boundaries within the cathode. Here it should be noted that although the boundary locations were the same within the simulated fractal reaction zone, the Faradaic current was scaled to reflect the appropriate number of electrons exchanged in the oxygen reduction reaction. The composition and current density were fixed at 21% oxygen, assuming air as the oxidant, and 3.0 A/cm^2.

As with the studies of anode performance all cases show that pore size and active length are the dominant factors with respect to current scaling and minimum oxygen partial pressure. While not a significant factor, the active level setting does show a higher level of influence with respect to minimum oxygen partial pressure than it displays for the molar flux scaling effects. Additionally, this influence appears to be increased compared to the influence of the active level setting on the anode side. There are two possible causes for this increased influence. First, a reduced diffusion coefficient is seen for oxygen within the cathode, where D_{O2} is in the range of 1-1.5 cm^2/s compared to hydrogen diffusion coefficient of 4.5-6.5 cm^2/s within the anode. Additionally, for the thinner cathode the reaction zone geometry may exert greater influence over transport behavior, particularly with respect to active site accessibility, due to the reduced

influence of transport through the thinner bulk electrode. Taken with the insights from previous chapters regarding the performance challenges associated with thinner electrodes, the latter of these points underscores the general need for greater attention to be paid to transport within thinner SOFC electrodes that are typically considered non-limiting with respect to mass transport.

Table 6.4 ANOVA for current scaling in cathode microstructural studies

Model Term	**DoF**	**Sum Sq**	**Mean Sq**	**F value**	**Pr(>F)**
Active Length (A)	5	111.90	22.38	121999	<0.001
Active Level (B)	1	0	0	0.01	0.9221
Pore Size (C)	2	0.053	0.0263	143.6	<0.001
factor(A):factor(B)	5	0.002	0.0004	1.93	0.0986
factor(A):factor(C)	10	0.005	0.0005	2.93	0.0034
factor(B):factor(C)	2	0.002	0.0008	4.18	0.0187
Residuals	82	0.015	0.0002		

Table 6.5 ANOVA for minimum oxygen partial pressure, cathode microstructural studies

Model Term	**DoF**	**Sum Sq**	**Mean Sq**	**F value**	**Pr(>F)**
Active Length (A)	5	0.11487	0.02297	173321	<0.001
Active Level (B)	1	0	0	0.21	0.6504
Pore Size (C)	2	0.0168	0.0084	63362	<0.001
factor(A):factor(B)	5	0	0	2.11	0.0723
factor(A):factor(C)	10	0.00277	0.00028	2086	<0.001
factor(B):factor(C)	2	0	0	5.58	0.0042
Residuals	82	0.00001	1.2×10^{-7}		

6.2 Considerations for Reduced Order Approaches to SOFC Gas Diffusion

6.2.1 The Land Surveyor Approximation (LSA) in Catalysis

Sapoval initially proposed that the performance of irregular resistive interfaces subject to Laplacian transport phenomena can be described effectively based on the geometry of the interface alone [79]. Santra and Sapoval later demonstrated the effects

of pore surface irregularity on catalytic efficiency using simulations of ballistic transport in prefractal structures [70]. These surface irregularity effects were linked to two causes: direct scaling effects that arise from the increased length (or area) of the rough surface and accessibility effects influenced by more detailed microstructural characteristics of the surface. Through consideration of the Laplacian problem within a porous catalyst Sapoval and colleagues introduced the Land Surveyor Approximation (LSA) as a means of describing the influence of scaling and accessibility effects on catalyst performance with respect to transport near the active surface and within larger pore geometries [76, 78, 79, 82]. The LSA approach provides a useful means of analyzing the impacts of active length, pore size, and active site accessibility seen in the studies above. Furthermore, this approach allows for insight into reduced order approximations for the impacts of reaction zone microstructure on SOFC electrode performance.

The Land Surveyor Approximation allows for the description of surface roughness effects based on the relation between diffusive transport and surface reaction rates. As noted above, this approach was developed from exploration of Laplacian transport near a rough interface, such as the pore wall of a catalyst. An overview of this problem, as presented by Sapoval et al. [78], is shown in Figure 6.6. For the domain shown, the distribution of the reactant that is consumed at the interface is described by the Laplace equation. At the active interface the flux of the reactant is dependent on the concentration and a surface reaction rate coefficient, K_s. A fixed concentration, herein labeled C_0, is set as the boundary condition at a source line near the rough interface.

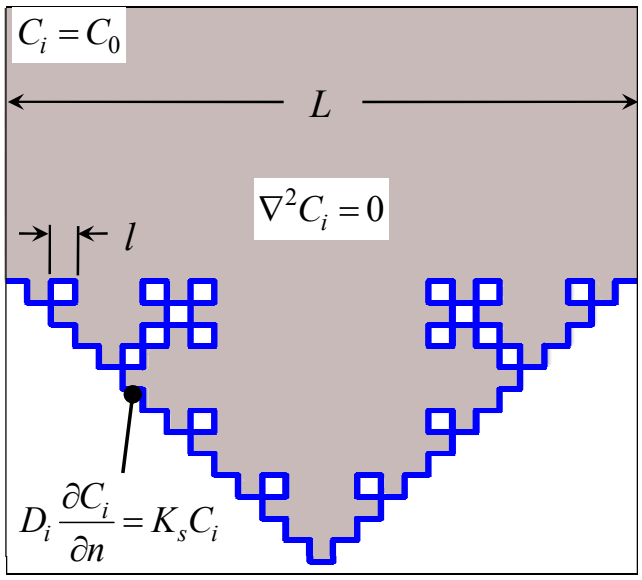

Figure 6.6 Laplacian transport problem near a rough catalyst interface of length L_p (indicated by the bold blue line) as examined by Sapoval et al. [78]

In their analysis, Sapoval et al. define a characteristic length scale for describing the effects of the rough catalytic interface by taking the ratio of the diffusion coefficient and surface reaction rate coefficient, Equation 6-1, which is referred to as the diffusion-reaction length scale. The magnitude of this length scale determines the expected performance of the catalytic surface. When the rate of reactant consumption at the surface is sufficiently lower than the rate of diffusion in the catalyst the diffusion-reaction length scale is significantly greater than the length of the active surface ($\Lambda >> L_p$). In this case, the reaction rates near the catalyst surface, and the corresponding catalytic efficiency, scale based on the ratio of the actual surface length (or area) and the apparent surface length (or area). In diffusion limited scenarios the diffusion-reaction length scale lies between the total surface length and the length of smallest branch in the fractal structure ($l \leq \Lambda \leq L_p$). In this regime, microstructural features give rise to a screening

effect, impeding transport to active sites, and the scaling relation becomes dependent on the microstructural characteristics of the rough surface [78, 79].

$$\Lambda = D_i / K_s \tag{6-1}$$

6.2.2 Application of the LSA in SOFC Modeling

The LSA approach presented by Sapoval and colleagues can be applied to further analyze the results of the fractal models presented above. However, two key distinctions must be made between the problem as it is presented in the literature and as it applies in the case of an SOFC electrode. For the SOFC electrode, the field examined is described using the dusty-gas formalism, and is therefore not strictly Laplacian. Additionally, in the present work the flux at the active interface is set using Faraday's law. An overview of the modified problem is shown in Figure 6.7.

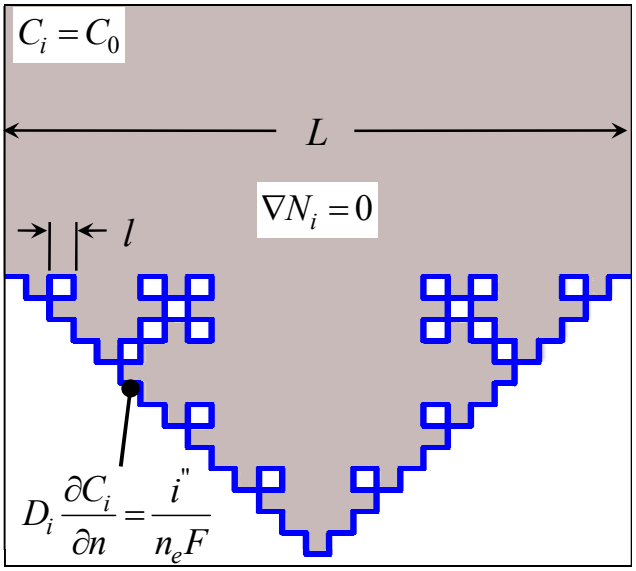

Figure 6.7 Transport problem near a rough interface as applicable to an SOFC electrode, subject to a Faradaic current boundary condition along the active surface; the molar flux, N_i, is defined using the dusty-gas formalism applied in the fractal reaction zone models

For the problem outlined in Figure 6.7, the diffusion-reaction length scale can be established based on Faraday's law. In determining the Thiele modulus for an SOFC electrode Costamagna et al. apply a coarse kinetic rate expression based on the current density and fuel stream composition [45]. This kinetic rate expression, Equation 6-2, can be cast in the form of a surface reaction rate coefficient based on the application of the Faradaic current boundary condition, as shown in Equation 6-3. Here, the electrode thickness is removed from the expression, since it not necessarily the length scale of interest. Instead this length scale is established through the parameter Λ. While not a rigorous definition, this coarse kinetic rate expression provides a means of calculating the diffusion-reaction length scale for the modified SOFC transport problem. The diffusion-reaction length scale for the transport problem with the Faradaic current boundary condition is expressed in Equation 6-4. Using this parameter a physical explanation of the active length scaling dominance can be inferred.

$$k = \frac{i''}{zFC_i^{ref} t_{elec}} \tag{6-2}$$

$$K_s = \frac{i''}{zFC_i^{ref}} \tag{6-3}$$

$$\Lambda = \frac{D_i zFC_i^{ref}}{i''} \tag{6-4}$$

For an initial exploration of the LSA concept as applied to SOFC mass transport a basic interfacial geometry similar to that in Figure 6.7 is examined. The apparent width of the interface is set to 2 μm, indicative of a dominant pore size for an SOFC electrode.

The distance from the source line ($C_i = C_0$) to the opening of the rough interface was set at 1 μm. The concentration was fixed at the source line, and the current density in the Neumann boundary condition at the rough interface was modified until the onset of depletion was observed. A sample reactant distribution is shown in Figure 6.8 for this surface geometry. The current density listed is the value applied along the reactive interface. To account for variation in the Knudsen diffusion coefficient the diffusion reaction length scale is calculated based on the average diffusion coefficient over the range of branch sizes. For the local current density shown there is minimal variation in reactant composition near the interface. This behavior is expected based on the diffusion-reaction length scale, which is significantly greater than the length of the active interface. In Figure 6.8, these lengths are both listed in relation to the minimum branch size following the convention of Sapoval et al. [78].

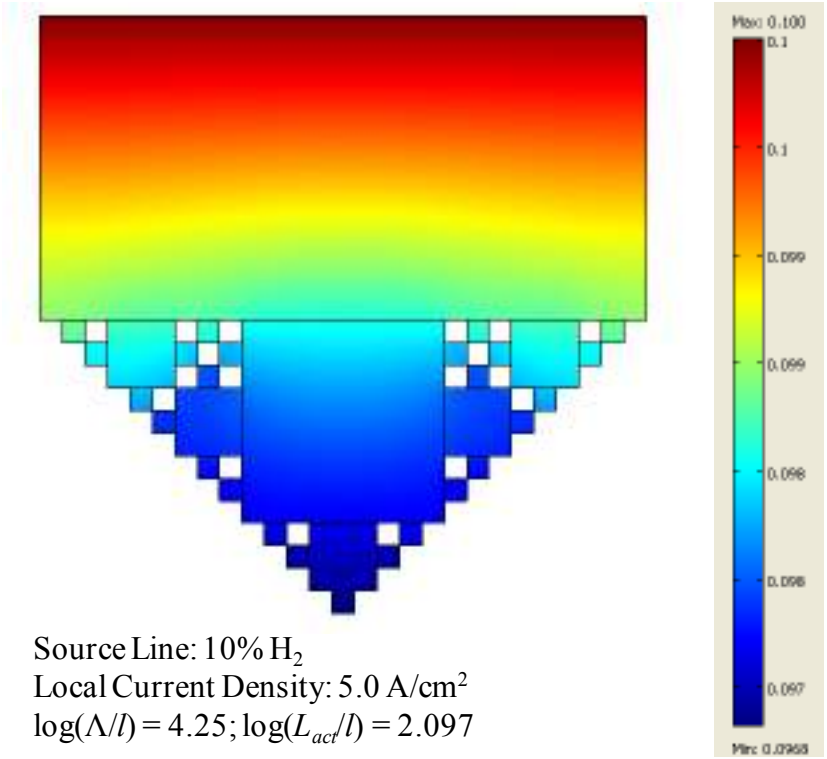

Source Line: 10% H_2
Local Current Density: 5.0 A/cm^2
$\log(\Lambda/l) = 4.25; \log(L_{act}/l) = 2.097$

Figure 6.8 Sample reactant (H_2) distribution for a basic fractal interface

Although the variation seen in the reactant distribution above is minimal, the potentially uneven nature of interfacial depletion phenomena at the active site level can be seen. The point at which such variations may require accounting for the microstructural detail of the rough interface can be determined from the basic finite element model. To do so, two reaction rate coefficients were calculated using Equation 6-3: one based on the source line concentration and one based on the average concentration along the entire rough interface. Comparing these two rate coefficients over the range on the diffusion-reaction length scales examined allows for observation of the onset microstructural screening effects on the reactant distribution that are caused by the rough interface, as shown in Figure 6.9. This onset is indicated by the departure of the interface average reaction rate coefficient from that of the source line, which occurs as the diffusion-reaction length scale begins to approach the magnitude of the active interface length. Values of Λ closer to the actual active length were not obtained because the onset of reactant depletion occurred while the diffusion-reaction length scale was still greater than the active length ($\Lambda \sim 2.75L_{act}$). The onset of microstructural screening effects at values of Λ greater that those suggested by Sapoval et al may be due to the differing nature of the boundary condition applied or the fact that the field described using the DGM formalism is not strictly Laplacian. Using a nonequilibrium molecular dynamics model Andrade et al. observed similar departure from the standard Laplacian problem for transition diffusion [75]. Additionally, the regimes proposed by Sapoval et al. were based on the general catalyst effectiveness and not the explicit reactant concentrations [78].

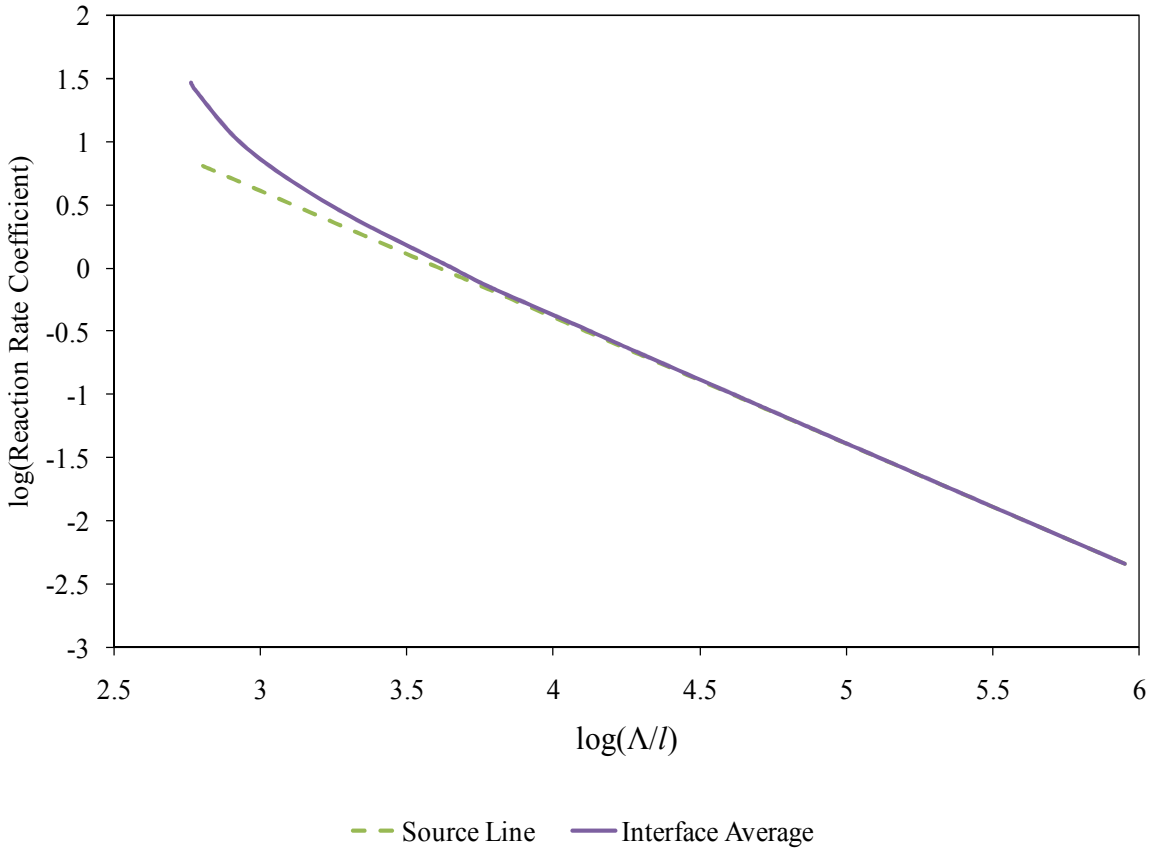

Figure 6.9 Approximate surface reaction rates as a function of diffusion-reaction length scale based on source line and interfacial average concentrations for a basic fractal interface geometry

It should be noted that achieving depleted scenarios in the exploration of the basic geometry above required either a high local current density or a very low source line concentration. Thus the onset of microstructural influences may be precluded in SOFC electrodes by influences of the bulk electrode geometry and the general pore geometry. Considering this point, extension of the LSA approach to the results from the fractal SOFC reaction zone studies elucidates the physical basis for the active length dominance and pore size significance that are observed. Here, the diffusion reaction length scale is calculated using the average reaction zone concentration as the reference. This value was

used because only a small disagreement was seen between the average and minimum concentrations for the reaction zone, so it is thought to be a sufficient approximation for the interfacial average. The minimum partial pressure for the consumed reactants in each electrode, as calculated in the fractal electrode models, are plotted in comparison to the diffusion-reaction length scale in Figure 6.10. Based on this length scale the cases examined fall well above the regime where microstructural screening effects would begin to influence performance. Thus, microstructural accessibility effects caused by surface irregularity are not seen as a significant factor in the studies presented above because diffusion restrictions within the porous structure are relatively weak. Instead, active length and pore size show the primary influence for transport phenomena assessed on larger length scales ranging from reaction zone size to bulk electrode dimensions. Compared to the active length settings examined and the total perimeters of the active regions, the characteristic length, Λ, defined by Sapoval et al. is significantly greater. As with the basic surface geometry above, in order to approach the microstructural screening regime reductions in the diffusion coefficient and average reaction zone composition of the consumed reactant, along with increases in the current density, would need to be large enough to achieve an appropriate reduction in the diffusion-reaction length scale. The majority of SOFC microstructural studies focus on impacts of pore size, particle size, porosity, and tortuosity, and often address variations in performance based on the average values of these properties [22, 44-46, 48, 50, 51, 53, 92, 93]. In some cases, anisotropy of characteristics such as pore tortuosity are addressed [51, 53], but such studies do not specifically address pore surface morphology, which may cause microstructural screening. Future SOFC microstructural characterization and design efforts would

benefit from further discerning the influence of these effects, particularly at length scales within the Knudsen diffusion regime.

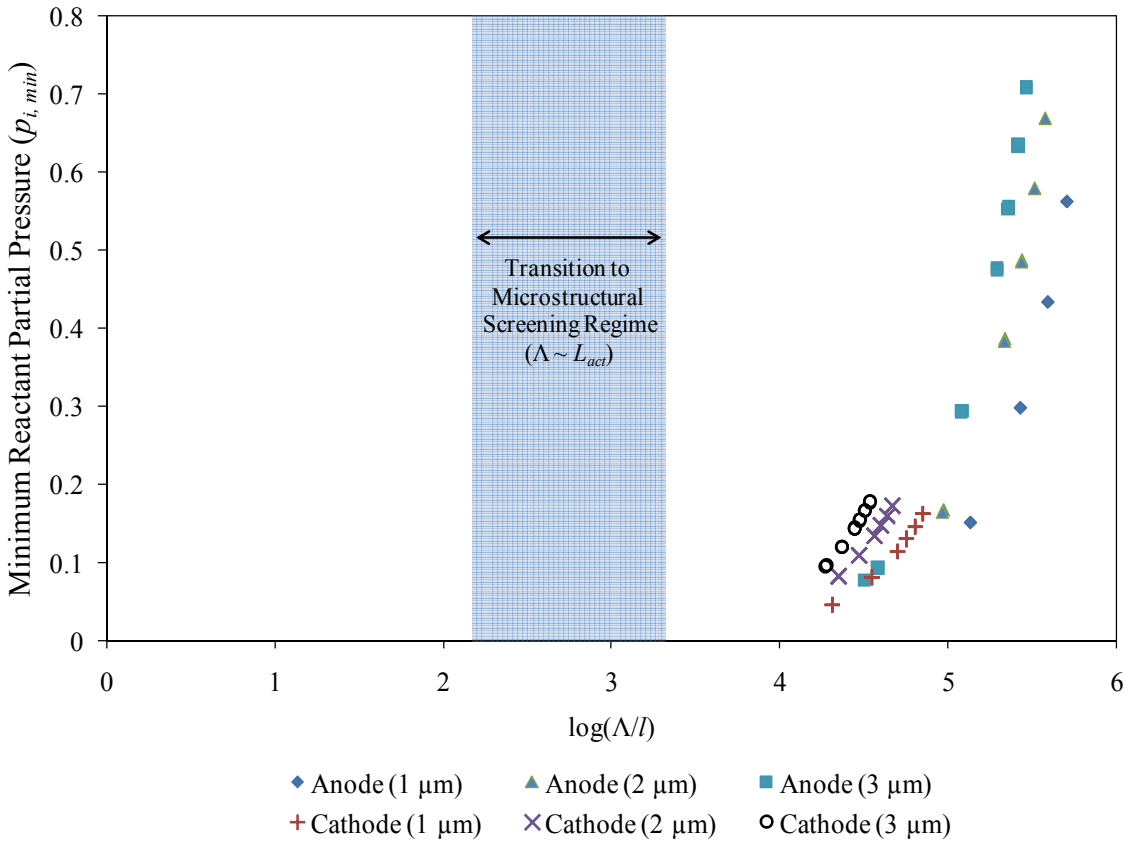

Figure 6.10 Minimum partial pressures (atm) observed in the numerical studies applying the SOFC electrode model with a fractal reaction zone compared to the diffusion-reaction length scale for reaction zone region

As an initial estimate the Faradaic diffusion-reaction length scale introduced above may allow for assessing the influence of microstructural details beyond average pore size and active length. Specifically, based on an active length and a minimum pore size (analogous to the smallest branch length *l*) one may determine if microstructural surface details exert a significant influence over electrode performance. The analyses above indicate that microstructural screening effects do not exert a significant influence at the

length scales explored. Thus a greater emphasis on describing the scaling relation between real and apparent active length (or area) for SOFC electrodes and accurately determining the pore size distribution may be warranted. Furthermore, there is a possibility that microstructural screening effects can have an impact on localized transport in the vicinity of active sites. While such effects can be initially investigated using finite element models and the approach outlined, the nature of pore sizes within the SOFC electrode and the length scales associated with triple phase boundaries may require more detailed numerical modeling approaches that are capable of handling diffusion within the transition and Knudsen regimes [46, 51, 53, 91]. Finally, lower diffusion-reaction length scales may result from specific surface reaction mechanisms, leading to increased microstructural influence. In such cases, the Land Surveyor Approximation would provide a readily accessible means of assessing this microstructural influence.

6.3 Connecting Continuum and Microstructural Component Models

A connection can be drawn between bulk electrode geometry effects on diffusive transport and the influence of microstructural features by examining the forms of limiting and depletion current densities previously addressed for SOFCs. Two forms of limiting current are defined in Equations 6-5 and 6-6. The first is the traditional definition of the limiting current density and the second is defined based on the unit cell half-width. The multi-dimensional depletion current density is restated in Equation 6-7.

$$i''_{\lim}\left(t_{elec}\right) = \frac{D_i^{eff} zFC_i^0}{t_{elec}} \tag{6-5}$$

$$i''_{\lim}(a) = \frac{D_i^{eff} zFC_i^0}{a} \tag{6-6}$$

$$i''_{dep} = \frac{D_i^{eff} zFC_i^0}{t_{elec} + \sum_{n=1}^{\infty} B_n \left[\cosh(\lambda_n t_{elec}) - \cos n\pi\right]} \tag{6-7}$$

These expressions bear the general form that is similar to that seen in the metric used to assess microstructural influence based on the Land Surveyor Approximation, as shown in Equation 6-8.

$$\frac{\Lambda}{l} = \frac{D_i zFC_i^{ref}}{l \cdot i''} \tag{6-8}$$

By comparing the limiting and depletion current densities in Equations 6-5 through 6-7 to the local current density, *i''*, the term Λ/l can be recast based on a general characteristic length, L_c, as shown in Equation 6-9.

$$\frac{\Lambda}{L_c} = \frac{D_i zFC_i^{ref}}{L_c i''} \tag{6-9}$$

As with the fractal geometries above, the general expression in Equation 5 provides a means of comparing the influence of diffusive mass transfer limitations to reaction limitations. However, using the more general form also allows for the comparison of geometric features across length scales. This comparison is made by drawing an analogy to the Thiele modulus, a common metric used for comparing reaction and diffusion rates

within porous catalysts. The parameter Λ/L_c can be related to the Thiele modulus, Φ, following Costamagna et al. [45], who defined the Thiele modulus based on the coarse kinetic rate expression described in Equation 6-2. Comparing Equations 6-9 and 6-10b reveals that the parameter Λ/L_c relates to the Thiele modulus according to Equation 6-11.

$$\Phi = L_c\sqrt{k/D_i} \tag{6-10a}$$

$$\Phi = L_c\sqrt{\frac{i''}{D_i z F C_i^{ref} L_c}} \tag{6-10b}$$

$$\frac{\Lambda}{L_c} = \frac{1}{\Phi^2} \tag{6-11}$$

Applying this common metric to the bulk electrode transport explored with the dimensionless performance metrics and the microstructural transport explored with the fractal model provides a means of assessing the diffusive mass transport influence of geometric features that exist across a broad range of length scales. An example of such an assessment is laid out in Figure 1. A log-log scale is applied to distinguish between electrode types at multiple scales. The characteristic lengths applied are representative of electrode thicknesses, unit cell widths, active lengths, and pore sizes that have been applied throughout the present work. Effective diffusion coefficients were used in calculations for the bulk electrode cases. For the active length and pore size cases, average Knudsen diffusion coefficients were calculated based on the branch sizes within the fractal structure. The diffusion coefficients in these latter cases were not modified.

The results shown in Figure 1 reflect some key insights discussed previously. For bulk electrodes the influence of anode thickness and unit cell width are comparable.

Therefore, such geometric designs can be considered well balanced in terms of the thickness-width mass transfer trade-off. However, for cathodes common unit cell widths tend to be greater than the commonly used electrode thicknesses. As a result, lateral effects are expected to exert a greater influence over mass transfer performance. These points were also demonstrated through the analysis of the dimensionless performance metrics in Chapter 4. In a similar fashion, the active lengths explored in the microstructural studies presented above can be seen as exerting a greater influence over diffusive transport than the microstructural features that may affect active site accessibility. Furthermore, there is smaller gap between the microstructural and bulk length scales for the cathode, suggesting the increased influence seen for microstructural effects in these thinner electrodes.

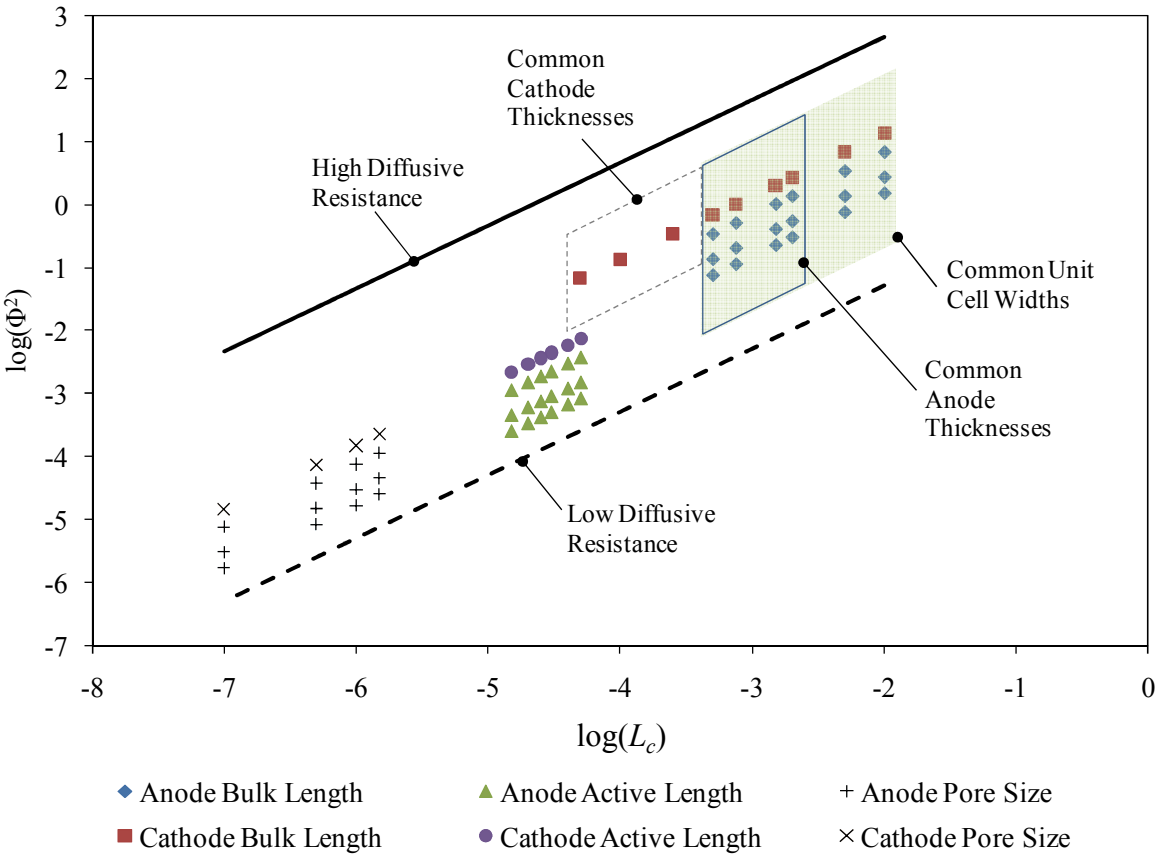

Figure 6.11 Assessment of diffusive mass transfer influence across length scales present in an SOFC electrode; reference lines for high and low diffusive resistance were calculated assuming diffusion coefficients of 0.01 cm^2/s and 10 cm^2/s, respectively.

6.4 Summary

The results of numerical studies presented above suggest that the active length and pore size within an SOFC reaction zone are the primary influences on mass transport performance. The former of these parameters can be accounted for in SOFC models by appropriate scaling of molar flux boundary conditions based on the ratio of real and apparent active length. Pore size effects are generally accounted for through the Knudsen diffusion coefficients, which are effectively averaged over the fractal reaction zone region in the fractal model. Additional active site accessibility, or microstructural

screening, effects were not found to exert a significant influence over electrode performance. This lack of influence can be explained using existing methods for assessing the effectiveness of porous catalysts, specifically the Land Surveyor Approximation developed by Sapoval et al. [78, 79]. This approach has been adapted for the case of transport in an SOFC electrode subject to a Faradaic molar flux boundary condition. When applied in the analysis of the modeling studies presented, the adapted approach reveals that limitations to reactant diffusion in SOFC electrodes may not be strong enough to result in microstructural screening at the length scales investigated. However, the influence of such effects may be increased for smaller pores or faster surface reaction kinetics. The fractal modeling approach outlined for SOFC electrodes provides a general framework for the further investigation of these more detailed cases. Additionally, this modeling approach enables development of a common metric for discerning between the influence of bulk electrode geometry effects on diffusive transport and the influence of more detailed microstructural features. This metric connects the comparison of the continuum and microstructural levels of transport within the SOFC electrode.

CHAPTER 7

CONCLUSIONS AND RECOMMENDATIONS

7.1 Conclusions

The diffusive mass transport mechanisms within porous SOFC components have been explored using two modeling approaches that can better inform the SOFC electrode design process. These approaches include the development of performance metrics for electrode cross-sectional design and a fractal approach for modeling mass transport within the electrode pore structure that focuses on microstructural details of the reaction zone within the electrodes. The first of these approaches describes the performance impacts of multi-dimensional mass transport and leads to the development of design maps that capture the inherent trade-offs in the design electrode cross-section geometry. The second approach provides an accessible numerical approach to modeling transport within the electrode reaction zone microstructure and, through the concept of the Land Surveyor Approximation, uncovers a straightforward approach for assessing the impact of specific microstructural details. These impacts include active length scaling effects and active surface accessibility effects associated with microstructural screening.

The dimensionless performance metrics presented for SOFC cross-sectional design applications were developed based on existing potential flow models. These metrics include a correction factor that can be applied to button-cell predictions of the reactant partial pressure distribution and two forms of dimensionless reactant depletion current density. The potential flow models that provide the basis for these performance metrics were compared to the more rigorous dusty-gas model to provide further understanding of

the limitations of the potential flow approach. As expected, it was found that the DGM produces more conservative predictions of interfacial partial pressures and depletion current density for dimensioned models. However, the dimensionless performance metrics developed may help close this gap in model performance. Furthermore, the analytical nature of these potential flow solutions and their associated performance metrics may enable the streamlined development of surrogate models for multi-dimensional effects on electrode performance.

The pressure correction factor developed shows sensitivity to the method used in calculating the effective diffusion coefficient within the SOFC electrode. However, when Knudsen diffusion is appropriately accounted for corrected one-dimensional dusty-gas model solutions can produce reactant partial pressure estimates that are comparable to estimates produced using two-dimensional finite element solutions. The analytical nature of this correction factor reduces computational time. Thus, it may serve as a modeling tool that can be applied to translate component level fidelity to cell and stack level models, particularly with respect to predicting the onset of reactant depletion phenomena.

The two depletion current density metrics presented allow for the development of electrode design maps based on dimensionless geometric parameters. A dimensionless depletion current density is developed to quantify the influence of sheet resistance effects on reactant depletion and demonstrate the mass transport trade-offs inherent in reducing electrode thickness for a fixed width unit cell geometry. Normalizing this current density metric by its one-dimensional form may allow for judgment of an electrode design's deviation from behavior predicted using button-cell tests and allows for review of existing electrode designs. This review demonstrates that proper electrode cross-

sectional design can result in electrodes that approach button-cell performance, and that excessively thin cathode designs may not be optimal from the standpoint of oxygen depletion. Furthermore, both of these depletion current density metrics are strictly functions of the bulk electrode geometry. Most notably, this dependence on geometry alone results in predictions of electrode reactant depletion performance that are in strong agreement with depletion behavior predicted using finite element models based on the dusty-gas model.

For common electrode geometries consideration of the trade-offs outlined for mass transport in SOFC electrode cross-sections also underscores the potential pitfalls of excessively thin electrodes. Thicker electrode geometries, commonly seen for SOFC anodes, are expected to be less susceptible to pronounced lateral reactant depletion. In contrast, the thinner electrode geometries, often used for the cathode, are expected to be prone to significant lateral depletion effects. These electrode geometries are also more likely to experience variation in molar flux along the electrode-electrolyte interface due to the influence of interconnect contact. Such variations require further consideration in future electrode modeling and design efforts for thinner electrodes. However, the results presented suggest that excessively thin electrodes may not be desirable when cross-sectional geometry effects are considered. Instead, cross-sectional designs that balance the key dimensions of electrode thickness, unit cell width, and interconnect and gas channel contact lengths may prove more desirable for mitigating losses associated with mass transport.

The potential flow and dusty-gas models applied in the exploration of SOFC cross-section design rely on average microstructural parameters and could be fortified by

greater consideration of the non-uniform nature of the porous electrode microstructure. To this end, a morphological fractal modeling approach common in the study of porous media was applied toward modeling diffusion within SOFC electrodes in an effort to capture the effects of microstructural variation on electrode performance. This model focused on applying a fractal geometry template to model the reaction zone while using a one-dimensional numerical solution to model the bulk electrode. The use of this fractal template allows for a focus on the effects of pore geometry on mass transfer while enabling implementation through accessible numerical tools, specifically Runge-Kutta and finite element methods. Additionally, using the combined bulk/reaction zone approach the boundary value problem describing mass transport within the electrode can be cast based on more detailed conditions within the reaction zone.

The electrode model incorporating a fractal reaction zone was compared to published experimental results as well as modeling results based on a one-dimensional dusty-gas approach assuming a planar reaction zone. Reasonable agreement between the fractal model and experimental results was demonstrated through direct comparison to concentration polarization measurements and voltage-current characteristics for several electrode geometries. Most notably, the model using the more detailed reaction zone description captures concentration polarization behavior missed when assuming planar reaction zones. However, in some cases this agreement is tempered by uncertainty in microstructural characteristics for the electrodes, specifically the active length within the reaction zone. In future work, coupling of the fractal template approach with percolation models within the solid matrix could mitigate this uncertainty.

Results of initial studies using the fractal SOFC electrode model suggest that more accurately accounting for active length within the reaction zone may impact performance predictions. As expected, increasing active length within the reaction zone resulted in reduced predictions of minimum hydrogen partial pressure as a function of current density, suggesting that scaling between the apparent and actual active areas may play a key role in mass transport performance of SOFC electrodes. The significance of active length scaling was confirmed by analyzing the results of an array of more detailed modeling studies using ANOVA. These studies included the variation of microstructural and operational variables for both the anode and the cathode. The analysis of the modeling results also demonstrated that within the operational regimes examined active site accessibility, represented by the activated levels of the fractal template structure, did not significantly influence modeling results.

For an SOFC the influence of geometric scaling effects and other microstructural factors, such as active site accessibility, can be estimated using methods developed in the study of catalysts. One such method is the Land Surveyor Approximation, which allows for the description of surface roughness effects based on the relation between diffusive transport and surface reaction rates [78]. In this approach a diffusion-reaction length scale is applied as a means of determining when surface reaction rates follow a simple scaling relation based on active length or if more complex microstructural screening effects influence transport. For a fractal template these regimes are established through comparison of the diffusion-reaction length scale to the total active length and the smallest branch size of the fractal structure. This approach could be extended to more complex structures using analogous measures of active length and minimum pore size.

In studies of catalyst performance, the LSA approach is based upon Laplacian transport near a surface subject to a flux boundary condition that is set based on a kinetic reaction rate. For SOFC diffusive mass transport this problem was modified by using the dusty-gas formalism for transport within the pore space and by applying a flux boundary condition that is established using Faraday's law. This latter modification allows for the definition of a Faradaic diffusion-reaction length scale that can be used to estimate the significance of microstructural screening effects within the reaction zone of an SOFC electrode.

For a simple rough interface subject to a Faradaic molar flux boundary condition microstructural screening effects were found to influence the reactant distribution as the diffusion-reaction length scale approached the magnitude of the active interface length. This earlier onset of microstructural screening effects occurred at length scales greater than those suggested in literature for a strictly Laplacian diffusion cell and is likely due to the application of the dusty-gas formalism, which accounts for both bulk and Knudsen diffusion effects within the transition regime. Discrepancies in the type of boundary condition applied may also influence this outcome. Values of the diffusion-reaction length scale closer to the actual active length were not obtained because the onset of reactant depletion occurred while the diffusion-reaction length scale was still greater than the active length. Furthermore, achieving depleted operation required either a high local current density or a very low source line concentration. While variation due to microstructural screening is minimal in the cases studied, at lower length scales (or for faster reaction kinetics) such effects may be more influential.

When applied to the results of the studies of the SOFC fractal electrode model the LSA approach enables a straightforward physical interpretation of the active length dominance and pore size significance that are observed in the numerical studies. Reaction zone geometry representative of common SOFC electrodes with respect to porosity and pore size characteristics was explored. For the cases examined the SOFC electrode were found to operate above the regime where microstructural screening effects begin to influence performance. In these cases, microstructural accessibility effects caused by surface irregularity were dominated by influence of active length and pore size. Thus, when assessed on length scales ranging from reaction zone size to bulk electrode dimensions the onset of microstructural influences may be precluded in SOFC electrodes by influences of the bulk electrode geometry and the general pore geometry. As with the basic geometry examined, the influence of microstructural screening effects may be increased for smaller pore sizes or for faster reaction kinetics.

Finally, comparing several forms of the depletion current density and the Faradaic diffusion-reaction length scale reveals a common metric that enables the assessment the influence of bulk electrode geometry effects on diffusive transport and the influence of more detailed microstructural features. Reviewing this metric over the range of characteristic lengths explored in the present work demonstrates similar insights seen using both the performance metrics for cross-sectional design and the Land Surveyor Approximation for SOFC electrodes. These insights include the dominance of unit cell width over thin electrode performance and the dominance of active length over reaction zone mass transport. This common metric provides a concise means of connecting and

comparing the continuum and microstructural levels of transport within the SOFC electrode.

7.2 Recommendations

The analytical models presented and the associated performance metrics that were developed capture the inherent trade-offs in the design of SOFC electrodes, particularly with respect to bulk mass transport. While these models offer key interconnect and bulk electrode design insights multi-dimensional transport phenomena they could be extended to other SOFC geometries and modes of transport. Similar analytical approaches could be applied to the cross-sectional design of tubular SOFCs to determine the impact of sheet resistance effects within the electrodes. Furthermore, drawing on analytical tools and numerical multiphysics approaches the impact of geometry effects on thermal transport could be explored, particularly with respect to the influence of cross-sectional temperature gradients on thermally induced stresses. Finally, while the analytical models presented can reduce computational burden, the associated series calculations may present a challenge with respect to model operation in real time simulation. While real time application may present a challenge, the reduced computational requirements offered by these analytical models could allow for the efficient development of surrogate models that are capable of accounting for such geometry effects in real time.

The fractal modeling approach presented provides an accessible framework for the exploration of SOFC microstructural influences in a controlled geometry. This approach allows for the consideration of microstructural details that are not captured by the analytical models of the bulk electrode and leads to a simplified means of assessing the

influence of electrode microstructural characteristics. However, the detailed and reduced order approaches could be expanded to incorporate specific surface reaction mechanisms and explore the interaction between these mechanisms and the pore surface microstructure. Application of similar fractal template approaches within numerical model that can extend to smaller length scales could also prove valuable for further discerning the influence of microscale and nanoscale features. Furthermore, the addition of solid phases into fractal template would allow for consideration of the impact of percolation phenomena on active length and active site dispersion. Finally, to complement these modeling studies microstructural characterization techniques could be applied to better determine the extent of self-similarity within SOFC electrode microstructure. Existing approaches for experimentally determining the fractal characteristics of physical systems, such as those discussed by Barnsley [67], could be readily applied in these characterization efforts.

The modeling approaches presented provide an accessible set of SOFC electrode design tools that allow for the consideration of interconnect geometry effects and the influence of key reaction zone microstructural characteristics. The performance metrics developed facilitate the design of SOFC cross-sectional geometry in a manner that can efficiently capture the trade-offs in reducing losses associated with mass transport. The analysis of these metrics introduces key caveats with respect to the design of thinner electrodes that do not provide cell mechanical support, typically the cathode. However, future electrode modeling and design efforts require more detailed treatment of the interaction between mass and electronic transport, particularly within thin electrodes. The reduced computational requirements of these models establish a clear path forward

for the incorporation of geometry effects into higher level models at the cell, system, and stack levels. However, these models rely on a simplified treatment of electrochemically active regions within SOFC electrodes. The fractal modeling approaches presented provide a means of addressing the microstructural details of these regions and provide insight into the influence of reaction zone characteristics on SOFC performance. The models developed suggest that active length and pore size exert a dominant influence over transport within the reaction zones. While the strength of this influence may be tempered at lower length scales or for specific surface reactions, the fractal modeling approaches can be modified to incorporate these more complex physical phenomena. Therefore, they provide a general means of expanding the exploration of interfacial phenomena within SOFC electrodes while controlling key microstructural characteristics. Together, these modeling approaches provide a key perspective on the impacts bulk and microstructural geometry in porous SOFC components.

APPENDIX A

DERIVATION OF POTENTIAL FLOW MODELS

The general form of the boundary value problem explored for the reactant distribution in an SOFC electrode is described in Equations A-1 through A-4. The associated domain for this problem is shown in Figure A.1.

$$\frac{\partial^2 p_i}{\partial x^2} + \frac{\partial^2 p_i}{\partial y^2} = 0 \tag{A-1}$$

$$\frac{\partial p_i}{\partial y}(x,0) = \frac{R_u T}{zFD_{ij}} \frac{\tau}{\varepsilon} i'' \tag{A-2}$$

$$\frac{\partial p_i}{\partial y}(x, t_{elec}) = \begin{cases} \dfrac{R_u T}{zFD_{ij}} \dfrac{a}{b} \dfrac{\tau}{\varepsilon} i''; & 0 < x < b \\ 0, & b < x < a \end{cases} \tag{A-3}$$

$$\frac{\partial p_i}{\partial x}(0, y) = 0\,, \; \frac{\partial p_i}{\partial x}(a, y) = 0 \tag{A-4}$$

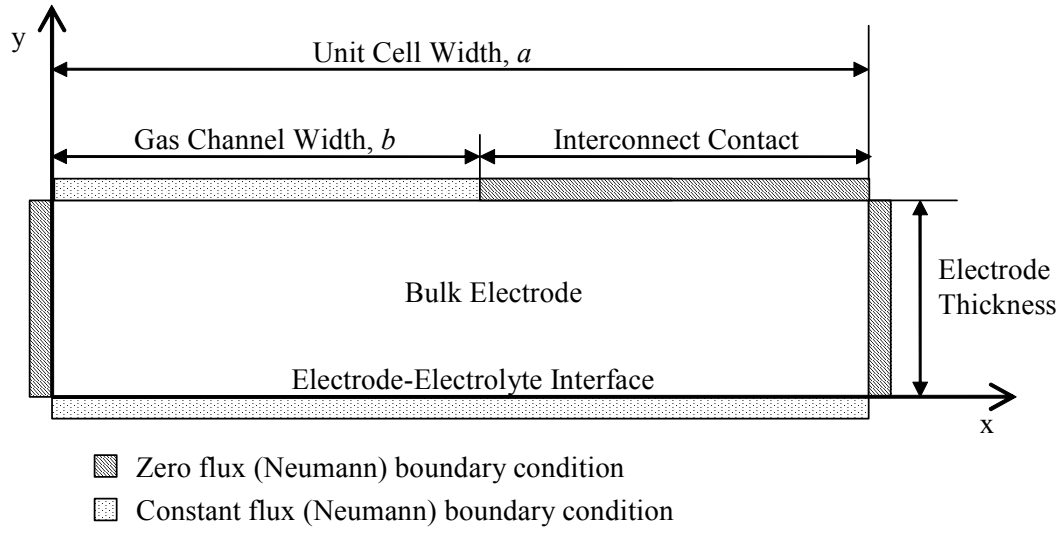

Figure A.1 General domain studied for neutral species mass transport model development

The scaling factor for the y-derivative boundary conditions, *a/b*, was found by equating the molar flow rates at each interface and solving for the anode-electrolyte molar flux. This method readily reveals the scaling relationship.

$$\dot{n}_{elec-GS} = \dot{n}_{elec-el}$$

$$J''_{elec-GS} \int dA_{elec-GS} = J''_{elec-el} \int dA_{elec-el}$$

$$J''_{elec-GS} = J''_{elec-el} \frac{a}{b}$$

Solution to the linear homogeneous problem above can be obtained using the standard technique of separation of variables [94]. The reactant partial pressure is expressed as the product of two functions $X(x)$ and $Y(y)$. This solution is then substituted into Equation A-1 and the boundary conditions are converted.

$$p_i(x,y) = \quad X(x)\cdot Y(y) \tag{A-5}$$

$$\frac{X''(x)}{X(x)} + \frac{Y''(y)}{Y(y)} = 0 \tag{A-6}$$

As functions of different independent variables X and Y must be to a constant α, such that:

$$\frac{X''}{X} = \alpha \tag{A-7}$$

$$\frac{Y''}{Y} = -\alpha \tag{A-8}$$

The following eigenvalue problem for $X(x)$ results

$$X''-\alpha X = 0 \tag{A-9}$$

$$X'(0) = 0\,,\ X'(a) = 0 \tag{A-10}$$

At this point the constant α can be either positive, negative, or zero. However, it can be shown that for the eigenvalue problem above $\alpha > 0$ results in a trivial solution. Therefore, only the cases for $\alpha \leq 0$ yield solutions. These solutions are:

$p = 0$
$X(x) = c_1 x + c_2 \Rightarrow c_1 = 0, \quad c_2 =$ Any constant

$$p < 0, \quad p = -\lambda^2$$
$$X(x) = c_1 \cos \lambda x + c_2 \sin \lambda x \Rightarrow c_2 = 0, \quad \lambda_n = \frac{n\pi}{a}$$

Applying these values of α to the problem for $Y(y)$ yields the solutions:

$$\alpha = 0$$
$$Y(y) = c_1 y + c_2$$

$$\alpha < 0, \quad \alpha = -\lambda^2$$
$$Y(y) = c_1 \cosh \lambda y + c_2 \sinh \lambda y$$

These solutions for $X(x)$ and $Y(y)$ can be combined to form a generic expression for the reactant partial pressure, Equation A-11. This form of the solution is comparable to that defined by Polyanin for the Laplace equation in a rectangular domain subject to flux boundary conditions [95]. However, the present problem is distinguished by the retention of the first two terms on the right-hand side of the equation and the application of the composite boundary condition along the boundary sharing contact with the gas channel and interconnects.

$$p_i(x,y) = A_0 + B_0 y + \sum_{n=1}^{\infty} \left[A_n \cosh(\lambda_n y) + B_n \sinh(\lambda_n y) \right] \cos(\lambda_n x) \qquad \text{(A-11)}$$

Determining the appropriate constants for the particular solution requires differentiation of Equation A- 11 with respect to y and application of the remaining boundary conditions, Equations A-2 and A-3.

$$\frac{\partial p_i}{\partial y} = B_0 + \sum_{n=1}^{\infty}\left[A_n\lambda_n \sinh(\lambda_n y) + B_n\lambda_n \cosh(\lambda_n y)\right]\cos(\lambda_n x) \tag{A-12}$$

$$\frac{\partial p_i}{\partial y}(x,0) = B_0 + \sum_{n=1}^{\infty} B_n\lambda_n \cos(\lambda_n x) \tag{A-13}$$

$$\frac{\partial p_i}{\partial y}(x,t_{elec}) = B_0 + \sum_{n=1}^{\infty}\left[A_n\lambda_n \sinh(\lambda_n t_{elec}) + B_n\lambda_n \cosh(\lambda_n t_{elec})\right]\cos(\lambda_n x) \tag{A-14}$$

Equations A-2 and A-13 can be applied to determine the constants B_0 and B_n using a Fourier series expansion.

$$B_0 = \frac{1}{a}\int_0^a \left(\frac{R_u T}{zFD_{ij}}\frac{\tau}{\varepsilon} i''\right)dx = \frac{R_u T}{zFD_{ij}}\frac{\tau}{\varepsilon} i'' \tag{A-15}$$

$$B_n = \frac{2}{a}\int_0^a \frac{1}{\lambda_n}\frac{R_u T}{zFD_{ij}}\frac{\tau}{\varepsilon} i''\cos(\lambda_n x)dx = 0 \tag{A-16}$$

Similarly, Equations A-3 and A-14 can be applied to determine the constant A_n. A Fourier series expansion for B_0 using these equations confirms the value shown in Equation A-15.

$$\begin{aligned} A_n &= \frac{2}{a}\int_0^a \frac{1}{\lambda_n \sinh(\lambda_n t_{elec})}\frac{\partial p_i}{\partial y}(x,t_{elec})\cos(\lambda_n x)dx \\ &= \frac{2}{a\lambda_n \sinh(\lambda_n t_{elec})}\left[\int_0^b \left(\frac{R_u T}{zFD_{ij}}\frac{a}{b}\frac{\tau}{\varepsilon} i''\right)\cos(\lambda_n x)dx + \int_b^a 0\,dx\right] \end{aligned} \tag{A-17a}$$

$$A_n = \frac{2B_0 \sin(\lambda_n b)}{n\pi\lambda_n \sinh(\lambda_n t_{elec})}\left(\frac{a}{b}\right) \tag{A-17b}$$

This yields a form of the reactant partial pressure distribution with one remaining constant, A_0.

$$p_i(x,y) = A_0 + B_0 y + \sum_{n=1}^{\infty} A_n \cosh(\lambda_n y)\cos(\lambda_n x) \tag{A-18}$$

To set this constant it is assumed that the reactant partial pressure at the gas channel centerline ($x = 0$, $y = t_{elec}$) is equal to the gas composition within the bulk gas channel. This constraint results in the solution for the electrode reactant partial pressure shown in Equation A-20.

$$p_i(0,t_{elec}) = p_i^0 = A_0 + B_0 t_{elec} + \sum_{n=1}^{\infty} A_n \cosh(\lambda_n t_{elec}) \tag{A-19}$$

$$\begin{aligned} p_i(x,y) = {} & p_i^0 - B_0(t_{elec} - y) \\ & - \sum_{n=1}^{\infty} A_n \left[\cosh(\lambda_n t_{elec}) - \cosh(\lambda_n y)\cos(\lambda_n x)\right] \end{aligned} \tag{A-20}$$

APPENDIX B

DERIVATION OF DIMENSIONLESS DEPLETION CURRENT DENSITY

Defined in terms of the unit cell half-width, the limiting current density is:

$$i''_{\lim}(a) = \frac{zFD_{ij}p_i^0}{R_uTa}\frac{\varepsilon}{\tau} \tag{B-1}$$

As noted in Equation 3-25, the depletion current density is:

$$i''_{dep} = \frac{zFD_{ij}}{R_uT}\frac{\varepsilon}{\tau}\frac{p_i^0}{t_{elec} + \sum_{n=1}^{\infty} B_n\left[\cosh(\lambda_n t_{elec}) - \cos n\pi\right]} \tag{B-2}$$

$$B_n = \frac{A_{n,elec}}{A_{0,elec}} = \frac{2\sin(\lambda_n b)}{n\pi\lambda_n \sinh(\lambda_n t_{elec})}\left(\frac{a}{b}\right) \tag{B-3}$$

Taking the ratio of these two expressions yields the dimensionless depletion current density.

$$\begin{aligned} i^*_{dep} &= \frac{i''_{dep}}{i''_{\lim}(a)} \\ &= \frac{\dfrac{zFD_{ij}}{R_uT}\dfrac{\varepsilon}{\tau}\dfrac{p_i^0}{t_{elec} + \sum_{n=1}^{\infty} B_n\left[\cosh(\lambda_n t_{elec}) - \cos n\pi\right]}}{\dfrac{zFD_{ij}p_i^0}{R_uTa}\dfrac{\varepsilon}{\tau}} \end{aligned} \tag{B-4}$$

$$i_{dep}^{*} = \frac{1}{\frac{1}{a}\left\{ t_{elec} + \sum_{n=1}^{\infty} B_n \left[\cosh\left(\lambda_n t_{elec}\right) - \cos n\pi \right] \right\}} \tag{B-5}$$

Recall that the eigenvalues, λ_n, for the potential flow solutions are functions of the unit cell half-width ($\lambda_n = n\pi/a$). With appropriate substitutions, this expression can be cast in terms of the length fraction ($LF = b/a$) and dimensionless thickness ($t^* = t_{elec}/a$).

$$i_{dep}^{*} = \frac{1}{\frac{1}{a}\left\{ t_{elec} + \sum_{n=1}^{\infty} \frac{2\sin\left(\frac{n\pi}{a} b\right)}{n\pi \frac{n\pi}{a} \sinh\left(\frac{n\pi}{a} t_{elec}\right)} \left(\frac{a}{b}\right) \left[\cosh\left(\frac{n\pi}{a} t_{elec}\right) - \cos n\pi \right] \right\}} \tag{B-6}$$

Proper simplification yields the expression for the dimensionless depletion current density shown in Equation 3-33b.

$$i_{dep}^{*} = \frac{1}{t^* + \sum_{n=1}^{\infty} \frac{2\sin\left(n\pi LF\right)}{n^2\pi^2 \sinh\left(n\pi t^*\right)} \left(\frac{1}{LF}\right) \left[\cosh\left(n\pi t^*\right) - \cos n\pi \right]} \tag{B-7}$$

REFERENCES

[1] Minh, N.Q., J. Am. Ceram. Soc., 1993. **76**(3): p. 563-588.

[2] Hawkes, G.L., et al., *CFD Model of a Planar Solid Oxide Electrolysis Cell for Hydrogen Production from Nuclear Energy*, in *The 11th International Topical Meeting on Nuclear Reactor Thermal-Hydraulics (NURETH-11)*. 2005: Popes' Palace Conference Center, Avignon, France.

[3] O'Brien, J.E., et al., J. Fuel Cell Sci. Tech., 2005. **2**(3): p. 156-63.

[4] Hickey, D., et al. *Optimization and demonstration of a solid oxide regenerative fuel cell system*. 2005. Quebec, Canada: Electrochemical Society Inc., Pennington, NJ 08534-2896, United States.

[5] Sridhar, K.R., et al. *Applications and markets for solid oxide regenerative fuel cells*. 2005. Quebec, Canada: Electrochemical Society Inc., Pennington, NJ 08534-2896, United States.

[6] Nelson, G.J. and C.L. Haynes, J. Power Sources, 2008. **185**(2): p. 1168-1178.

[7] Kakaç, S., A. Pramuanjaroenkij, and X.Y. Zhou, International Journal of Hydrogen Energy, 2007. **32**(7): p. 761-786.

[8] Campanari, S. and P. Iora, Fuel Cells, 2005. **5**(1): p. 34-51.

[9] Ferguson, J.R., J.M. Fiard, and R. Herbin, J. Power Sources, 1996. **58**(2): p. 109-22.

[10] Gemmen, R.S. and C.D. Johnson, J. Power Sources, 2005. **144**(1): p. 152-64.

[11] Khaleel, M.A., et al., J. Power Sources, 2004. **130**(1-2): p. 136-48.

[12] Selimovic, A., et al., J. Power Sources, 2005. **145**(2): p. 463-469.

[13] Yakabe, H., et al., J. Power Sources, 2001. **102**(1-2): p. 144-154.

[14] Smirnov, A., A. Burt, and I. Celik, J. Power Sources, 2006. **158**(1): p. 295-302.

[15] *Fuel Cell Handbook*. 6th ed. 2002, U.S. Dept. of Energy, National Energy Technology Laboratory: Morgantown, West Virginia.

[16] Nelson, G.J. and C.L. Haynes. *Localized constriction resistance effects upon SOFC transport phenomena*. in *2005 ASME International Mechanical Engineering Congress and Exposition*. 2005. Orlando, FL.

[17] Larminie, J. and A. Dicks, *Fuel Cell Systems Explained*. 2nd ed. 2003, Chichester, West Sussex: J. Wiley.

[18] Kendall, K., International Materials Reviews, 2005. **50**(5): p. 257-64.

[19] Haile, S.M., Acta Materialia, 2003. **51**(19): p. 5981-6000.

[20] Jiang, Y. and A.V. Virkar, J. Electrochem. Soc., 2003. **150**(7): p. 942-951.

[21] Kim, J.-W., et al., J. Electrochem. Soc., 1999. **146**(1): p. 69-78.

[22] Zhao, F. and A.V. Virkar, J. Power Sources, 2005. **141**(1): p. 79-95.

[23] Henne, R., Journal of Thermal Spray Technology, 2007. **16**(3): p. 381-403.

[24] Hui, R., et al., J. Power Sources, 2007. **170**(2): p. 308-323.

[25] Liu, Y., C. Compson, and M. Liu, J. Power Sources, 2004. **138**(1-2): p. 194-198.

[26] Sofie, S.W., J. Am. Ceram. Soc., 2007. **90**(7): p. 2024-2031.

[27] Tanner, C.W. and A.V. Virkar, J. Power Sources, 2003. **113**(1): p. 44-56.

[28] Chan, S.H. and Z.T. Xia, J. Appl. Electrochem., 2002. **32**(3): p. 339-47.

[29] Lin, Z., J.W. Stevenson, and M.A. Khaleel, J. Power Sources, 2003. **117**(1-2): p. 92-97.

[30] Fleig, J. and J. Maier, *The influence of inhomogeneous potential distributions on the electrolyte resistance in solid oxide fuel cells*, in *Fifth International Symposium on Solid Oxide Fuel Cells (SOFC-V)*. 1997: Aachen, Germany.

[31] Fleig, J., et al., Solid State Ionics, 1998. **113-115**: p. 739-747.

[32] Lin, Y. and S.B. Beale, Appl. Math. Model., 2006. **30**(11): p. 1485-1496.

[33] Ji, Y., et al., J. Power Sources, 2006. **161**(1): p. 380-391.

[34] Sudaprasert, K., R.P. Travis, and R.F. Martinez-Botas, P. I. Mech. Eng. A-J. Pow., 2005. **219**(3): p. 159-167.

[35] Hussain, M.M., X. Li, and I. Dincer, Int. J. Energ. Res., 2005. **29**(12): p. 1083-1101.

[36] Suwanwarangkul, R., et al., J. Power Sources, 2003. **122**(1): p. 9-18.

[37] Washak, H., S.M. Guo, and A. Turan. *Gas transport in porous electrodes of solid oxide fuel cells*. 2005. Quebec, Canada: Electrochemical Society Inc., Pennington, NJ 08534-2896, United States.

[38] Tseronis, K., I.K. Kookos, and C. Theodoropoulos, Chem. Eng. Sci., 2008. **63**(23): p. 5626-5638.

[39] Nelson, G. and C. Haynes, *Localized constriction resistance effects upon SOFC transport phenomena*, in *2005 ASME International Mechanical Engineering Congress and Exposition (IMECE2005)*. 2005: Orlando, FL, United States.

[40] Krishna, R. and J.A. Wesselingh, Chem. Eng. Sci., 1997. **52**(6): p. 861-911.

[41] Mason, E.A. and A.P. Malinauskas, *Gas transport in porous media: the dusty-gas model* Chemical engineering monographs. Vol. 17. 1983, Amsterdam: Elsevier.

[42] Liu, M., J. Electrochem. Soc., 1998. **145**(1): p. 142-154.

[43] Tanner, C.W., K.-Z. Fung, and A.V. Virkar, J. Electrochem. Soc., 1997. **144**(1): p. 21-30.

[44] Cannarozzo, M., et al., J. Fuel Cell Sci. Tech., 2007. **4**(1): p. 99-106.

[45] Costamagna, P., P. Costa, and V. Antonucci, Electrochim. Acta, 1998. **43**(3-4): p. 375-394.

[46] Schneider, L.C.R., et al., Electrochim. Acta, 2006. **52**(1): p. 314-324.

[47] Costamagna, P., P. Costa, and E. Arato, Electrochim. Acta, 1998. **43**(8): p. 967-972.

[48] Schneider, L.C.R., et al., Electrochim. Acta, 2007. **52**(9): p. 3190-3198.

[49] Zhu, H. and R.J. Kee, J. Electrochem. Soc., 2008. **155**(7): p. B715-B729.

[50] Nam, J.H. and D.H. Jeon, Electrochim. Acta, 2006. **51**(17): p. 3446-3460.

[51] Izzo Jr, J.R., et al., J. Electrochem. Soc., 2008. **155**(5): p. B504-B508.

[52] Izzo Jr, J.R., A.A. Peracchio, and W.K.S. Chiu, J. Power Sources, 2008. **176**(1): p. 200-206.

[53] Wilson, J.R., et al., Nature Materials, 2006. **5**(7): p. 541-544.

[54] Joshi, A.S., et al., J. Power Sources, 2007. **164**(2): p. 631-638.

[55] Joshi, A.S., et al., J. Phys. D: Appl. Phys., 2007. **40**(23): p. 7593-7600.

[56] Nelson, G. and C. Haynes, *Parametric studies of constriction resistance effects upon solid oxide cell transport*, in *2006 ASME International Mechanical Engineering Congress and Exposition (IMECE2006)*. 2006: Chicago, IL, United States.

[57] Ni, M., D.Y.C. Leung, and M.K.H. Leung, J. Power Sources, 2008. **183**(2): p. 668-673.

[58] Williford, R.E., et al., J. Electrochem. Soc., 2003. **150**(8): p. 1067-1072.

[59] Williford, R.E. and L.A. Chick, Surf. Sci., 2003. **547**(3): p. 421-437.

[60] Shi, Y., N. Cai, and C. Li, J. Power Sources, 2007. **164**(2): p. 639-648.

[61] Lee, W.Y., D. Wee, and A.F. Ghoniem, J. Power Sources, 2009. **186**(2): p. 417-427.

[62] Kerkhof, P.J.A.M., Chemical Engineering Journal, 1996. **64**(3): p. 319-342.

[63] Young, J.B., Annual Review of Fluid Mechanics, 2007. **39**: p. 193-215.

[64] Young, J.B. and B. Todd, International Journal of Heat and Mass Transfer, 2005. **48**(25-26): p. 5338-5353.

[65] Keil, F.J., Chem. Eng. Sci., 1996. **51**(10 pt A): p. 1543-1567.

[66] Haugaard, J. and H. Livbjerg, Chem. Eng. Sci., 1998. **53**(16): p. 2941-2948.

[67] Barnsley, M.F., *Fractals everywhere*. 2nd ed. / ed, ed. H. Rising. 1993, Boston :: Academic Press Professional.

[68] Mandelbrot, B.B., *The fractal geometry of nature*. Updated and augmented. ed. 1983, New York :: W.H. Freeman.

[69] Yu, B. and W. Liu, AIChE Journal, 2004. **50**(1): p. 46-57.

[70] Santra, S.B. and B. Sapoval, Physical Review E. Statistical Physics, Plasmas, Fluids, and Related Interdisciplinary Topics, 1998. **57**(6): p. 6888-6888.

[71] Coppens, M.O., *Accessibility of a Catalyst's Fractal Surface to Diffusing and Reacting Molecules*, in *Fractals in engineering : from theory to industrial applications*, J.L. Vehel, E. Lutton, and C. Tricot, Editors. 1997, Springer: London.

[72] Coppens, M.O. and G.F. Froment, Fractals, 1995. **3**(4).

[73] Malek, K. and M.-O. Coppens, Physical Review Letters, 2001. **87**(12): p. 125505-4.

[74] Malek, K. and M.-O. Coppens, Journal of Chemical Physics, 2003. **119**(5): p. 2801-2811.

[75] Andrade Jr, J.S., et al., Physical Review E - Statistical, Nonlinear, and Soft Matter Physics, 2003. **68**(4 1): p. 416081-416084.

[76] Costa, M.H.A.S., et al., Physical Review E - Statistical, Nonlinear, and Soft Matter Physics, 2003. **67**(6 1): p. 061406/1-061406/5.

[77] Grebenkov, D.S., Physical Review Letters, 2005. **95**(20): p. 1-4.

[78] Sapoval, B., J.S. Andrade Jr, and M. Filoche, Chem. Eng. Sci., 2001. **56**(17): p. 5011-5023.

[79] Sapoval, B., Physical Review Letters, 1994. **73**(24): p. 3314-3314.

[80] Liu, J.G. and Y.F. Nie, Journal of Environmental Sciences, 2001. **13**(2): p. 170-172.

[81] Zhang, B. and X. Liu, AIChE Journal, 2003. **49**(12): p. 3037-3047.

[82] Sapoval, B., et al., Fractals, 2004. **12**(4): p. 381-387.

[83] Shi, Y., et al., J. Power Sources, 2006. **160**(1): p. 277-283.

[84] Shi, Y., et al., J. Power Sources, 2008. **185**(1): p. 241-247.

[85] Watt-Smith, M.J., et al., J. Power Sources, 2008. **184**(1): p. 29-37.

[86] Park, B.Y., et al., J. Electrochem. Soc., 2007. **154**(2): p. P1-P5.

[87] Reid, R.C., J.M. Prausnitz, and T.K. Sherwood, *The Properties of Gases and Liquids*. 3rd ed. 1977, New York: McGraw-Hill.

[88] Incropera, F.P. and D.P. DeWitt, *Fundamentals of Heat and Mass Transfer*. 5th ed. 2002, New York: John Wiley and Sons.

[89] Waldbillig, D., A. Wood, and D.G. Ivey, J. Power Sources, 2005. **145**: p. 206-215.

[90] Yakabe, H., et al., J. Power Sources, 2000. **86**(1-2): p. 423-431.

[91] Jena, A. and K. Gupta. *Characterization of pore structure of electrodes of solid oxide fuel cells*. 2005. Cocoa Beach, FL, United states: American Ceramic Society.

[92] Suzuki, T., et al., Science, 2009. **325**(5942): p. 852-855.

[93] Zhu, B., et al., Int. J. Energ. Res., 2002. **26**(1): p. 57-66.

[94] Powers, D.L., *Boundary value problems*. 4th ed. ed. 1999, San Diego, CA :: Academic Press.

[95] Polyanin, A.D., *Handbook of linear partial differential equations for engineers and scientists*. 2002, Boca Raton, Fla. :: Chapman & Hall/CRC.